

UC Berkeley

UC Berkeley Electronic Theses and Dissertations

Title

Optimal Control of Commercial Office Battery Systems, and Grid Integrated Energy Resources on Distribution Networks

Permalink

<https://escholarship.org/uc/item/5mb285r6>

Author

Sankur, Michael

Publication Date

2017

Peer reviewed|Thesis/dissertation

**Optimal Control of Commercial Office Battery Systems, and Grid Integrated
Energy Resources on Distribution Networks**

by

Michael Derin Sankur

A dissertation submitted in partial satisfaction of the

requirements for the degree of

Doctor of Philosophy

in

Engineering - Mechanical Engineering

in the

Graduate Division

of the

University of California, Berkeley

Committee in charge:

Professor Dave Auslander, Chair
Professor Kameshwar Poolla
Assistant Professor Scott Moura
Adjunct Professor Alexandra Von Meier

Fall 2017

**Optimal Control of Commercial Office Battery Systems, and Grid Integrated
Energy Resources on Distribution Networks**

Copyright 2017
by
Michael Derin Sankur

Abstract

Optimal Control of Commercial Office Battery Systems, and Grid Integrated Energy Resources on Distribution Networks

by

Michael Derin Sankur

Doctor of Philosophy in Engineering - Mechanical Engineering

University of California, Berkeley

Professor Dave Auslander, Chair

The proliferation of new sensing and actuation technologies presents new opportunities for enhanced supervision, optimization, and control of energy systems. In the commercial office environment, the use of smart power strips, uninterruptible power supplies, and advanced building energy management systems is growing as a means to implement control of energy efficiency measures and demand response. In electricity distribution networks, phasor measurement units and inverters are enabling utility operators to monitor and manage distribution systems more effectively. The physics or operational constraints of systems within the commercial office environment or distribution networks are often nonlinear or nonconvex, and thus difficult to incorporate into optimization programs. This dissertation presents research into modeling and optimal control of two nonlinear energy systems.

At the commercial office scale, we discuss the development and implementation of optimal control of plug loads and office scale battery storage. Building upon successes in optimal control of plug loads, we propose a model predictive controller (MPC) for the incorporation of battery storage. We derive a model of an off the shelf battery storage system through experimental data, and discuss extensions to allow controllable charging. We investigate two methods to solve the nonlinear and binary MPC, and simulations show the promise dynamic programming method.

At the distribution network scale, we discuss power flow models for optimization of grid distributed energy resources (DER), and techniques for solving nonlinear optimal power flow (OPF) problems. First, we study semidefinite programming as a method for solving nonlinear OPFs for control of voltage phasors. Simulation results motivate the development of novel models. We then derive a linearized unbalanced power flow model (LUPFM) for use in convex optimal power flow (OPF) formulations. The LUPFM builds upon previous work by adding a relationship between voltage phasor and complex power flow. A study into the LUPFM accuracy shows its fidelity for benchmark networks. We discuss two applications of the LUPFM. The first is balancing of voltage magnitude on a distribution network, and simulations are successful for both radial and mesh networks. The second application is

minimization of voltage magnitude and angle difference for switching operations. Simulations show the success and potential of the LUPFM for OPF control of voltage phasors.

To Nellie the Elephant
See you on the road to Mandalay

Contents

Contents	ii
List of Figures	v
List of Tables	vii
1 Introduction	1
1.1 Modeling and Optimal Control of Commercial Office Plug Loads and Battery Storage Systems	1
1.2 Optimization and Control of Distribution Network Scale Energy Systems . .	2
1.3 Research Contributions	3
1.4 Organization of this Dissertation	4
I Modeling and Optimal Control of Commercial Office Plug Loads and Battery Storage Systems	5
2 Introduction	6
3 Model Predictive Control of Plug Loads and an Office Scale Battery Storage System	8
4 Experimentally Derived OSBS Battery Model	14
5 An Exhaustive Search Numerical Method and Simulation Results	19
5.1 Exhaustive Search Numerical Method	19
5.2 Simulation Results using Exhaustive Search Method	21
6 A Dynamic Programming Algorithm for the MPC Optimization Program and Simulation Results	30
6.1 Dynamic Programming Algorithm	30
6.2 Simulation Results using Dynamic Programming Algorithm	32

7	Concluding Remarks and Future Work	39
II	Modeling of Unbalanced Power Flow and Optimal Control of Distributed Energy Resources for Grid Reconfiguration	41
8	Introduction	42
8.1	Nomenclature, Definitions, and Preliminaries	44
9	A Discussion of Semidefinite Programming for Optimal Power Flow Problems	49
9.1	Introduction	49
9.2	Previous Research in SDP for OPFs	50
9.3	Extensions of the SDP OPF for Control of Voltage Phasors	52
9.4	Conclusions	62
10	Derivation of a Linearized Unbalanced Power Flow Model	64
10.1	Introduction	64
10.2	Derivation of Power and Losses for Unbalanced Approximate Power Flow . .	65
10.3	Derivation of Voltage Magnitude Relations for Unbalanced Approximate Power Flow	67
10.4	Derivation of Voltage Angle Relations for Unbalanced Approximate Power Flow	71
10.5	Linearized Unbalanced Power Flow Model	75
11	Accuracy Analysis of Linearized Unbalanced Power Flow Approximation	77
12	Applications of the Linearized Unbalanced Power Flow Model	83
12.1	Voltage Magnitude Balancing	83
12.2	Phasor Difference Minimization for Switching Operations	90
13	Concluding Remarks and Future Work	99
14	Conclusion	101
14.1	Modeling and Optimal Control of Commercial Office Plug Loads and Battery Storage Systems	101
14.2	Modeling of Unbalanced Power Flow and Optimal Control of Distributed Energy Resources for Grid Reconfiguration	102
	Bibliography	103
A	Distribution Network Parameters	108
A.1	Parameters of the Five Node Network	108
A.2	Parameters of the IEEE 13 Node Test Feeder	109

A.3 Parameters of the Nine Node Meshed Network	112
B Newton-Raphson Algorithm for Solving Approximate Unbalanced Power Flow	117
C Derivation of a Half-space Approximations for L2 Norm Constraints	121

List of Figures

3.1	Office plug loads and OSBS presided over by an EIG	10
3.2	Plot of inconvenience function $r(Q_t)$ where $Q_r = 40$ and $r_r = 0.1$	13
4.1	APC UPS charging cycle SOC and net power.	15
4.2	APC UPS computed charging power and piecewise linear charging power model.	17
5.1	Demand response (DR) and load-following (LF) scenario load-shed targets.	22
5.2	Total and component load-shed of plug loads and an OSBS for static target scenario.	23
5.3	Demand response scenario simulation results for UPS and CBS.	28
5.4	Load-following scenario simulation results for UPS and CBS.	29
6.1	OSBS operation states for DR scenario.	35
6.2	Performance comparison between UPS and CBS for DR scenario.	36
6.3	OSBS operation states for LF scenario.	37
6.4	Performance comparison between UPS and CBS for LF scenario.	38
8.1	Simple network showing node voltages, line currents, and line impedances	46
8.2	Diagram of simple network showing node voltage, node load, line impedance, and line complex power.	46
9.1	Diagram of simple network used in SDP OPF Simulations.	54
9.2	Results of OPF (9.16) simulations with varying voltage magnitude reference and reactive power dispatch penalty. Blue dots represent cases with rank-one solutions. Red dots represent cases where a rank-one solution was not obtained.	57
9.3	Results of OPF (9.16) simulations with varying voltage magnitude reference and reactive power dispatch penalty. Blue dots represent cases with rank-one solutions. Red dots represent cases where a rank-one solution was not obtained.	57
11.1	IEEE 13 node feeder topology modified for accuracy analysis of unbalanced approximate power flow model.	79
11.2	Maximum voltage magnitude error across all phases and nodes from Monte Carlo simulation.	80
11.3	Apparent power error from Monte Carlo simulation.	80

11.4	Monte Carlo simulation results for voltage angle error and total vector error for case where all voltage magnitudes are assumed to be 1 in (10.44).	81
11.5	Monte Carlo simulation results for voltage angle error and total vector error for case where voltage magnitudes in (10.44) are assigned to the values from solving power flow.	82
12.1	Modified IEEE 13 node feeder topology for voltage magnitude balancing simulation.	85
12.2	Plot of voltage magnitudes for base case of voltage magnitude balancing scenario	86
12.3	Plot of voltage magnitudes for control case of voltage magnitude balancing scenario	86
12.4	Comparison of voltage magnitude imbalance for voltage balancing scenario. . . .	87
12.5	Nine node mesh network topology.	88
12.6	Plot of voltage magnitudes for base case of voltage magnitude balancing scenario for nine node mesh network	88
12.7	Plot of voltage magnitudes for control case of voltage magnitude balancing scenario for nine node mesh network	89
12.8	Comparison of voltage magnitude imbalance for voltage balancing scenario for nine node mesh network.	89
12.9	Distribution network composed of two IEEE 13 node feeder models connected to same transmission line.	92
C.1	Tangential half-space approximation of circle.	123
C.2	Error of half-space approximation of apparent power constraint.	123

List of Tables

3.1	Nomenclature for Part I.	9
3.2	OSBS decision variables and operation states.	11
5.1	Plug loads used in simulations.	22
5.2	Comparison of UPS and CBS performance for DR scenario.	25
5.3	Comparison of UPS and CBS performance for LF scenario.	27
6.1	OSBS control states in Figure 6.1 and Figure 6.3.	33
8.1	Nomenclature for Part II.	45
9.1	Voltage from solving power flow [48] with zero DER dispatch.	55
12.1	Optimal DER dispatch for voltage balancing on IEEE 13 node feeder	87
12.2	Optimal DER dispatch for voltage balancing on nine node mesh network	90
12.3	Results of phasor matching for switching action simulation.	95
12.4	Optimal DER dispatch for phasor matching and switching action	96
12.5	Results of phasor matching for switching action simulation.	97
12.6	Optimal DER dispatch for phasor matching and switching action	98
A.1	Five node network node parameters	108
A.2	Five node network line parameters.	108
A.3	Five node network complex demands	109
A.4	Five node network capacitors	109
A.5	Five node network DER apparent power capacity.	109
A.6	IEEE 13 node test network node phases	109
A.7	IEEE 13 node test network line parameters.	111
A.8	IEEE 13 node test feeder complex demands	112
A.9	IEEE 13 node test feeder capacitors	112
A.10	IEEE 13 node feeder DER apparent power capacity	112
A.11	Nine node mesh network node parameters	113
A.12	Nine node mesh network line parameters.	115
A.13	Nine node mesh network complex demands	116

A.14 Nine node mesh network capacitors 116
A.15 Nine node mesh network DER apparent power capacity. 116

Acknowledgments

First and foremost, I would like to thank my advisor Professor Dave Auslander for all the help, advice, insight, and support that he has given me during my time as Ph.D. student. I am grateful for the opportunity to work with him, and all of the knowledge and experience that I have gained from being his student.

I owe a large debt of gratitude to my friend, colleague, and mentor Dr. Dan Arnold. His continued friendship, support, and guidance has helped me immensely throughout this process. I am very grateful to have worked alongside Dan, and without him this dissertation would not be possible.

I want to express my deep gratitude to Professor Alexandra Von Meier for her support and mentorship. Her research insight and feedback have been invaluable. I also want to thank her for the opportunity to be a graduate student instructor.

I would like to thank Professor Kameshwar Poolla for serving on my dissertation committee. I also want to thank Professor Scott Moura for serving on my dissertation committee, for his dissertation feedback and advice, and for the opportunity to be a graduate student instructor.

I am grateful to Professors Karl Hedrick, Dennis Lieu, Shmuel Oren, and Kameshwar Poolla for serving on my qualification exam committee.

I would like to thank the Department of Defense and the National Defense Science and Engineering Graduate Fellowship program, for the award in 2009.

I want to express my gratitude to my colleagues from the DIADR (A Distributed Intelligent Automated Demand Response Building Management System, # DE-EE0003847) project: Tyler Jones, Andrew Krioukov, Nate Murthy, Jorge Ortiz, Therese Peffer, Jay Taneja, Jason Trager, Rongxin Yin, Siyuan Zhou, and the research staff at Siemens.

I want to thank my colleagues from the OpenBAS (Open Building Automation System, #DE-EE0006351) project: Therese Peffer, Marco Pritoni and Jacob Cabrera.

I want to thank my colleagues from the ARPA-E (#DE-AR0000340) project: Kyle Brady and Roel Dobbe.

I am grateful to Emma Stewart for providing employment and research opportunities at Lawrence Berkeley National Laboratory.

I want to thank my family. My mother Vega and father Haluk have provided tremendous support and inspiration with unlimited patience throughout this process. I am grateful to my sister Ailene as she was my childhood role model and she inspired me to seek an education. I am also grateful she did not earn a PhD, as I have now won this round of sibling rivalry.

I am very grateful for my family friend Marla Petal for her invaluable help in motivation and organization.

Chapter 1

Introduction

With the advent of new technologies ranging from smart power strips, uninterruptible power supplies, the internet of things, advanced metering infrastructure for electric grid, micro synchophasor measurement units, to inverters there are new and exciting areas in which to apply optimization and control theory to energy systems. However, many of these systems have nonlinear physics or nonlinear operational characteristics and thus require suitable mathematical models or optimization techniques. The focus of this work is to apply modeling, optimization and control techniques to two nonlinear energy systems. The first system is a commercial office with plug loads and battery storage. The second is an unbalanced distribution network with integrated distributed energy resources (DER).

1.1 Modeling and Optimal Control of Commercial Office Plug Loads and Battery Storage Systems

Commercial buildings are becoming increasingly metered and controllable with the adoption of technologies such as smart meters, smart power strips, and advanced building energy management systems [19, 49]. Economic incentives such as time-of-use electricity pricing has led to many research efforts in and the advancement of technologies for commercial building efficiency and demand response.

An area often overlooked until recently in commercial buildings for load-shedding are plug loads [3, 19, 40]. Systems such as office scale battery storage (OSBS) are enabling peak load reduction and load shifting actions to be complemented by plug loads [41]. In this work, we study the modeling optimal control of plug loads and an OSBS in a commercial office setting. The effort is detailed in Part I of this dissertation.

This work builds upon previous effort of plug load control [2, 4, 3, 40], we focus mainly on the integration of an off the shelf OSBS system. Firstly, a model predictive controller (MPC) is formulated that encapsulates the behavior of plug loads. A battery charging and discharging model is derived from experimental data. The battery model is nonlinear and nonconvex, with two modes of operation. Next, techniques for obtaining the optimal control

state of plug loads and the OSBS are discussed. The first technique is an exhaustive search algorithm, and simulations highlight its shortcomings. The second technique studied is dynamic programming. Simulations show its strength in optimizing over long time horizons with good time granularity.

1.2 Optimization and Control of Distribution Network Scale Energy Systems

Modeling, formulation, and solving of optimal power flow (OPF) problems is an area of research that is increasingly important with the advent of renewable and distributed energy resources, and the increasing ubiquity of grid sensors and data [43]. An important area for the application of OPF is grid reconfiguration for grid stability, reliability and integration of micro-gridding. In this work, we study OPFs that seek to manage DER for grid reconfiguration actions on an unbalanced network.

The physics of power flow are nonlinear and nonconvex, making it difficult to directly incorporate the physics into an reliably and easily solvable OPF problem. To address this, research has focused on semidefinite programming (SDP) and approximate power flow models [7], however literature has highlighted some drawbacks that may preclude its widespread applicability [24, 27]. Novel linearized models for unbalanced power flow are used for their linear properties, however their approximate nature may not capture important nonlinear physics [14, 39].

Our first effort in this area is to develop SDP OPFs for control of voltage magnitude and angle, and to explore convergence to a physically meaningful solution through simulation. We propose and derive several OPFs for control of voltage phasors. Simulations motivate further study in the control of voltage magnitude, and show the viability of placing bounds on voltage angle.

Our second effort is to develop a model that can be incorporated into a convex program, and thus we derive a linearized unbalanced power flow model (LUPFM). This model augments previous literature [14, 39] by adding a relationship for voltage angle and complex power flow. We investigate the accuracy of the LUPFM, and find it acceptable for benchmark networks.

Two OPF applications of the LUPFM are discussed. The first OPF seeks to balance voltage magnitude across different phases at nodes on a network. Simulation results show the ability of the OPF to reduce voltage imbalance for both radial and mesh networks. The second OPF seeks to minimize the voltage phasor difference between two points on a network for switching actions. Simulation results show the ability of the OPF to regulate voltage magnitude and angles at different points on a network.

1.3 Research Contributions

The contributions of Part I, titled Modeling and Optimal Control of Commercial Office Plug Loads and Battery Storage Systems, of this work are as follows:

- Chapter 3: A model predictive control formulation is developed that expands on previous work in optimal control of plug loads [3, 40]. This MPC incorporates devices commonly found in commercial offices and an abstract energy storage model.
- Chapter 4: A battery model of an off the shelf uninterruptible power supply (UPS) is derived through experimentation. To incorporate a real UPS into the MPC from Chapter 3, its battery discharging and charging and charge controller characteristics are investigated and modeled.
- Chapter 5: An exhaustive search method for solving the MPC is investigated. Simulation results show the limited viability of this method.
- Chapter 6: A dynamic programming method for solving the MPC is investigated. Simulation results show its promise as a viable method for optimizing over extended periods.

The contributions of Part II, titled Modeling of Unbalanced Power Flow and Optimal Control of Distributed Energy Resources for Grid Reconfiguration, of this work are as follows:

- Chapter 9: The derivation and investigation of SDP OPFs for control of voltage phasors. Simulation results further motivate efforts in this area, and the exploration of other power flow models.
- Chapter 10: The derivation of a linearized unbalanced power flow model (LUPFM). This model augments that of [14, 39] by incorporating a relationship between voltage angle and complex power flow.
- Chapter 11: The accuracy of the LUPFM is investigated, with simulation results demonstrating model accuracy for benchmark networks.
- Chapter 12: Two OPFs that incorporate the LUPFM are designed and experiments are performed demonstrating the its effectiveness in OPFs for voltage control.
 - Section 12.1: OPF1 seeks to minimize voltage magnitude imbalance across a distribution network. Simulation results show significant reduction in voltage imbalance.
 - Section 12.2: OPF2 seeks to minimize voltage phasor difference (both voltage magnitude difference and angle difference) between two points in a network for switching actions. Simulations show OPF2 controlling both voltage magnitude and angle, thus reducing potential power flow across an open switch scheduled to be closed.

1.4 Organization of this Dissertation

Part I of this dissertation is concerned with modeling and optimal control of office scale battery storage systems.

- Chapter 2 gives overview of existing technologies and summarizes the effort undertaken in Part I.
- Chapter 3 discusses the derivation of an MPC for optimal load-shedding through control of plug loads and battery storage.
- Chapter 4 discusses the derivation of a battery system operation model through experimental data.
- Chapter 5 presents an exhaustive search control algorithm and simulation results are discussed.
- Chapter 6 derives and discusses a dynamic programming algorithm for optimizing OSBS control state, and simulation results for two scenarios are discussed.
- Chapter 7 provides concluding remarks and a discussion of future work.

Part II of this dissertation is concerned with power flow models and optimization of distribution networks.

- Chapter 8 summarizes the current state of research into linear and nonlinear OPFs and outlines the research effort of Part II.
- Chapter 9 discusses research in using SDP for OPF for control of voltage magnitude and angle.
- Chapter 10 provides a derivation of a linearized unbalanced power flow model.
- Chapter 11 investigates the accuracy of the LUPFM from Chapter 10.
- Chapter 12 provides discussion of two applications of the LUPFM in OPFs for voltage control, and simulations.
- Chapter 13 provides concluding remarks and a discussion of future work.

Conclusions for this dissertation are drawn in Chapter 14.

Part I

Modeling and Optimal Control of Commercial Office Plug Loads and Battery Storage Systems

Chapter 2

Introduction

The commercial building sector accounts for 36 % of electrical energy consumption in the United States [45]. The advent and increasing ubiquity of smart-meters, tiered and time-of-use pricing has led to research in and advancements of commercial demand response technologies. Many successful efforts in reducing building peak power, and energy consumption, target building HVAC and lighting systems. Building HVAC and lighting are major consumers of electricity. These systems are likely to be centrally controlled and metered.

Plug loads, on the other hand, are often neglected as a resource for demand response. Plug loads can account for 30 % to 50 % of energy consumption in commercial buildings [49, 19]. A plug load is a device that draws electrical power from an outlet for operation. This includes, but not limited to, desktop computers, desktop monitors, fans, persona, heaters, and lamps. Their inclusion as a resource for demand response would greatly increase the flexibility and efficacy of a DR system. Plug loads are usually not utilized for DR for several reasons. The foremost reason is their distributed nature and lack of centralized point of access and control. Plug loads most often lack the necessary intelligence for self-monitoring and control so intermediary devices are needed for these purposes. Finally, the cost to retrofit a building with meterable and controllable outlets is often prohibitive.

Advancements in technologies are enabling plug loads to become a load-shed resource for DR. One such technology is the smart power strip (SPS). An SPS is a device comprised of one or more electrical outlets. The outlets are independently metered and controllable, and enable the user to selectively power connected devices. A second enabling technology is the Energy Information gateway (EIG). An EIG is a software system that interfaces with existing hardware (such as an SPS) for plug load monitoring and control [2, 4, 40]. A third enabling technology is battery storage, specifically office scale battery storage (OSBS) system. An OSBS system provides power to one or more plug loads from outlet power or from its own battery power. Many commercial environments contain one or more OSBS systems for protection against power failure. The increasing adoption and ubiquity of SPSs, EIGs, and OSBS systems in commercial environments prompts the investigation of optimal control of an OSBS system and plug loads as load-shedding resources.

There have been many research efforts focused on the incorporation of plug loads and

battery storage in the context of DR. The authors in [34] present a model predictive control (MPC) framework for coordinated control of laptop battery charging for DR. Their algorithm simplifies to a modified knapsack problem with constraints to avoid over cycling between charging and discharging states. Their simulations show that laptop batteries are a viable resource for load-shifting. In [36] the authors present an MPC framework to reduce peak electricity demand. The authors develop a room thermal model to account for thermal storage and varying tariffs on electricity.

The authors in [17] develop an algorithm for optimal storage use in a demand response context. They propose a simple convex optimization program that does not require pricing information. In [46], the authors use dynamic programming to develop control policies of battery storage for residential demand response. They minimize the residential energy cost taking advantage of predictions of variable pricing signals. Optimal energy storage control policies are developed in [21], where the authors utilize a dynamic programming algorithm. However, many of these efforts do not address the control of battery storage in conjunction with plug loads, or employ simple or generalized battery models.

Much of our previous effort has focused on the development of our own EIG [2], [4], [40]. EIG development was spread across several projects. The initial project was to develop an open-source reference model of an EIG for a residential setting, sponsored by the California Energy Commission (CEC) and the California Institute for Energy and the Environment (CIEE). The EIG was adapted for and deployed in a commercial setting as part of a project with Siemens. Further development includes several iterations and the use of a linear solver for optimal plug load control. We successfully demonstrated the EIG exercising optimal control of plug loads in a commercial office during a load-following (LF) scenario, and validated simulation results with physical experiments [3].

In this work, we investigate optimal control of an OSBS system alongside plug loads for load-shedding. We look at two OSBS systems, investigating the value of controllable charging. We develop a model predictive control (MPC) framework to account for varying load-shed targets and OSBS battery dynamics. An experientially derived battery model is presented. An exhaustive search numerical method is discussed, and simulation results demonstrate the the use of an OSBS alongside plug loads as a load-shed resource. Simulation results also quantify the value of controllable charging for increasing battery capacities. A dynamic programming algorithm is discussed. The algorithm produces control variable look up tables and quantifies OSBS performance. lastly, this work is summarized and plans to carry this work forward are discussed.

Chapter 3

Model Predictive Control of Plug Loads and an Office Scale Battery Storage System

In this work, we focus on control at an office level, as shown in Figure 3.1. Here, an EIG coordinates energy related information and control within an office. The office has one or more SPSs, each with one or more plug loads. The EIG monitors and exerts control over the SPSs. The plug loads connected to each SPS are “actuated” through actuation of the corresponding SPS outlet. A plug load is powered off by powering off its corresponding SPS outlet, and powered on by powering on its corresponding SPS outlet. A plug load that has been powered off, and therefore does not consume outlet power, is considered to have shed its load.

The EIG also monitors and controls an OSBS system that serves a critical load which must always be powered. The OSBS can operate on outlet power or its own battery power. The OSBS sheds its load by running on battery power, so as to not draw power from an outlet. A higher level building entity, the Central Building Authority (CBA) in Figure 3.1, acts as the link from the outside world to the EIG and disseminates load-shedding targets to each office [40]. The office EIG is given a load-shed target over a time horizon by the CBA and seeks to meet this target as closely as possible while minimizing a metric of occupant “inconvenience”. The term inconvenience can be thought of as the occupant discomfort incurred by actuation of plug loads and OSBS battery discharging [3, 41, 42].

We begin our discussion of the MPC formulation by describing three decision variables; one for the plug loads within the EIG domain, and two for an OSBS system. Equation (3.1) gives the binary vector decision variable for plug loads within the EIG domain. As discussed earlier, and in [3], this is also the state of the SPS outlet the plug load is connected to:

$$x_t^i = \begin{cases} 0 & : i^{th} \text{ device powered off at time } t \\ 1 & : i^{th} \text{ device powered on at time } t . \end{cases} \quad (3.1)$$

Symbol	Description	Unit
γ_t	Load-shed target at time t for an office	[W]
c	Vector denoting power consumption of office plug loads	[W]
p_t	Vector denoting inconveniences associated with actuation of office plug loads at time t	[-]
x_t	Vector of binary decision variables denoting power state of office plug loads at time t	[-]
σ_t	Maximum allowable inconvenience associated with office plug loads at time t	[-]
L_T	Total load on OSBS	[W]
S_t	OSBS battery energy at time t	[J]
K	OSBS total battery energy capacity	[J]
Q_t	OSBS battery state of charge (SOC), representing percent of battery energy S_t of total battery capacity K	[%]
P_t	OSBS charging power at time t	[W]
\overline{P}_t	OSBS average charging power over time t to $t + \Delta T$	[W]
u_t	Binary decision variable indicating OSBS outlet power state	[Z]
v_t	Binary decision variable indicating OSBS battery charging state	[Z]
r_t	Inconvenience as a function of SOC at time t	[-]
N	Prediction horizon of model predictive control (MPC)	[-]
β_{pl}	Weighting given to inconvenience of plug load actuation	[W]
β_{soc}	Weighting given to inconvenience of battery discharge	[W]

Table 3.1: Nomenclature for Part I.

The binary decision variable for OSBS power, u_t , is defined by (3.2). This decision variable refers to whether the OSBS is operating on power from its own battery, or operating on power drawn from an outlet. A state of $u_t = 0$ indicates the OSBS operates on its battery power at time t . A state of $u_t = 1$ indicates the OSBS operates on power drawn from an outlet at time t . The term “operates” in this context refers to running the OSBS and servicing any connected plug loads:

$$u_t = \begin{cases} 0 & : \text{OSBS operating on battery power at time } t \\ 1 & : \text{OSBS operating on outlet power at time } t . \end{cases} \quad (3.2)$$

The binary decision variable for OSBS charging state, v_t , is defined by (3.3). A state

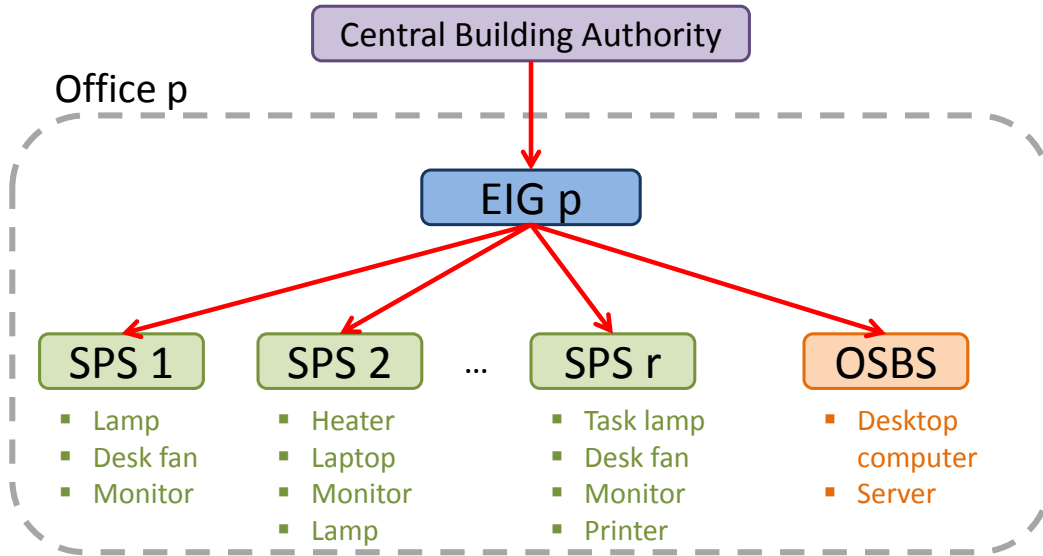


Figure 3.1: Office plug loads and OSBS presided over by an EIG

of $v_t = 0$ indicates the OSBS is not charging its battery at time t , while a state of $v_t = 1$ indicates the OSBS is charging its battery at time t :

$$v_t = \begin{cases} 0 & : \text{OSBS not charging battery at time } t \\ 1 & : \text{OSBS charging battery at time } t . \end{cases} \quad (3.3)$$

In this work we look at two different OSBS systems. The first is based on an uninterruptible power supply (UPS). A UPS automatically charges its battery to and/or maintains it at a full state of charge (SOC) when operating on outlet power. It cannot charge its battery when operating on battery power. Therefore a UPS effectively has one decision variable, such that $u_t = v_t \forall t$. Further modeling of the UPS will be discussed in Chapter 4.

We consider a second OSBS system with the ability to control charging when operating on outlet power, a system we call controllable battery storage (CBS). The CBS can either charge or idle its battery when operating on outlet power, therefore $u_t = 1 \implies v_t \in \{0, 1\}$. Like the UPS, the CBS cannot charge its battery when running on battery power, therefore $u_t = 0 \implies v_t = 0$. When operating on outlet power the CBS can bypass its battery and solely service its plug load(s), such that $u_t = 1, v_t = 0$; or it can both service its load and charge its battery, such that $u_t = 1, v_t = 1$. The relationships between OSBS decision variables are defined in (3.4). OSBS decision variables and OSBS operation states are defined

in Table 3.2:

$$\begin{aligned}
 \text{UPS: } & u_t = 0 \implies v_t = 0 \\
 & u_t = 1 \implies v_t = 1 \\
 \text{CBS: } & u_t = 0 \implies v_t = 0 \\
 & u_t = 1 \implies v_t \in \{0, 1\} .
 \end{aligned} \tag{3.4}$$

OSBS	u_t	v_t	Operation State
UPS	0	0	UPS operating on battery power and not charging its battery.
	1	1	UPS drawing outlet power and charging/maintaining battery to/at 100% SOC.
CBS	0	0	CBS operating on battery power and not charging its battery.
	1	0	CBS drawing outlet power and not charging its battery.
	1	1	CBS drawing outlet power and charging/maintaining battery to/at 100% SOC.

Table 3.2: OSBS decision variables and operation states.

The objective function of the MPC is given in (3.5), in which two terms are summed over a time horizon. The first term is the absolute value of the difference between the target load-shed, and the load-shed from plug loads, $c^T(x_t - 1)$, and the OSBS, $L_T(u_t - 1) + \bar{P}_t v_t$. The charging power is included in this term as battery charging requires drawing power additional to the OSBS load being serviced. It should be noted that as plug load power and OSBS power are discrete, the load-shed target is not likely to be exactly met, and an under-shed or over-shed will likely occur. The second term is the measure of inconvenience or incurred by actuation of plug loads and OSBS battery discharge. In (3.5), $X_{0 \rightarrow N-1}$ refers to the sequence of x_t from $t = 0$ to $t = N - 1$. The same applies for $U_{0 \rightarrow N-1}$ for u_t and $V_{0 \rightarrow N-1}$ for v_t .

$$\begin{aligned}
 \underset{\substack{X_{0 \rightarrow N-1} \\ U_{0 \rightarrow N-1} \\ V_{0 \rightarrow N-1}}}{\text{minimize}} & \sum_{t=0}^{N-1} |\gamma_t + c^T(x_t - 1) + L_T(u_t - 1) + \bar{P}_t(Q_t)v_t| \dots \\
 & + \beta_{pl} p_t^T (1 - x_t) + \beta_{soc} r_t(Q_t) .
 \end{aligned} \tag{3.5}$$

The generalized set of constraints of the MPC is given by (3.6). Here, (3.6a) represents battery state of charge (SOC) dynamics in time as a function of the current SOC, the total load on the OSBS and its operation state. Equation (3.6b) is the average charging power over the timestep from t to $t + \Delta T$ as a function of the current SOC, r_t . A measure of

inconvenience as a function of SOC is given in (3.6c). The derivation of an OSBS model for (3.6a), (3.6b), and (3.6c) will be discussed in the subsequent section:

$$Q_{t+1} = f_{SOC}(Q_t, L_T, u_t, v_t) \quad \forall t \in \{0, N-1\} \quad (3.6a)$$

$$\bar{P}_t = f_P(Q_t) \quad \forall t \in \{0, N-1\} \quad (3.6b)$$

$$r_t = f_r(Q_t) \quad \forall t \in \{0, N-1\} \quad (3.6c)$$

$$Q_t \geq Q_{min,t} \quad \forall t \in \{0, N\} \quad (3.6d)$$

$$p_t^T \leq \sigma_t(1 - x_t) \quad \forall t \in \{0, N-1\} \quad (3.6e)$$

$$x_t \in \chi_t \quad \forall t \in \{0, N-1\} \quad (3.6f)$$

$$x_t^i \in \{0, 1\} \quad \forall i \quad \forall t \in \{0, N-1\} \quad (3.6g)$$

$$u_t \in \{0, 1\} \quad \forall t \in \{0, N-1\} \quad (3.6h)$$

$$v_t \in \{0, 1\} \quad \forall t \in \{0, N-1\} . \quad (3.6i)$$

A time varying minimum SOC constraint is given by (3.6d). This constraint is included as many batteries incur damage at low SOC, and an occupant may want to maintain a minimum SOC as a power failure safeguard. A time varying constraint on the maximum allowable inconvenience incurred from plug load actuation is given by (3.6e). This constraint represents the user's desire to meet the target without incurring too much inconvenience. As in [3], this can also be considered the point at which meeting the load-shed target is no longer as valuable to the occupant as use of their plug loads. A time of use constraint for plug loads is given by (3.6f), indicating the occupants need to use their devices at certain times. Equation (3.6g) enforces the binary nature of plug load operation. Finally (3.6h) and (3.6i) enforce OSBS control states as binary. Equations (3.5) and (3.6) comprise the optimization program for the model predictive controller.

A model of the inconvenience incurred by discharging the UPS was also developed, given by (3.7). While there is a constraint placed on the SOC (3.6), (3.7) in the objective (3.5) serves to penalize low OSBS SOC. The constraints and penalty may arise from concerns about battery life and the desire to always maintain a minimum reserve SOC in case of power failure:

$$r_t(Q_t) = \begin{cases} 1 - \left(\frac{1 - r_r}{Q_r} \right) Q_t : & 0 \leq Q_t \leq Q_r \\ r_r \left(\frac{100 - Q_t}{100 - Q_r} \right) : & Q_r \leq Q_t \leq 100 . \end{cases} \quad (3.7)$$

We chose a piecewise linear function, whose value remains relatively small for high SOC and increases dramatically as the SOC decreases past a cutoff. An example of this function with values $Q_r = 40$ and $r_r = 0.1$ can be seen in Figure 3.2. The penalty function on SOC is likely to be a business decision and so will not be discussed in detail in this work.

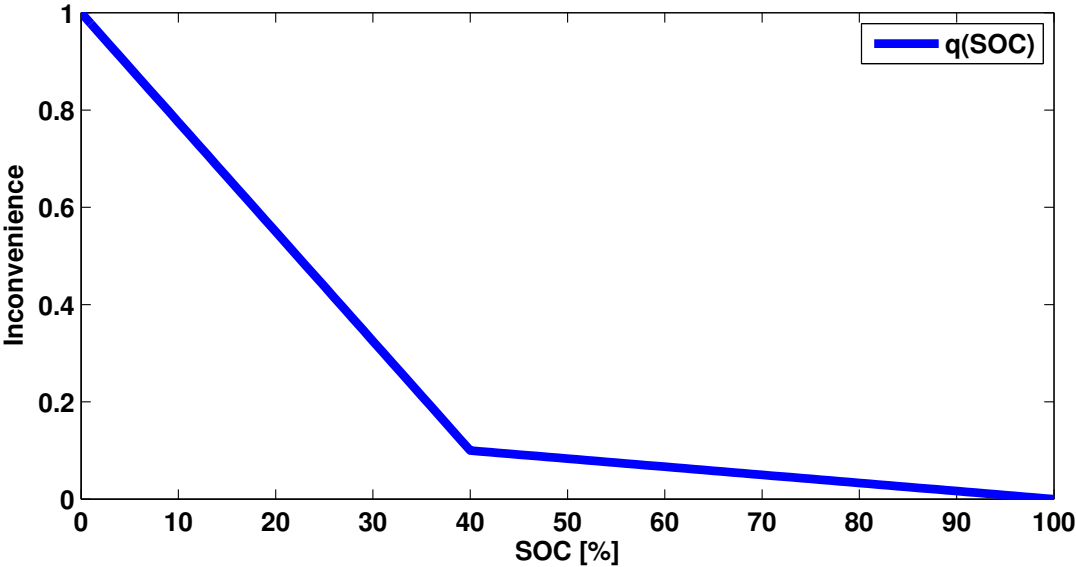


Figure 3.2: Plot of inconvenience function $r(Q_t)$ where $Q_r = 40$ and $r_r = 0.1$.

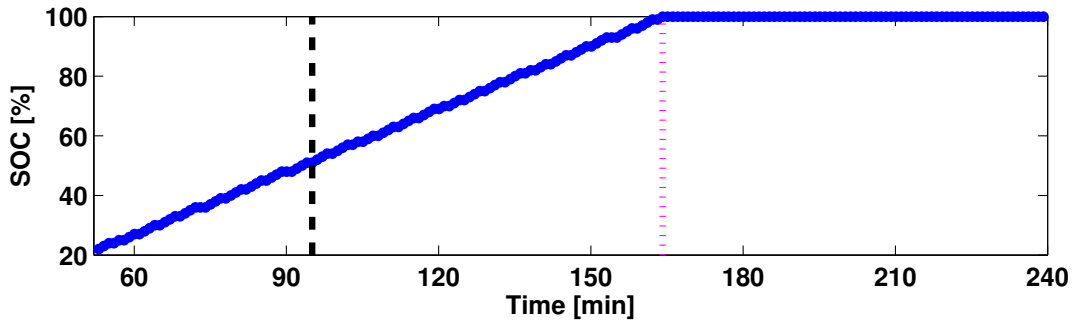
Chapter 4

Experimentally Derived OSBS Battery Model

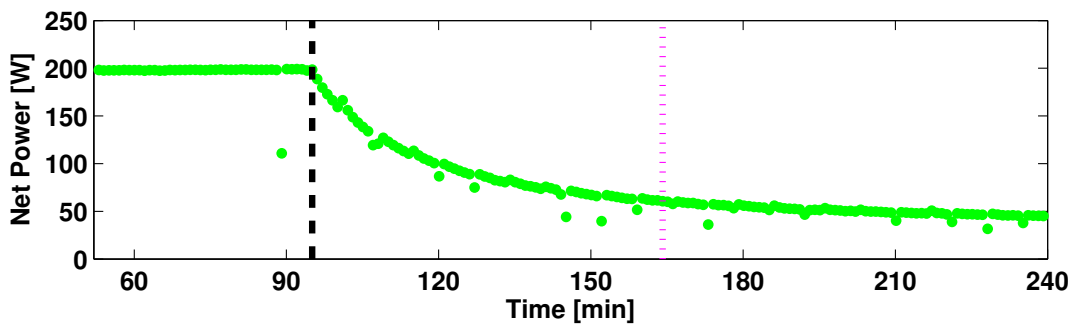
A dynamic model of a commercially available OSBS was experimentally developed for this MPC formulation. The OSBS is an uninterruptible power supply (UPS), the American Power Conversion (APC) Smart UPS 1500RXLM, referred to the APC UPS. The APC UPS operates on its battery power when outlet power is disconnected, until outlet power is restored or the battery reaches a minimum state of charge whereupon it shuts down. When outlet power is connected the APC UPS charges its battery to, and/or maintains its battery, at 100% SOC. The UPS model described in the previous section, and defined by (3.4) is based on the operational nature of the APC UPS. The APC UPS cannot control its charging independently when it is drawing outlet power.

As the system state is the OSBS SOC, we seek to derive a model which captures battery charging power as a function of battery state of charge (SOC). In order to model the APC UPS, it was discharged to several pre-defined SOC by connecting a load and disconnecting outlet power. After the APC UPS reached the target SOC, outlet power was restored and the APC UPS was allowed to charge to 100% SOC. This was done for a range of connected plug loads, including loads of 60 W, 120 W and 180 W. From the APC UPS software, time, percent (%) battery capacity, and battery voltage was recorded in one (1) minute intervals. The power drawn by the APC UPS was recorded in 15 second intervals with an SPS. The power drawn from the APC UPS by the connected plug load was recorded in 15 second intervals by a second SPS. It was observed in all tests that the APC UPS drew an almost constant amount of power additional to the connected load when not charging its battery. This was confirmed by analyzing the power data recorded by the two SPSs. The tests and power data also showed that the connected plug load drew nearly the same amount of power regardless APC UPS operation state, differing by 3 % at maximum.

The APC UPS percent battery capacity was assumed to be its battery SOC. As SPS power trace data was recorded at 15 second intervals, it was linearly interpolated to fit the one minute intervals of the APC UPS data. Thus a set of SOC and power data was created for the APC UPS. The power drawn by the plug load was subtracted from the power drawn



(a) APC UPS battery capacity (SOC) recorded during charging cycle.



(b) APC UPS net power consumption during charging cycle. This is the difference between the measured power drawn by the UPS and that drawn by the loads connected to the UPS.

Figure 4.1: APC UPS charging cycle SOC and net power. In this figure, the black dashed line represents the switch from a period of nearly constant power draw to that of decaying power draw. The magenta dotted line represents the time at which the SOC reaches 100%, assumed to be when charging is complete.

by the APC UPS to obtain the net power consumed by the APC UPS.

Figure 4.1 shows the data for a test in which the UPS was discharged to a 20 % SOC with a nominal load of 180 W. Figure 4.1b shows the SOC increasing in an linear fashion in time. In Figure 4.1b it can be seen that the APC UPS drew an almost constant amount of net power as the its SOC increased from 20 % to 50 %. The net power decreases as the SOC increases from 50 % to 100 %. After the battery reaches, and stays at, 100 % SOC it can be seen that the APC UPS continues to draw a decaying amount of power. As we look to use battery SOC as a state variable and parameterize charging power in SOC, it is assumed that charging is complete once the battery has reached 100 % SOC. The time and data after the APC UPS reaches 100 % SOC is neglected. When the APC UPS initially reaches 100 % SOC it can be seen that it is drawing roughly 60 W net, which is assumed to be the constant UPS operation power. From these observations we arrive at a battery charging model for the UPS, listed below:

1. Constant APC operation power during all power states of 60 W.

2. Connected plug load draws constant power regardless of UPS power state.
3. Constant charging power when SOC between 0% and 50% of 140 W.
4. Charging completed when APC UPS reaches 100 % SOC.

We select a battery energy model in which the SOC Q_t is the percent of total battery energy capacity at time t . Battery energy at time t is represented by S_t . The total battery energy capacity K is the maximum amount of energy the battery can hold, defined as the maximum time the OSBS can operate on battery power (discharge to zero energy) with a nominal load, including operating power. Therefore the SOC Q_t is defined as in (4.1):

$$Q_t = \frac{S_t}{K} \times 100 \% . \quad (4.1)$$

As K is a constant, it is trivial to replace Q_t with S_t in equations. The SOC dynamics are represented as battery energy dynamics, given by (4.2), similar to the model presented in [17]:

$$S_{t+1} = S_t + [(u_t - 1)(L_T) + \eta_c v_t \bar{P}_t(S_t)] \Delta T . \quad (4.2)$$

Battery energy is linear in time, and binary in the control states u_t and v_t . Here, \bar{P}_t denotes the average amount of charging power over from time t to $t + \Delta T$. The variable η_c represents battery charging efficiency, and is chosen as 1. This equation demonstrates the binary nature of the APC UPS, as it either operates on battery power or outlet power. The battery energy model is generalized with both OSBS decision variables to be used for both the UPS and CBS model. The battery energy dynamics can also be written solely in terms of the SOC by using (4.1), resulting in the OSBS SOC dynamics, (4.3):

$$Q_{t+1} = Q_t + \frac{K}{100} [(u_t - 1)(L_T) + \eta_c v_t \bar{P}_t(S_t)] \Delta T . \quad (4.3)$$

Battery charging power was parametrized in battery SOC as in (4.4). This function captures the constant charging power draw from 0 to 50 % SOC, as seen in Figure 4.1. The decaying charging power seen as SOC increases from 50 to 100 % was modeled using a constrained least squares fit. A piecewise linear function was ostensibly chosen to place the optimization program within a linear programming framework:

$$P_t(Q_t) = \begin{cases} 140 : & 0 \leq Q_t \leq 50 \\ 510 - 7.4Q_t : & 50 \leq Q_t \leq 60 \\ 240 - 2.9Q_t : & 60 \leq Q_t \leq 75 \\ 90 - 0.9Q_t : & 75 \leq Q_t \leq 100 . \end{cases} \quad (4.4)$$

The piecewise linear function was constrained such that: $P_t(50) = 140$ to represent the transition between constant and decaying power draw, P_t maintains piecewise continuity, and $P_t(100) = 0$ to represent the completion of charging at 100 % SOC. Figure 4.2 depicts

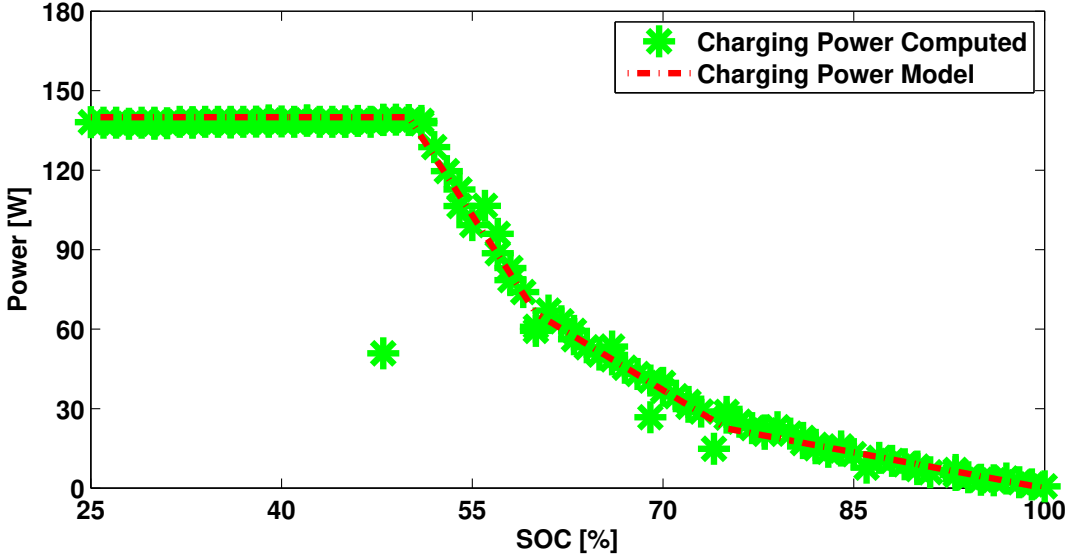


Figure 4.2: APC UPS computed charging power and piecewise linear charging power model.

the charging power model, with 3 linear segments for the decaying charging power regime. The piecewise linear function was also ostensibly selected so that the optimization program would be compatible with a linear programming framework.

The full MPC optimization program, with the SOC as the state, is written as (4.5). It should be noted that this program is nonlinear, binary in its decision variables, and has several switched modes from the battery charging model.

$$\begin{aligned}
& \underset{\substack{X_{0 \rightarrow N-1} \\ U_{0 \rightarrow N-1} \\ V_{0 \rightarrow N-1}}}{\text{minimize}} & \sum_{t=0}^{N-1} |\gamma_t + c^T(x_t - 1) + L_T(u_t - 1) + \bar{P}_t(Q_t)v_t| \dots \\
& & + \beta_{pl} p_t^T(1 - x_t) + \beta_{soc} r_t(Q_t) \\
\text{subject to} & \forall t \in \{0, N-1\} \\
& Q_{t+1} = Q_t + (K/100) [(u_t - 1)(L_T) + \eta_c v_t \bar{P}_t(S_t)] \Delta T \\
& P_t(Q_t) = \begin{cases} 140 : & 0 \leq Q_t \leq 50 \\ 510 - 7.4Q_t : & 50 < Q_t \leq 60 \\ 240 - 2.9Q_t : & 60 < Q_t \leq 75 \\ 90 - 0.9Q_t : & 75 < Q_t \leq 100 \end{cases} \\
& r_t(Q_t) = \begin{cases} ((Q_r - 1 + r_r)/Q_r)Q_t : & 0 \leq Q_t \leq Q_r \\ r_r(100 - Q_t)/(100 - Q_r) : & Q_r \leq Q_t \leq 100 \end{cases} \\
& Q_t \geq Q_{min,t} \\
& p_t^T(1 - x_t) \leq \sigma_t \\
& x_t \in \chi_t \\
& x_t^i \in \{0, 1\} \forall i \\
& u_t \in \{0, 1\} \\
& v_t \in \{0, 1\} .
\end{aligned} \tag{4.5}$$

Chapter 5

An Exhaustive Search Numerical Method and Simulation Results

5.1 Exhaustive Search Numerical Method

The full MPC optimization program is given by (3.5)-(4.4), and concisely presented in (4.5). The MPC objective function contains a binary term $L_T u_t$ and a nonlinear binary term, $u_t \bar{P}_t(Q_t)$. The non-convex piecewise linear charging power model introduces switched modes into the set of MPC constraints. Additionally the decision variables x_t , u_t , and v_t are all binary. The nature of this MPC program precludes it from being solved by many popular solvers as they are not well suited to handle these types of problems.

It is clear that the aforementioned nonlinearities and non-convexities come from the binary nature of OSBS operation and its charging power model. By removing all terms associated with the OSBS from (3.5) and (3.6), the optimization program is reduced to a binary integer linear program (BILP) quite similar to that in [3]. This can be leveraged to solve the optimization program by an exhaustive search.

We denote a general sequence of u_t from $t = 0$ to $N - 1$ as $U_{0 \rightarrow N-1}$, and that of v_t as $V_{0 \rightarrow N-1}$. For any combination of $U_{0 \rightarrow N-1}$ and $V_{0 \rightarrow N-1}$, and Q_0 , the sequences $S_{1 \rightarrow N}$ and $Q_{1 \rightarrow N}$ can be calculated by (4.2). Using (4.4) the sequence $\bar{P}_{0 \rightarrow N-1}$ can be computed, as can $r_{0 \rightarrow N-1}$ with (3.7). Treating these sequences as exogenous parameters, like the load-shed target γ_t , the optimization problem is reduced to an N step BILP as in(5.1):

$$\begin{aligned}
 & \underset{X_{0 \rightarrow N-1}}{\text{minimize}} && \sum_{t=0}^{N-1} \left| \gamma_t + c^T (x_t - 1^n) + (L_T) (u_t^\diamond - 1) + \bar{P}_t^\ddagger(Q_t) v_t^\diamond \right| \dots \\
 & && + \beta_{pl} p_t^T (1^n - x_t) + \beta_{soc} r_t^\ddagger(Q_t) \\
 & \text{subject to} && p_t^T (1^n - x_t) \leq \sigma_t \quad \forall t \in \{0, N - 1\} \\
 & && x_t \in \chi_t \quad \forall t \in \{0, N - 1\} \\
 & && x_t \in \{0, 1\} \quad \forall t \in \{0, N - 1\} .
 \end{aligned} \tag{5.1}$$

Here, the superscript \diamond denotes the decision variables from the combination of $U_{0 \rightarrow N-1}$ and $V_{0 \rightarrow N-1}$, and the superscript \ddagger denotes the calculated values for the combination. The decision variable $X_{0 \rightarrow N-1}$ is the sequence of x_t for $t = 0$ to $N - 1$.

This method discretizes the portion of the state space of (3.5) and (3.6) representing the OSBS, keeping the decision variables representing plug loads free. The simplification removes the nonlinearities and non-convex switched battery model from the optimization program. The optimization program of (3.5) and (3.7) is reduced to a BILP (5.1) of dimension nN , where n is the number of plug loads, for which many open source and commercial solvers are available. As in (3.4), it can be seen that the UPS effectively has one decision variable, therefore $U_{0 \rightarrow N-1} = V_{0 \rightarrow N-1}$. The CBS has two decision variables, thus $U_{0 \rightarrow N-1}$ and $V_{0 \rightarrow N-1}$ may differ. Not all combinations of $U_{0 \rightarrow N-1}$ and $V_{0 \rightarrow N-1}$ will be feasible from CBS operation and (3.4). The optimal decision variable sequences $X_{0 \rightarrow N-1}^*$, $U_{0 \rightarrow N-1}^*$, and $V_{0 \rightarrow N-1}^*$ are obtained by comparing every combination of every permutation of $U_{0 \rightarrow N-1}$ and $V_{0 \rightarrow N-1}$. This is done by comparing the BILP objective value for the each combination. Thus, the algorithm for solving the MPC optimization problem is as follows:

1. Grid u_t and v_t over all possible permutations of $U_{0 \rightarrow N-1}$ and $V_{0 \rightarrow N-1}$.
2. Iterate over all sequences $U_{0 \rightarrow N-1}$ (UPS), or all combinations of sequences $U_{0 \rightarrow N-1}$ and $V_{0 \rightarrow N-1}$ (CBS).
 - For CBS only, check feasibility of current sequence combination with regard to CBS operation, and proceed only if feasible.
3. Evolve OSBS dynamics (4.2) and (4.4) for the current decision variable sequence (UPS) or combination (CBS) over horizon $t = 0$ to $N - 1$.
4. Check feasibility of current sequence or combination with regard to minimum SOC constraint (3.6d) over horizon $t = 0$ to $N - 1$ (UPS and CBS)
5. Solve BILP (5.1) if current sequence or combination is feasible.
6. Compare current BILP objective to best obtained thus far:
 - If better, store objective, $U_{0 \rightarrow N-1}$, $V_{0 \rightarrow N-1}$ and $X_{0 \rightarrow N-1}$ as best thus far.
 - Otherwise, discard.
7. Return optimal solution after BILP solved for all feasible sequences (UPS) or combinations (CBS).

This method returns the optimal decision variable sequences for plug loads and the UPS or CBS over the time horizon $t = 0$ to $N - 1$. For a prediction horizon of N steps, there are 2^N permutations of $U_{0 \rightarrow N-1}$. The BILP must be solved for all feasible, with regard to SOC, permutations of $U_{0 \rightarrow N-1}$ to obtain the optimal decision variables sequences of $X_{0 \rightarrow N-1}^*$ and $U_{0 \rightarrow N-1}^*$. The CBS has two decision variables, and therefore two sequences, there are

$2^{2N} = 4^N$ possible combinations of the permutations of $U_{0 \rightarrow N-1}$ and $V_{0 \rightarrow N-1}$. As there are three CBS operation states, there are 3^N permutations feasible with regard to CBS operation. Not all permutations will be feasible with regard to the minimum SOC constraint.

It should be noted that this method can quickly become intractable with an increasing MPC prediction horizon and/or number of OSBSs. For an office with a single UPS and prediction horizon $N = 10$, the algorithm would need to compare 2^{10} possible sequences, solving the BILP of dimension $10n$ for each feasible sequence. For an EIG domain with m UPSs, there are 2^{mN} possible combinations of sequence permutations. Though a powerful computer may be able to handle longer prediction horizons, this method may still deliver suboptimal results. Small timesteps may cause the temporal length of the prediction horizon to be too short. The inability to predict far enough into the future may cause “shortsighted” policies to be implemented, due to load-shed target changes outside the prediction horizon. Longer timesteps would ameliorate this problem, however this would mean averaging the OSBS charging power and battery dynamics over a longer time period. The exponential computational scaling associated with this method preclude both longer prediction horizons and greater dimensionality in the number of OSBSs per EIG.

5.2 Simulation Results using Exhaustive Search Method

We now present results from simulations of an EIG exerting control of office plug loads and an OSBS. The simulations are for a 360 minute period with a load-shed period of 180 minutes from 60 to 240 minutes. Outside the load-shed period, rule based control is applied to the OSBS, such that the UPS and CBS charge their batteries to 100% SOC. During the load-shed period the MPC is employed to obtain the optimal decision variable sequences. The MPC optimization program is solved at each timestep setting the current timestep as $t = 0$. The MPC implements the first decision variable of each sequence, x_0^* , u_0^* , and v_0^* for the duration of the timestep.

We consider two scenarios for simulations; a DR scenario and a load-following (LF) scenario. A static load-shed target is assigned by the CBA to the EIG in the DR scenario. In the LF scenario, the load-shed target is variable in time. The load-shed targets are shown in Figure 5.1. Each scenario is simulated with a range of battery capacities (run times), from 60 minutes to 210 minutes in 30 minute increments. The minimum allowable SOC is 10% to allow for prolonged operation on battery power.

The UPS and CBS service a load of 120 W, and their operating power is 60 W as per the APC UPS model. Therefore when operating on battery power their load-shed is 180 W. The plug load inconvenience weighting β_{pl} is 10, and the SOC inconvenience weighting β_{soc} is chosen as 5. The maximum allowable inconvenience σ_t is 4 during load-shed periods, and 0 otherwise. The maximum prediction horizon is chosen as $N = 6$ to balance the performance of the MPC algorithm and computational expediency. The prediction horizon decreases

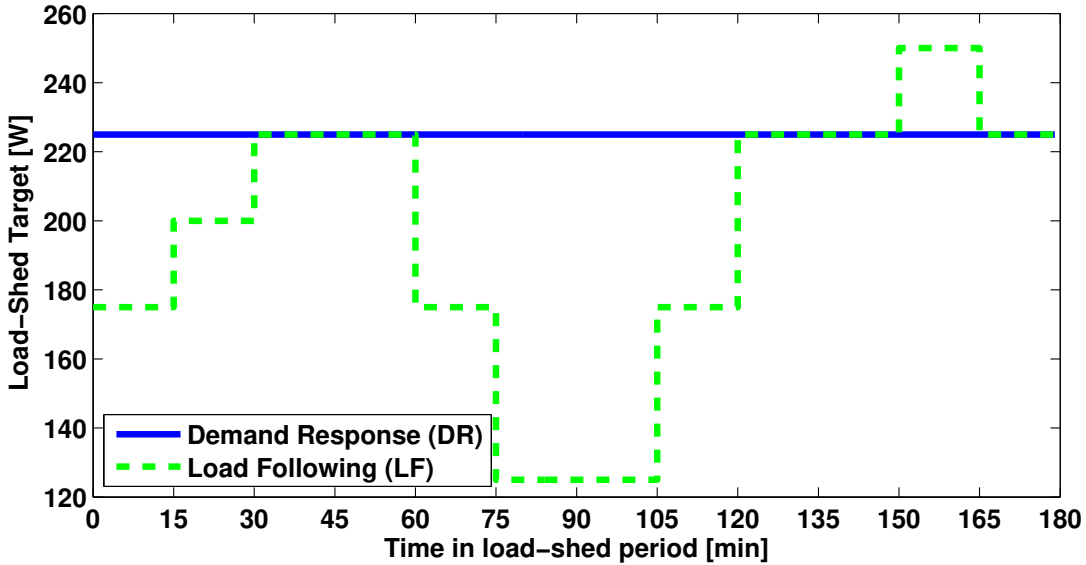


Figure 5.1: Demand response (DR) and load-following (LF) scenario load-shed targets.

in length nearing the end of the event, so as to not include non-load-shed periods into the optimization program. The timestep length is 15 minute, giving a 90 minute temporal length to the prediction horizon.

Plug load	Power [W] - c_i	Inconvenience - p_i
Large Fan	30	2
Desktop Monitor	60	3
Desk Lamp	60	2
Desk Lamp (CFL)	15	2
Laptop	40	2
Small Fan	15	3
Laptop	40	1
Desk Lamp	50	2

Table 5.1: Plug loads used in simulations.

As in [3, 42], we select an assortment of plug loads commonly found in offices. The plug loads are assumed to have static power consumption when operating, and constant priority values. Table 5.1 lists the plug loads, their respective power consumptions and inconvenience value. The SOC inconvenience function $r_t(Q_t)$ is given by (3.7) with values of $Q_q = 40$ and $r_r = 0.1$, as in Figure 3.2. In each scenario, we assume the UPS or CBS operates on outlet

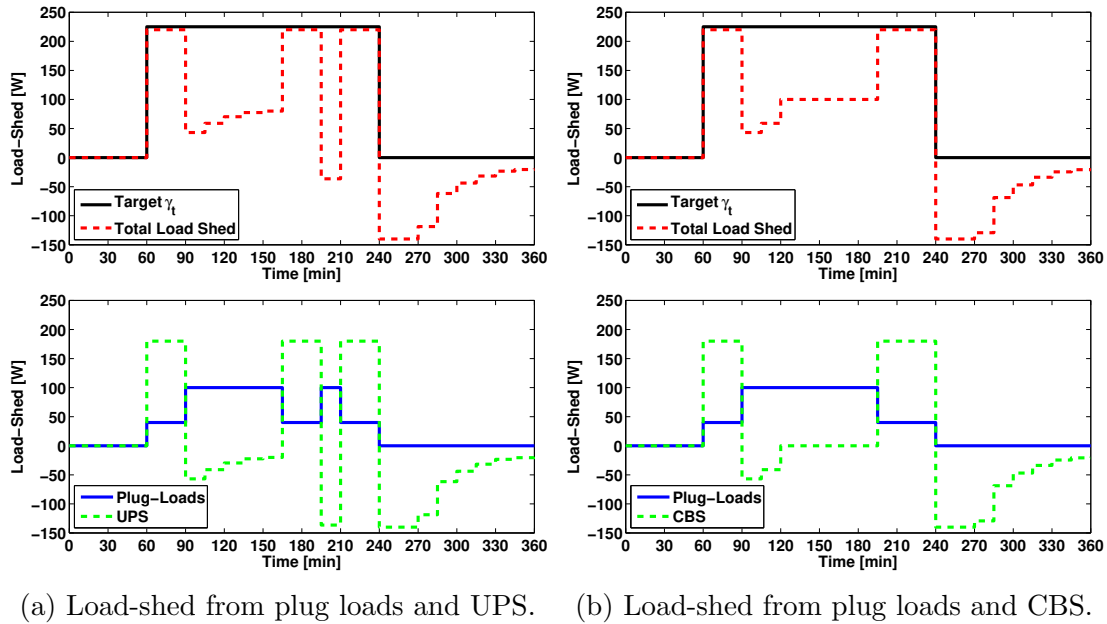


Figure 5.2: Total and component load-shed of plug loads and an OSBS for static target scenario.

power and is allowed to charge before and after the load-shed period. The UPS or CBS begin the simulation with 100 % SOC.

Model Predictive Control of Plug Loads and an OSBS for Load-Shedding

In this section we discuss results from simulations a with a static load-shed target of 225W, shown in Figure 5.2. The simulations demonstrate the MPC algorithm providing control of the plug loads and a UPS or CBS with battery run time of 90 minutes. It should be noted that the negative load-shed following the load-shed period is due to rule based control such that the OSBS charges its battery.

Figure 5.2a shows the total and component load-sheds from plug loads and a UPS. Figure 5.2b shows the total and component load-sheds from plug loads and a CBS. In each simulation it can be seen that when the UPS or CBS operates on battery power, shedding its 180 W load, the plug loads comprise approximately 40 W of load-shed to meet the load-shed target as closely as possible. When the UPS or CBS operates on outlet power, 100 W of load-shed is achieved through plug load actuation to closer meet the load-shed target. However the plug loads are never used to their full load-shed potential as a result of the maximum inconvenience constraint.

In Figure 5.2a, it can be seen that the UPS and plug loads combined load-shed is within 10 W of the target when the UPS operates on battery power. After 30 minutes of operating

on battery power, the UPS charges its battery for 75 minutes. The UPS then operates on battery power for 30 minutes before returning to outlet power. At this point the UPS is drawing 140 W to charge, while the plug loads contribute 100 W to the load-shed, thus there is actually a negative load-shed of 40 W.

In Figure 5.2b, it can be seen that the CBS operates on battery power for the first 30 minutes of the load-shed period. It then operates on outlet power and charges for 30 minutes, before operating on outlet power without charging for 75 minutes. During this time, the plug loads constitute the load-shed of 100 W. For the last 45 minutes of the event, the CBS operates on battery power, and the plug loads constitute 40 W of load-shed.

In Figure 5.2, it can be seen that the UPS runs on battery power for a total of 90 minutes, while the CBS does so for 75 minutes. The UPS charges its battery for more time than the CBS, during the times either OSBS draws outlet power. The time from 120 minutes to 195 minutes in which the CBS operates on outlet power without charging its battery highlights that doing so is optimal for certain conditions.

Demand Response Scenario

In the demand response scenario, a static load-shed target of 225W was assigned over the 180 minute load-shed period. Simulation results for three battery capacity cases, for both the UPS and CBS, are shown in Figure 5.3. The figures show the load-shed target and the total load-shed achieved when using plug loads and either the UPS (red, left column) or CBS (blue, right column). It can be seen that the UPS and CBS generally exhibit similar behavior at the end of the DR period independent of batter capacity. They both reserve and/or charge to accrue enough SOC to operate on battery power such that the battery is maximally discharged by the end of the DR period.

Figures 5.3a and 5.3b show simulation results for a UPS and CBS with 60 minute battery run times, respectively. Both operate on outlet power from the beginning of the event, with plug loads constituting the load-shed of 100 W. Starting 45 minutes prior to the end of the event, both the UPS and CBS operate on battery power, shedding their load. During this time plug loads contribute 40 W of load-shed, instead of the prior 100 W. Similar to the results from Figure 5.2 the plug load inconvenience constrains prevents their load-shed potential from being fully realized when the OSBS operates on outlet power.

Simulation results for the 120 minute run time case are shown in Figure 5.3c and 5.3d. It can be seen that the UPS and CBS exhibit similar behavior during the DR period. They both operate on battery power for the initial 15 minutes of the DR period, then operate on outlet power. The UPS charges its battery as it must, while the CBS does not. At 75 minutes from the end of the DR period, both the UPS and CBS operate on battery power, shedding their respective loads.

Figure 5.3e and Figure 5.3f show the results from the 180 minute run time case for the UPS and CBS, respectively. The UPS and CBS both shed their loads by operating on battery power for the first 60 minutes of the DR period. They then both operate on outlet power for 45 minutes. During this time the UPS charges its battery and the CBS does not. Both the

UPS and CBS operate on battery power for the last 75 minutes of the DR period, shedding their respective loads.

From these simulations, it can be seen that the optimal control policy is for the OSBS to operate on battery such that its battery is discharged to the minimum allowable SOC at the end of the event. The simulations suggest that it is optimal to operate on battery power during the beginning of the event as well for larger battery capacities. This is somewhat counter-intuitive as it would require the UPS to charge if it returns to outlet power during the event. These simulations also clearly show that it is often optimal for the CBS to idle its battery when operating on outlet power.

Capacity [min]	J_{UPS} [W]	J_{CBS} [W]	CBS Improvement [%]
60	1441	1441	0
90	1331	1262	5.2
120	1089	1024	6.0
150	976	884	9.4
180	762	607	20.3
210	600	466	22.3

Table 5.2: Comparison of UPS and CBS performance for DR scenario.

Table 5.2 compares the performance of the UPS and CBS from DR scenario simulations. Performance is measured as the sum of the MPC objective function over the DR period, evaluated with the implemented optimal decision variables for each 15 minute timestep, as in (5.2):

$$J = \sum_{t=60}^{240} |\gamma_t + c^T (x_t^* - 1) + L_T (u_t^* - 1) + \bar{P}_t(Q_t)v_t^*| + \beta_{pl}p_t^T (1 - x_t^*) + \beta_{soc}r_t(Q_t) . \quad (5.2)$$

The UPS and CBS perform identically with the smallest battery capacity, as seen in Figure 5.3. As battery capacity increases, the CBS increasingly outperforms the UPS. This intuitive result comes from the ability of the CBS to control battery charging. Battery charging constitutes a negative amount of load-shed by the OSBS and detracts from the load-shed provided by the plug loads. These results show that the addition of controllable charging becomes increasingly valuable as OSBS battery capacity increases. This is also seen in Figure 5.3 as the CBS does not charge its battery when operating on outlet power during the DR period.

Load-Following Scenario

In the load following (LF) scenario, a time varying load-shed target is assigned, with targets ranging from 75W to 225W over a 180 minute period. The load-shed target has two

peaks, one toward the beginning of the LF period and one near the end of the LF period, with a valley during the middle. Simulation results are shown in Figure 5.4.

Figure 5.4a (UPS) and Figure 5.4b (CBS) show the different behaviors of the UPS and CBS for the 60 minute battery run time case. The UPS operates on outlet power for the first 30 minutes of the LF period, then operates on battery power for 30 minutes, shedding its load. It then operates on outlet power and charges its battery for 60 minutes. The UPS then switches to battery power for 30 minutes, resumes outlet power for 15 minutes, then operates on battery power for the last 15 minutes of the LF period. In contrast, the CBS operates on outlet power for the first 15 minutes of the LF period, then sheds its load by running on battery power for 30 minutes. During this time, two different amounts of load-shed are realized by the plug loads. The CBS then operates on outlet power while idling its battery for 105 minutes. It then again sheds its load during the second target peak. The CBS simulation, in Figure 5.4b, show operation on outlet power without battery charging is optimal for the CBS. Furthermore, the UPS actually caused negative load-sheds at times when charging its battery, as charging power was greater than the maximum plug load load-shed available.

Figures 5.4c and 5.4d give simulation results for the UPS and CBS, respectively, each with a 120 minute battery run time. The UPS operates on battery power during the initial 15 minutes of the LF event, returning to outlet power for the next 15. It then operates on battery power during the first target peak for 45 minutes. While the target is comparatively lower, the UPS operates on outlet power, charging its battery. It then operates on battery power, shedding its load, for 15 minutes before charging for 15 minutes. Finally the UPS sheds its load for the last 45 minutes of the event. The CBS, however, operates on battery power for the first 60 minutes of the LF period. It then operates on outlet power without charging for 90 minutes, while the load-shed target is decreased. It then sheds its load for the last 30 minutes of the event.

It can be seen in Figures 5.4e and 5.4f that the UPS and CBS operate on battery power or outlet power in an almost identical fashion. The UPS operates on battery power for 30 minutes while the load-shed target is at its lowest point. The CBS does so for 45 minutes without charging. The UPS runs on battery power for the last 75 minutes of the LF event, while the CBS does so for 60 minutes. As the UPS charges its battery while running on outlet power, its SOC is higher than the CBS when switching to battery power toward the end of the LF period.

The LF simulation again shows that CBS operation on outlet power without charging is optimal as opposed to CBS operation on outlet power and charging. Table 5.3 compares the performance of the UPS and CBS in the LF scenario. Much like the DR scenario, the CBS outperforms the UPS in its ability to meet a load-shed criteria in conjunction with plug loads. Similar to the DR scenario, the performance of the CBS increases with battery capacity. Again, this is due to the CBS being able to run on outlet power and not charge its battery, while the UPS must charge if using outlet power.

Capacity [min]	J_{UPS} [W]	J_{CBS} [W]	CBS Improvement [%]
60	1183	1118	5.5
90	1100	968	12
120	876	736	16
150	683	556	18.6
180	450	357	20.7
210	389	256	34.2

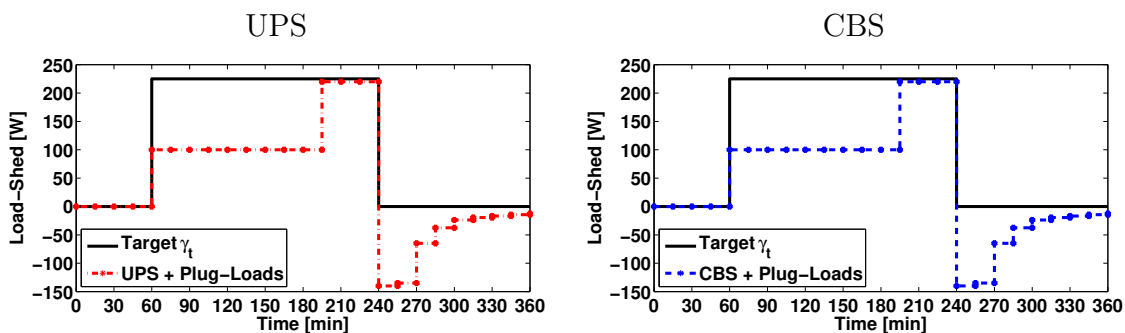
Table 5.3: Comparison of UPS and CBS performance for LF scenario.

Remarks on Exhaustive Search Method and Simulations

Simulation results show that the CBS offers better performance than the UPS for both the DR and LF scenarios. The performance gap increases as battery size increases. This intuitive result comes as the CBS offers more flexibility as it can run on outlet power and not charge its battery. Simulation results also highlight that it is very often optimal for the CBS to utilize this feature during a DR or LF event. This can be seen in Figure 5.4, where the CBS does not charge its battery while running on outlet power, when the load-shed target is relatively low. Of course, with a low enough load-shed target it may be optimal to charge the CBS battery, especially if plug loads can be actuated to account for the charging power drawn.

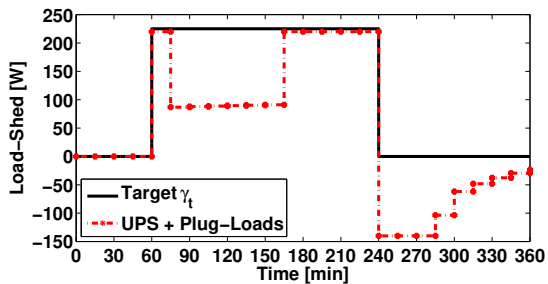
While the exhaustive search method delivers an optimal control policy at each timestep, it suffers from several drawbacks. The main drawback is the length of the prediction horizon N . The optimal control policy may not take important future events into account. As the prediction horizon N needs to be small enough for computational expediency, the length of the timesteps also becomes an issue. With a timestep that is too small, the temporal length of the prediction horizon may be too short to capture important future events and/or to capture different battery charging regimes. This can be remedied by increasing timestep length. However the OSBS charging power is then averaged over a longer time. These caveats associated with the exhaustive search method prompt the search for a different method for solving the optimization program, which will be discussed in the next chapter.

DEMAND RESPONSE SCENARIO SIMULATIONS

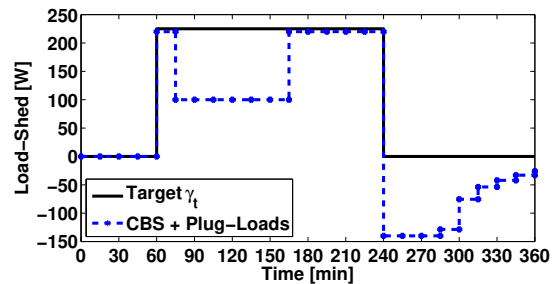


(a) Simulation of DR scenario; UPS with 60 minute battery capacity

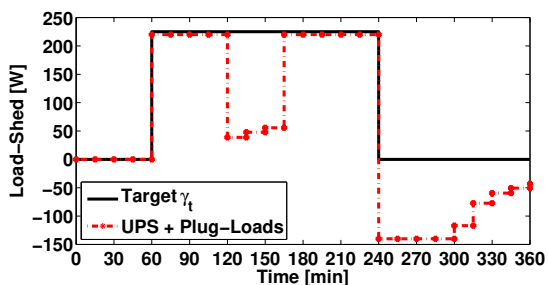
(b) Simulation of DR scenario; CBS with 60 minute battery capacity



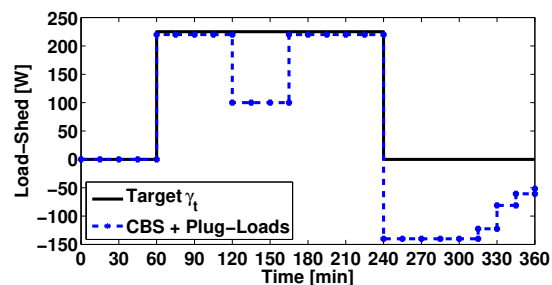
(c) Simulation of DR scenario; UPS with 120 minute battery capacity



(d) Simulation of DR scenario; CBS with 120 minute battery capacity



(e) Simulation of DR scenario; UPS with 180 minute battery capacity



(f) Simulation of DR scenario; CBS with 180 minute battery capacity

Figure 5.3: Demand response scenario simulation results for UPS and CBS, with battery capacities of 60, 120 and 180 minutes.

LOAD-FOLLOWING SIMULATIONS

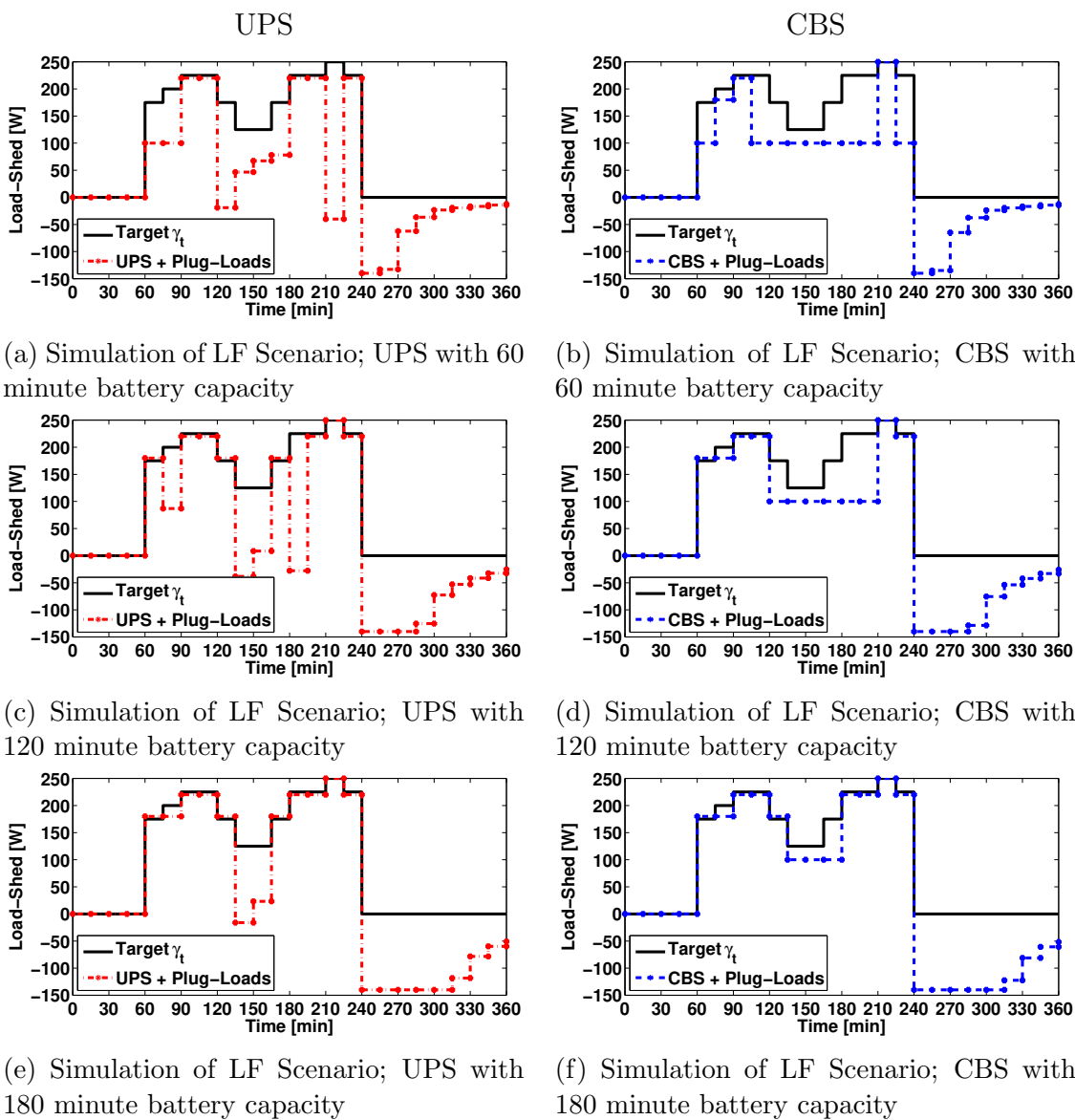


Figure 5.4: Load-following scenario simulation results for UPS and CBS, with battery capacities of 60, 120 and 180 minutes.

Chapter 6

A Dynamic Programming Algorithm for the MPC Optimization Program and Simulation Results

6.1 Dynamic Programming Algorithm

Dynamic programming is a powerful optimization tool, that can be used to solve many complex problems not amenable to linear or quadratic programs. The basic tenet is to dissolve a problem into a series of smaller problems. As in [21], [46] it is used to optimize based on a set of predicted signals and/or events. The MPC formulation is amenable to being formulated as a dynamic program, addressing several of the problems associated by the aforementioned exhaustive search method. The system state is the OSBS battery energy S_t , and by linear scaling the SOC Q_t . The UPS effectively has one binary decision variable, and therefore has two operation states: operation on outlet battery where $u_t = v_t = 0$, and operation on outlet power where $u_t = v_t = 1$. The CBS has two decision variables, and three operational states: operation on battery power where $u_t = v_t = 0$, operation on outlet power without charging where $u_t = 1, v_t = 0$, and operation on outlet power with charging where $u_t = v_t = 1$.

The algorithm for solving the DP is as follows: The SOC Q is gridded as a discrete set of points. At the last timestep, $t = N$, the boundary condition is computed for each point in the SOC grid as $r_N(Q_N)$ and is stored as the terminal cost $V_N(Q_N)$. The algorithm proceeds to the previous timestep, $t = N - 1$. At each SOC grid point Q^j the OSBS dynamics (4.2) and (4.4) are evolved over one timestep for the two (UPS) or three (CBS) operation states. For Q_t^j , this gives the battery energy $S_{t+1}(S_t^j, u_t, v_t)$, and SOC $Q_{t+1}(Q_t^j, u_t, v_t)$ by (4.1) at the next time step, and the average charging power over the timestep $\bar{P}_t(Q_t^j)$. The feasibility of each OSBS operation state is checked using $Q_{t+1}(Q_t^j, u_t, v_t)$ in the minimum SOC constraint (3.6d). If an operation state is feasible, a binary integer linear program (6.1) gives the optimal plug load decision variable $x_t^*(Q_t^j, u_t, v_t)$ as a function of the OSBS SOC

and operation state for the current timestep:

$$\begin{aligned}
 x_t^*(Q_t^j, u_t, v_t) = \operatorname{argmin}_{x_t} \quad & \{ |\gamma_t + c^T (x_t - 1) + L_T (u_t - 1) + \overline{P}_t(Q_t^j)v_t| + \beta_{pl}p_t^T (1 - x_t) \} \\
 \text{subject to} \quad & p_t^T (1 - x_t) \leq \sigma_t \\
 & x_t \in \chi_t \\
 & x_t^i \in \{0, 1\} \quad \forall i .
 \end{aligned} \tag{6.1}$$

The stage cost is computed for each operation state, as in (6.2), using the average charging power and the optimal plug load states $x_t^*(Q_t, u_t, v_t)$ for the operation state:

$$\begin{aligned}
 g_t(Q_t^j, u_t, v_t) = & |\gamma_t + c^T (x_t^{j*}(Q_t^j, u_t, v_t) - 1) + L_T (u_t - 1) + \overline{P}_t(Q_t^j)v_t| \dots \\
 & + \beta_{pl}p_t^T (1 - x_t^{j*}(Q_t^j, u_t, v_t)) + \beta_{soc}r_t(Q_t^j) .
 \end{aligned} \tag{6.2}$$

The cost-to-go function (6.3) is evaluated for feasible OSBS operation states, using a linear interpolation to calculate $V_{t+1}(Q_{t+1}(Q_t^j, u_t, v_t))$. The OSBS operation state, and therefore decision variables, that minimizes $v_t^j(Q_t^j)$ is chosen as the optimal:

$$v_t^*(Q_t^j) = \min_{u_t, v_t} \{ g_t(Q_t^j, u_t, v_t) + V_{t+1}(Q_{t+1}(Q_t^j, u_t, v_t)) \} . \tag{6.3}$$

Evaluating (6.3) gives the optimal OSBS decision variables $u_t^*(Q_t^j)$ and $v_t^*(Q_t^j)$ at time t and for SOC point Q_t^j . This also gives the optimal plug load decision variable $x_t^*(Q_t^j)$. The optimal decision variables are saved in lookup tables indexed by time and SOC. The cost-to-go $v_t^*(Q_t^j)$ is stored for the current timestep and SOC. This algorithm proceeds backwards in time until the initial timestep, at which point it is terminated. The DP algorithm is also outlined below:

1. At $t = N$, initialize cost-to-go function $V_N(Q_N)$ using boundary condition of $r_N(Q_N)$ for all SOC grid points.
2. Proceed backward one timestep and loop through all SOC grid points.
3. At the current SOC grid point Q_t^j , compute $S_{t+1}(Q_t^j)$ by (4.2), $Q_{t+1}(Q_t^j)$ by (4.1), $\overline{P}_t(Q_t^j)$ by (4.4), and $r_t(Q_t^j)$ by (3.7) for each operation state.
4. Check feasibility of operation state with regard to battery SOC (3.6d).
 - If operation state is infeasible and $v_t = 0$, set cost-to-go for operation state to infinity.
 - If operation state is infeasible and $v_t = 1$, solve BILP (6.1) and compute stage cost (6.2) for operation state.
 - If operation state is feasible, solve BILP (6.1) and compute stage cost (6.2) for operation state.

5. Select optimal OSBS and plug load operation state for SOC grid point via (6.3).
6. Store optimal decision variables $u_t^*(Q_t^j)$, $v_t^*(Q_t^j)$, $x_t^*(Q_t^j)$, and cost-to-go $v_t^*(Q_t^j)$ for current SOC.
7. Repeat steps 3 through 6 for all SOC grid points at current time t .
8. Repeat steps 2 through 7 progressing backward in time through first timestep $t = 1$. Terminate after.

Casting the MPC as a dynamic program eliminates several of the problems of the exhaustive search method. While the DP algorithm has advantages in solving the MPC optimization program, it also has drawbacks. The most recognizable is the preclusion of solving an optimization program with multiple OSBS systems within a domain. For k OSBS systems, each with SOC grid of size n , there are n^k possible SOC combinations. At each of these combinations every possible control state over the k OSBS systems must be compared, up to k^3 . It can clearly be seen that this method is not scalable in the number of OSBS systems, as computation scales exponentially.

6.2 Simulation Results using Dynamic Programming Algorithm

In this section we present simulation results for two scenarios. The first scenario is of a demand response (DR) event in which a static load-shed target is assigned to the EIG from a higher building level authority. The second is a load-following (LF) scenario where a time varying load-shed target is assigned. The load-shed targets for both scenarios are shown in Figure 5.1 for simulation periods (event length) of 180 minutes. The timestep length is one (1) minute.

The simulations are of an EIG coordinating the listed plug loads and either a UPS or CBS. As in the simulations for the exhaustive search method, we select a variety of plug loads representing commonly found devices in commercial offices [3, 42]. The plug loads and their respective power consumption and occupant assigned static inconvenience value are listed in Table 5.1.

The UPS and CBS have identical parameters and battery models. We look at one battery capacity for these simulations; 180 minutes. The plug load served by the OSBS is 120 W, and the OSBS operating power is 60 W. The total load on the OSBS is $L_T = 180$ W. The minimum SOC is 25%, to simulate battery longevity considerations and to represent a reserve of battery energy desired by the occupant. The plug load inconvenience weighting is $\beta_{pl} = 25$, and SOC inconvenience weighting is $\beta_{soc} = 50$. The SOC inconvenience function $r_t(Q_t)$ is given by (3.7) with values of $Q_q = 40$ and $r_r = 0.1$, and can be seen in Figure 3.2. In each scenario, we assume the OSBS operates on outlet power before and after the load-shed period, however we do not limit the initial SOC to 100 % SOC.




OSBS	Region	Operation State	$u_t(Q_t)$	$v_t(Q_t)$
UPS & CBS		Battery power — No charging	0	0
CBS		Outlet power — No charging	1	0
UPS & CBS		Outlet power — Charging	1	1

Table 6.1: OSBS control states in Figure 6.1 and Figure 6.3.

Demand Response Scenario and Load-Following Scenarios

Figure 6.1 and Figure 6.3 show the optimal OSBS operation states derived via simulations for the DR and LF scenarios, respectively. In each figure, the x axis is simulation time, starting at the beginning of the DR or LF event. The battery SOC grid is on the y axis. In each figure, the red region represents the operation state of UPS or CBS running on battery power: $u_t(Q_t) = v_t(Q_t) = 0$. Green regions represent the state where the CBS operates on outlet power and does not charge: $u_t(Q_t) = 1, v_t(Q_t) = 0$. Blue regions represent the operation state where the UPS or CBS draws outlet power and charges its battery: $u_t(Q_t) = v_t(Q_t) = 1$. The regions and corresponding decision variables are also explained in Table 6.1.

Figure 6.1 show the optimal operation state and decision variables for the DR scenario simulation. It can be seen in Figure 6.1a that the optimal UPS control policy is to initially operate on outlet power, then switch to battery power so as to discharge the battery to the minimum SOC by the end of the event. A line separating the state space between outlet and battery power is defined as the SOC needed to power the UPS for the remaining time in the DR event. This is perhaps more accurately views as the run time of the UPS operating on battery power starting at an SOC. Similarly, as shown in Figure 6.1b, the optimal control policy for the CBS is to operate on outlet power, then switch to battery power such that the battery will be completely discharged at the end of the event. However, the CBS optimal charging policy is to charge the battery only when its initial SOC is less than or equal to 40%, during the initial 45 minutes of the DR event. Figure 6.1b shows the optimality of CBS operation on outlet power without charging, and of charging for low initial SOCs. Both the UPS and CBS charge when the SOC is less than 25 % in order to satisfy the minimum SOC constraint.

A comparison of the performance between the UPS and CBS for the DR scenario is given by Figure 6.2. In Figure 6.2a, the overall performance is plotted for the full range of initial SOCs. Here, performance is measured as the total cost at the initial timestep for each SOC grid point, $V_0(Q_0)$ for $Q_0 = 0$ to $Q_0 = 100$. The total cost includes the difference between the load-shed target and achieved load-shed from OSBS and plug loads, and the weighted inconvenience functions. Figure 6.2a shows that CBS performance is better across the full

range of initial SOC's, and that CBS performance nears that of the UPS as the initial SOC reaches 100 %. The percent improvement in performance is given by Figure 6.2b, in which the gap in performance decreases with initial SOC's greater than 40 %. The peak at 40 % is likely due to the SOC inconvenience function, (3.6c), which has a knee when $Q = 40$. At 100 % initial SOC, the CBS has a performance increase of 3.0 %. This is due to the similar optimal control policies of both devices and the UPS not charging its battery for a prolonged period with high initial SOC's.

Simulation results for the LF scenario are displayed in Figure 6.3. Figure 6.3a shows the optimal UPS control policy, which is to run on battery power for higher initial states of charge, then to charge the battery when the load-shed target is reduced during the middle of the event. As the load-shed target increases, the optimal policy is to operate on battery power for as long as possible. Similar results are found for the CBS, seen in Figure 6.3b. For higher initial SOC's the CBS operates on battery power, while for initial SOC's less than 40% the CBS operates on outlet power and charges its battery. The CBS operates on outlet power without charging during the middle of the event while the load-shed target is lowered. It then switches to battery power for the remainder of the event to discharge its battery to the minimum allowable SOC by the end of the event.

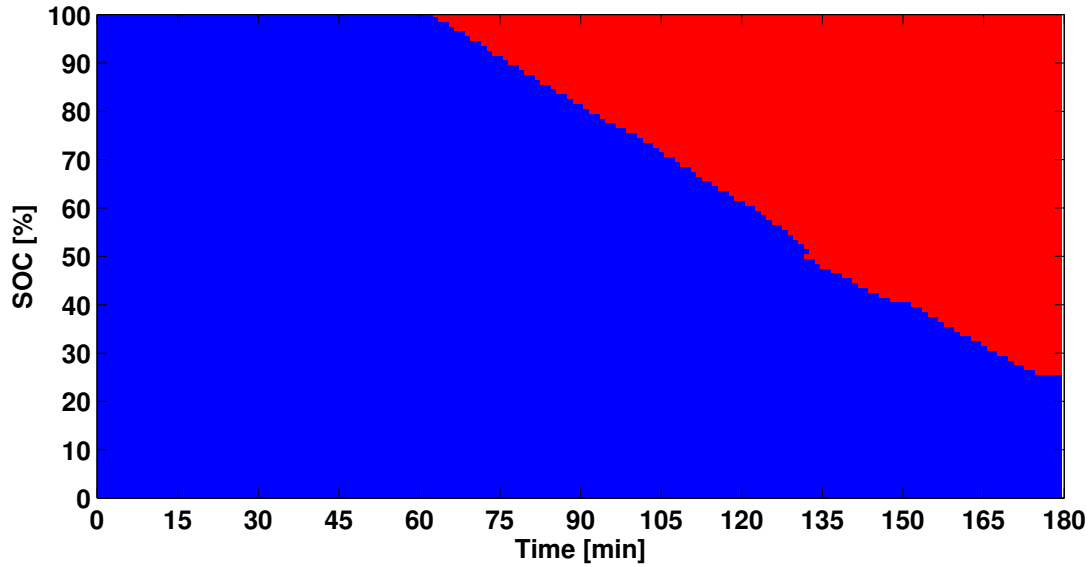
Figure 6.4 gives a comparison between UPS and CBS performance for the LF scenario. In Figure 6.4a it can be seen that the CBS has better performance across the entire range of initial SOC's. Figure 6.4b shows that the CBS outperforms the UPS to its greatest extent with an initial SOC of 40 %. At 100 % initial SOC, the CBS performs 6.9 % better than the UPS, due to the CBS ability to control its charging when drawing outlet power.

These simulation results demonstrate the utility of DP for optimal scheduling of plug loads and OSBS systems as load-shed resources. Implementation of DP allows for a longer prediction horizons with smaller timesteps. The DP algorithm provides the user with lookup tables for OSBS and plug load control policies. Furthermore, the DP algorithm provides a measure of performance of an OSBS system in conjunction with plug loads as a load-shed resource.

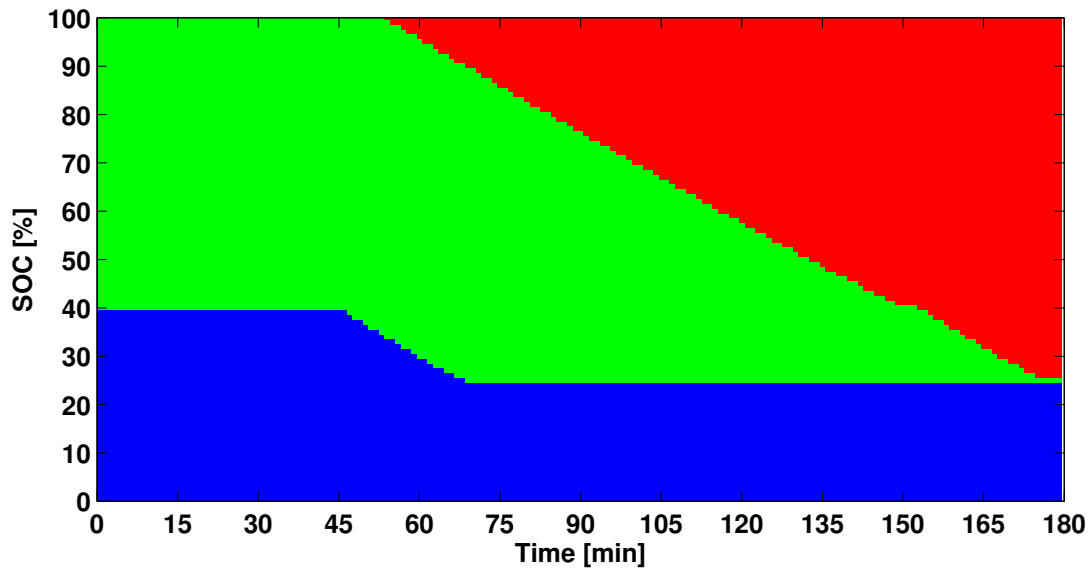
Remarks on Dynamic Programming Method and Simulations

It is clear that reformulating the MPC optimization program as a dynamic program abates several of the problems inherent in the exhaustive search method. Dynamic programming allows for larger number of timesteps in the prediction horizon. In turn, this allows for shorter timestep temporal length and less averaging of battery dynamics. However the use of DP precludes the inclusion of more than one OSBS system in the current formulation.

The dynamic programming algorithm provides valuable lookup tables for OSBS and plug load control. The tables contain optimal decision variable values for a given time and SOC. The DP algorithm also gives a numerical value to the cost of using an OSBS alongside plug loads for load shedding. The DP algorithm exhibits much advantage over the exhaustive search algorithm, and thus should be used for to control OSBS systems and plug loads for optimal load-shedding.

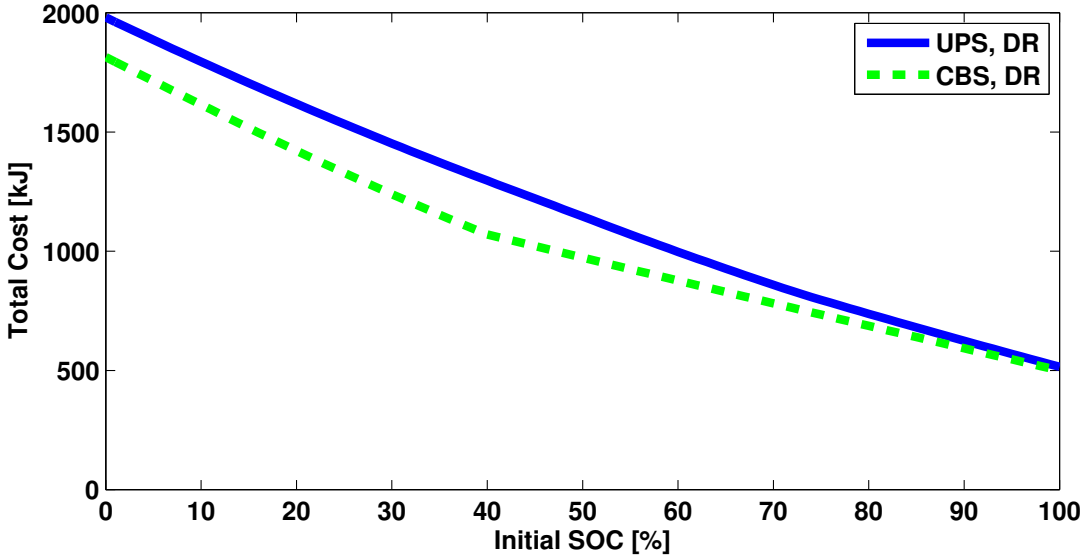


(a) Optimal UPS operation state lookup table for DR scenario.

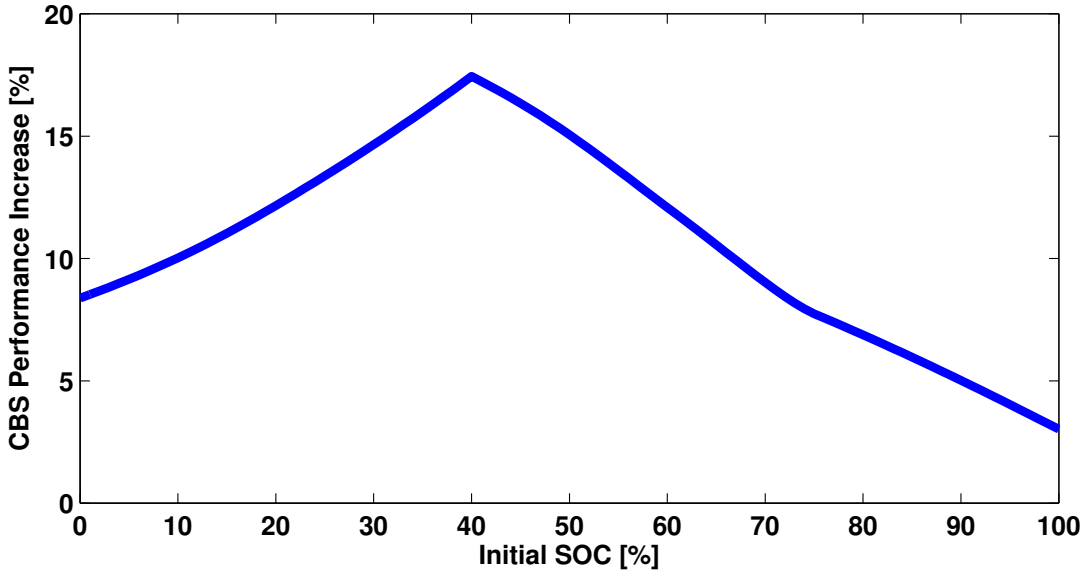


(b) CBS operation state lookup table for DR scenario.

Figure 6.1: OSBS operation states for DR scenario. See Table 6.1 for explanation of regions.

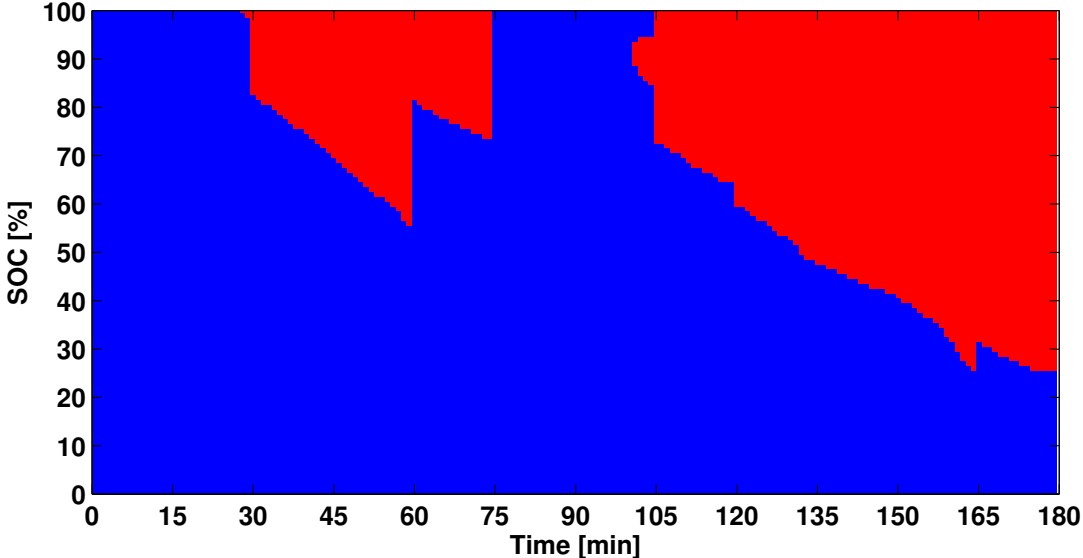


(a) Comparison between UPS and CBS performance for DR scenario. Performance is given as $V_0(S_0)$ as defined in (6.3)

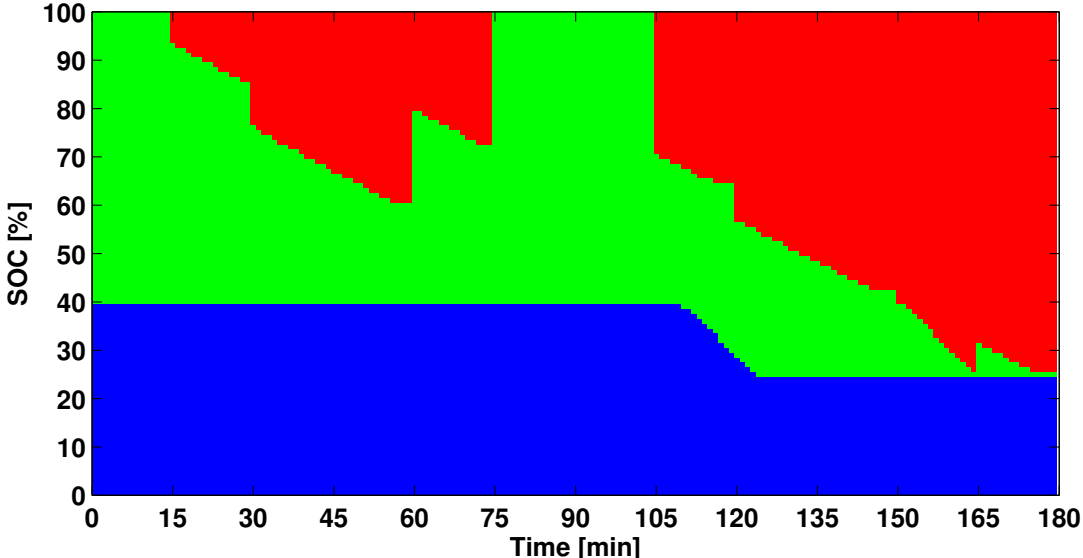


(b) CBS performance increase as percent of UPS performance for DR scenario.

Figure 6.2: Performance comparison between UPS and CBS for DR scenario.

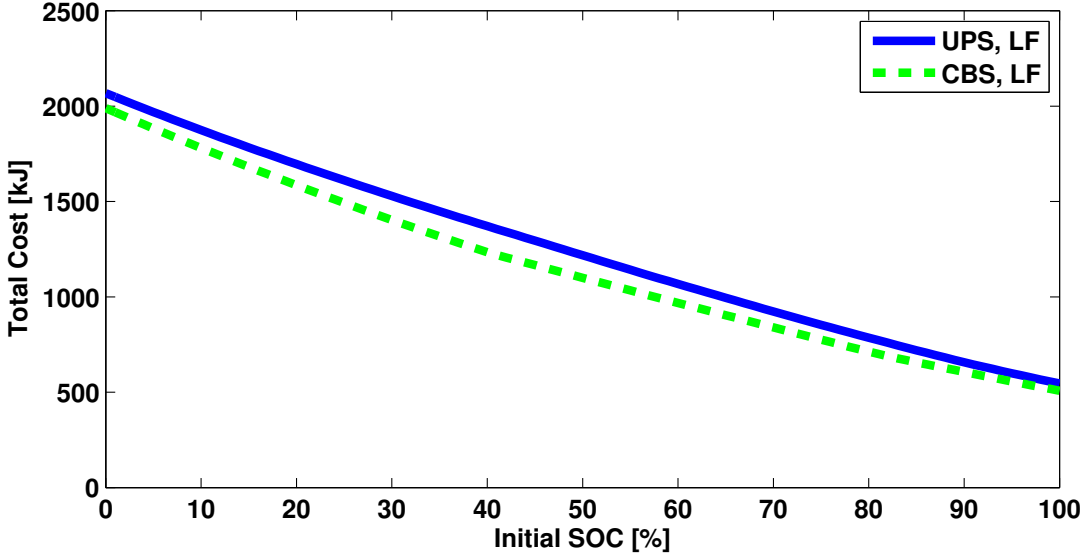


(a) Optimal UPS operation state lookup table for LF scenario.

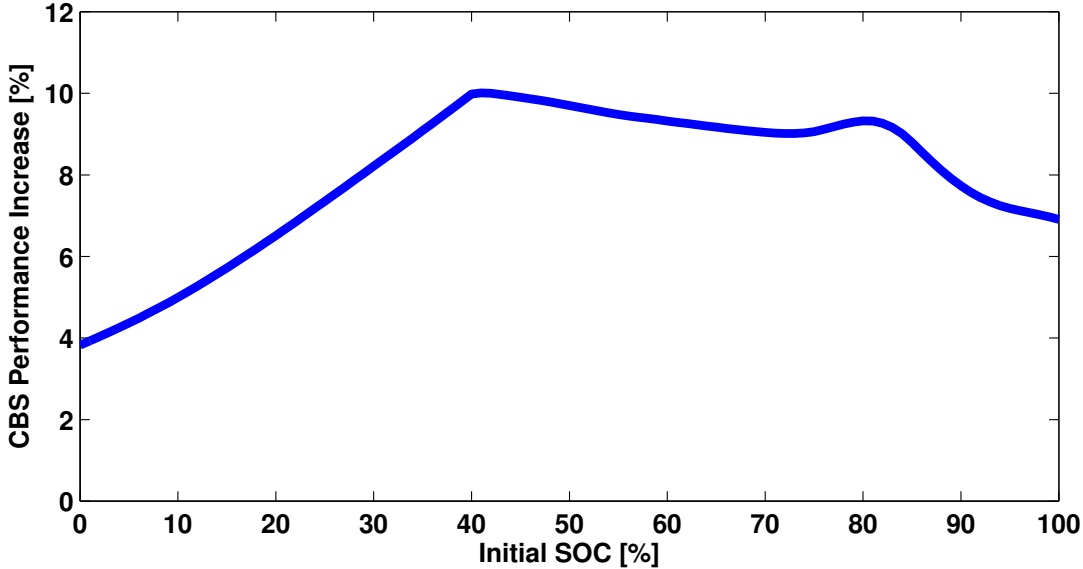


(b) Optimal CBS operation state lookup table for LF scenario.

Figure 6.3: OSBS operation states for LF scenario. See Table 6.1 for explanation of regions.



(a) Comparison between UPS and CBS performance for LF scenario across initial SOC's. Performance is given as $V_0(Q_0)$ as defined in (6.3)



(b) CBS performance increase as percent of UPS performance for LF scenario.

Figure 6.4: Performance comparison between UPS and CBS for LF scenario.

Chapter 7

Concluding Remarks and Future Work

In this work we present a framework for optimal control of plug loads and battery storage in the context of load-shedding. We discuss the impetus for this work, enabling technologies and previous research efforts in the field. The use of EIG and SPS systems in a commercial office is discussed and a model predictive controller is formulated. This MPC balances meeting a load-shedding objective with the inconvenience and discomfort associated with doing so. An OSBS battery model derived from experimental observation is discussed. Two OSBS systems are presented, with their differences in physical key physical and mathematical model difference highlighted.

The complexity of the MPC optimization program is discussed. A simplification enables the use of an exhaustive search method which is outlined. Simulation results for a demand response and a load-following scenarios are presented. Simulations show the value of battery storage to complement plug loads as a load-shed resource. Simulations show that it is optimal to run on battery power so as to discharge it at the end of a DR or LF event. The results quantify the increasing value of controllable charging with battery capacity. We found that for the smallest battery capacities, the UPS and CBS offer identical performance. The CBS outperforms the UPS 22.3 % in the DR scenario, and 34.2 % in the LF scenario. The drawbacks of this numerical method, which may preclude its practical implementation, are also discussed.

A second numerical method for the optimization program is presented. This dynamic programming algorithm eliminates several of the drawbacks of the exhaustive search method, but not without its own. The DP algorithm is discussed, as are simulations performed using it. The simulation results demonstrate that it is optimal for both the UPS and CBS to discharge their batteries to the minimum SOC by end of the event. The UPS should charge/maintain its battery to/at 100 % SOC during the beginning of the event. The CBS should only charge its battery if it has a low SOC during the beginning of the event. The CBS very often operates on outlet power without charging. These results prove the need for controllable charging. We found that for 100 % initial SOC, CBS performance is 3.0 %

better than the UPS in the DR scenario, and 6.9 % better in the LF scenario.

We plan to continue this work in two key areas. The first is to investigate other methods for solving the MPC optimization program, including binary relaxations. A second method is the reformulation of the battery model with special ordered sets to allow for casting the MPC as a linear program. The second area in which this work will be continued is experimentation with available hardware to verify simulation results.

Part II

Modeling of Unbalanced Power Flow and Optimal Control of Distributed Energy Resources for Grid Reconfiguration

Chapter 8

Introduction

The proliferation of new types of sensors into the electric power distribution system is providing deeper insights into the operation of the grid and is driving innovation around new paradigms for system management. Among the many new sensing devices being deployed in the distribution grid, distribution synchrophasors provide a suite of new functionality that could serve to better inform the process of managing Distributed Energy Resources (DER). Distribution PMUs not only collect “traditional” system telemetry (such as voltage and current magnitudes) on sub-second time intervals, but provide access to voltage and current phase *angles* as well. These devices are now becoming more commonplace and are either manifesting as standalone units [30] or are being incorporated into other system components [44].

The growing presence of distribution PMUs indicates that sufficient infrastructure may be in place in future grids to support control activities that make decisions based on feeder voltage measurements. In fact, a small, but growing, number of control applications that utilize phase angle measurements have started to appear in literature. The work of [35] proposed the use of voltage angle measurements to curtail over-generation of renewables. Additionally, the authors of [47] considered voltage angle thresholds as criteria to connect renewable generation. Both works refer to this control activity as “Angle Constrained Active Management”, or ACAM.

An application for distribution PMU data may be useful is enabling fast and safe switching of network elements. The ability to disconnect and reconnect microgrids and quickly reconfigure distribution networks are two important abilities of future distribution networks [15, 16, 37]. Network Reconfiguration and microgrid islanding/reconnection may require switching actions.

Preventing arcing and or large transient currents when opening or closing a switch is important for safe and reliable grid operation, and to prolong the life of existing protection equipment. To open a switch, the magnitude of the current, and therefore power, flowing through the line must not be over safe limits, as well as the switch action to occur at a current zero-crossing. To close a switch, the voltage difference across it end must be sufficiently small to prevent arcing and large current surges.

As such, distribution system operators (DSOs) require power injection at reconfiguration locations to close switches and minimize impact on grid components and power quality. Switching actions may be scheduled beforehand, but for a contingency case a mobile generation that provides power to the correct location may be dispatched.

The advent and proliferation of distributed energy resources present an opportunity to power sections of a network and facilitate network reconfiguration at a potentially faster timescale than current practices. With proper location of DER and sufficient power/energy resource it may be possible to control voltage and current phasors at critical points in the network from the DSO, without needing to dispatch a mobile generation unit or engineering team.

The literature on control and optimization of DER to for more sophisticated operation distribution networks is quite vast. Many of the works in this field seek are motivated from an economic standpoint, and works in which the aim is to *directly control* voltage phasors is sparse.

Many works in the field study the use of semidefinite programming (SDP), semidefinite relaxations (SDR), and convex relaxations in optimal power flow (OPF) problems. Works on this topic range from studying the geometry of the problem [23], to conditions under which a convex relaxation is likely to be tight [22], to limitations on the application of SDPs [24], to solving distributed SDP OPFs for unbalanced networks [11]. It should be noted that much of the earlier literature considers balanced networks, and only recently have unbalanced networks been studied [11, 50].

Recently, other works in the field have studied using approximate power models, including linearized models [6, 14, 39], and quadratic models [13]. Other works have considered optimal DER dispatch in a model-free framework [1, 5].

To enabled control strategies for regulation of voltage phasors, we build upon a linear model of unbalanced power flow by adding a relation between voltage angle differences and line real and reactive power. Previous works have considered linear models of unbalanced power flow [14, 39], but have only provided considered voltage magnitude. To our knowledge, this work is the first to include voltage angle on an unbalanced network, and in which an OPF is capable of regulating the entire voltage phasor (magnitude and angle).

In this work, we investigate OPF formulations for control of voltage magnitude and phase angle through DER dispatch, for the purposes of opening or closing a switch on a distribution network. First in Section 8.1, pertinent nomenclature and equations are presented and explained. In Chapter 9, semidefinite programming for OPF formulations is discussed. Section 9.2 provides an overview of the state of research on SDP OPFs and presents an argument for the need of other OPF formulations. In Section 9.3, we derive SDP OPFs for the control of voltage magnitude and phase angle, and discuss preliminary simulations on simple networks.

In Chapter 10, a linearized unbalanced power flow model (LUPFM) that incorporates voltage angle is derived. The accuracy of the LUPFM is investigated in Chapter 11 for benchmark IEEE test feeders. Two applications of the LUPFM are discussed in Chapter 12, with Section 12.1 presenting an OPF for balancing voltage magnitude across multiple

phases at networks nodes, and Section 12.2 presenting an OPF for minimizing voltage phasor difference across the ends of an open switch.

8.1 Nomenclature, Definitions, and Preliminaries

Symbol	Description	Unit
\mathcal{N}	Set of network nodes in network	
\mathcal{P}_n	Set of phases that exist at node n	
\mathcal{E}	Set of lines (edges) in network	
\mathcal{P}_{mn}	Set of phases that exist on line (m, n)	
\mathcal{G}	Set of nodes with energy resources	
V_n^ϕ	Voltage phasor at node n on phase ϕ	[p.u.]
\mathbf{V}_n	Vector of voltage phasors at node n	[p.u.]
E_n^ϕ	Square magnitude of voltage at node n on phase ϕ	[(p.u.) ²]
\mathbf{E}_n	Vector of square magnitudes of voltage at node n	[(p.u.) ²]
θ_n^ϕ	Phase angle of voltage phasor at node n on phase ϕ	[-]
Θ_n	Vector of phase angles of voltage phasors at node n	[-]
i_n^ϕ	Load current of phase ϕ at node n	[p.u.]
\mathbf{i}_n	Vector of load currents at node n	[p.u.]
$Z_{mn}^{\phi\phi}$	Impedance of line (m, n) on phase ϕ	[p.u.]
$Z_{mn}^{\phi\psi}$	Impedance of line (m, n) between phases ϕ and ψ	[p.u.]
\mathbf{Z}_{mn}	Impedance matrix of line (m, n)	[p.u.]
$Y_{mn}^{\phi\phi}$	Admittance of line (m, n) on phase ϕ	[p.u.]
$Y_{mn}^{\phi\psi}$	Admittance of line (m, n) between phases ϕ and ψ	[p.u.]
\mathbf{Y}_{mn}	Admittance matrix of line (m, n)	[p.u.]
I_{mn}^ϕ	Current phasor on phase ϕ on line (m, n)	[p.u.]
\mathbf{I}_{mn}	Vector of current phasors on line (m, n)	[p.u.]
$P_{mn,m}^\phi$	Real power on line (m, n) on phase ϕ at node m	[p.u.]
$\mathbf{P}_{mn,m}$	Vector of real power on line (m, n) at node m	[p.u.]
$P_{mn,n}^\phi$	Real power on line (m, n) on phase ϕ at node n	[p.u.]
$\mathbf{P}_{mn,n}$	Vector of real power on line (m, n) at node n	[p.u.]
$Q_{mn,m}^\phi$	Reactive power on line (m, n) on phase ϕ at node m	[p.u.]
$\mathbf{Q}_{mn,m}$	Vector of reactive power at node m	[p.u.]

$Q_{mn,n}^\phi$	Reactive power on line (m, n) on phase ϕ at node n	[p.u.]
$\mathbf{Q}_{mn,n}$	Vector of reactive power on line (m, n) at node n	[p.u.]
$S_{mn,m}^\phi$	Phasor of complex power on line (m, n) on phase ϕ at node m	[p.u.]
$\mathbf{S}_{mn,m}$	Vector of complex power phasors at node m	[p.u.]
$S_{mn,n}^\phi$	Phasor of complex power on line (m, n) on phase ϕ at node n	[p.u.]
$\mathbf{S}_{mn,n}$	Vector of complex power phasors at node n	[p.u.]
d_n^ϕ	Complex demand on phase ϕ at node n	[p.u.]
\mathbf{d}_n	Vector of complex demands at node n	[p.u.]
s_n^ϕ	Complex load on phase ϕ at node n	[p.u.]
\mathbf{s}_n	Vector of complex loads at node n	[p.u.]
u_n^ϕ	DER real power dispatch on phase ϕ at node n	[p.u.]
\mathbf{u}_n	Vector of DER real power dispatch at node n	[p.u.]
v_n^ϕ	DER reactive power dispatch on phase ϕ at node n	[p.u.]
\mathbf{v}_n	Vector of DER reactive power dispatch at node n	[p.u.]
w_n^ϕ	DER complex dispatch on phase ϕ at node n	[p.u.]
\mathbf{w}_n	Vector of DER complex dispatch at node n	[p.u.]
e_n^ϕ	Fixed voltage magnitude reference for phase ϕ at node n	[(p.u.) ²]
\mathbf{e}_n^ϕ	Vector of fixed voltage magnitude references at node n	[(p.u.) ²]
$(\cdot)^T$	Transpose	
$(\cdot)^*$	Complex conjugate	
$(\cdot)^H$	Complex conjugate transpose	

Table 8.1: Nomenclature for Part II.

Let $\mathcal{T} = (\mathcal{N}, \mathcal{E})$ denote a graph representing an unbalanced distribution feeder, where \mathcal{N} is the set of nodes of the feeder and \mathcal{E} is the set of line segments. There are $N+1$ nodes on the network including the node representing a transmission line or point of common connection (PCC), which may be indexed by 0 or ∞ and assigned the number 0. Nodes will be indexed by their name, and assigned a number ranging from 1 to N . We treat the PCC as an infinite bus, decoupling interactions in the downstream distribution system from the rest of the grid. While the substation voltage may evolve over time, we assume this evolution takes place independently of loading conditions and DER control actions in \mathcal{T} .

Each node and line segment can have up to three phases, labeled a , b , and c . Phases are referred to by $\phi \in \{a, b, c\}$ and $\psi \in \{a, b, c\}$. Let \mathcal{P}_m be the set of phases at node m , and \mathcal{P}_{mn} be the set of phases of line (m, n) . If phase ϕ is present at node m , then at least one

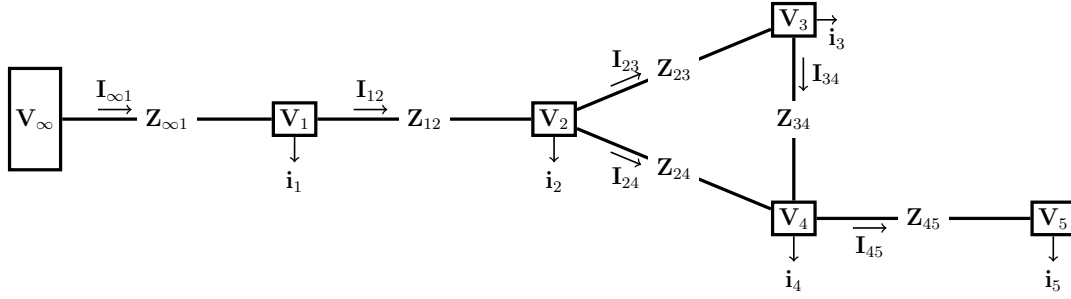


Figure 8.1: Simple network showing node voltages V_m , node currents i_m , line currents I_{mn} , and line impedances Z_{mn} .

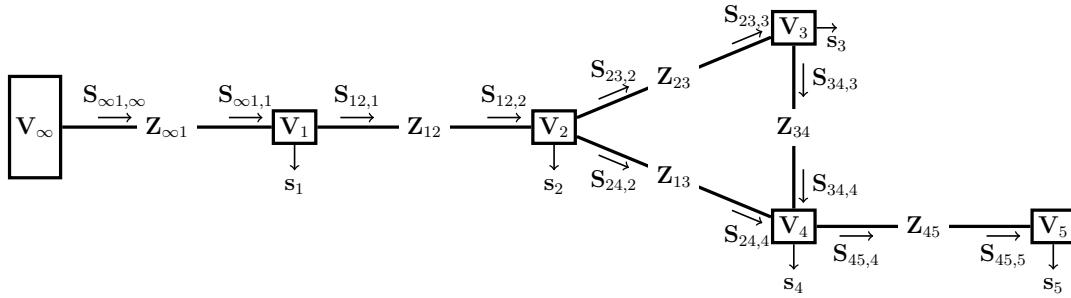


Figure 8.2: Diagram of simple network showing node voltage V_m , net node demand s_m , line impedance Z_{mn} , and line complex power referenced to line transmitting node $S_{mn,m}$ and line receiving node $S_{mn,n}$.

line connected to m must contain phase ϕ , such that:

$$m \in \mathcal{N} \Rightarrow \mathcal{P}_m = (\cup_{l:(l,m) \in \mathcal{E}} \mathcal{P}_{lm}) \cup (\cup_{n:(m,n) \in \mathcal{E}} \mathcal{P}_{mn}) .$$

If line (m, n) exists, its phases must be a subset of the phases present at both node m and node n , such that:

$$(m, n) \in \mathcal{E} \Rightarrow \mathcal{P}_{mn} \subseteq \mathcal{P}_m \cap \mathcal{P}_n ,$$

However $\mathcal{P}_m \cap \mathcal{P}_n \neq \emptyset$ does not necessarily mean $\exists(m, n) \in \mathcal{E}$.

The voltage phasor for phase ϕ at node n is $V_n^\phi \in \mathbb{C}$, and the vectors of voltage phasors for node n is $\mathbf{V}_n = [V_n^a \ V_n^b \ V_n^c]^T \in \mathbb{C}^3$. The current phasor for phase ϕ on line (m, n) is $I_{mn}^\phi \in \mathbb{C}$, and the voltage of current phasors on line (m, n) is $\mathbf{I}_{mn} = [I_{mn}^a \ I_{mn}^b \ I_{mn}^c]^T \in \mathbb{C}^3$. The current phasor for phase ϕ at node n is $i_n^\phi \in \mathbb{C}$, and the vector of current phasors for node n is $\mathbf{i}_n = [i_n^a \ i_n^b \ i_n^c]^T \in \mathbb{C}^3$.

We define $V_n^\phi = 0$ if $\phi \notin \mathcal{P}_n$, $I_{mn}^\phi = 0$ if $\phi \notin \mathcal{P}_{mn}$, and $Z_{mn}^{\phi\psi} = Z_{mn}^{\psi\phi} = 0 \ \forall \psi \in \{a, b, c\}$ if

$\phi \notin \mathcal{P}_{mn}$, such that:

$$\begin{aligned}
\phi \notin \mathcal{P}_n &\Rightarrow V_n^\phi = 0 \\
\phi \notin \mathcal{P}_{mn} &\Rightarrow I_{mn}^\phi = 0 \\
\phi \notin \mathcal{P}_{mn} &\Rightarrow Z_{mn}^{\phi\psi} = Z_{mn}^{\psi\phi} = 0 \quad \forall \psi \in \{a, b, c\} \\
\phi \notin \mathcal{P}_{mn} &\Rightarrow Y_{mn}^{\phi\psi} = Y_{mn}^{\psi\phi} = 0 \quad \forall \psi \in \{a, b, c\} .
\end{aligned} \tag{8.1}$$

The current/voltage relationship for a three phase line (m, n) between adjacent nodes m and n is captured by Kirchoff's Voltage Laws (KVL) in its full (8.2), and compact form (8.3):

$$\begin{bmatrix} V_m^a \\ V_m^b \\ V_m^c \end{bmatrix} = \begin{bmatrix} V_n^a \\ V_n^b \\ V_n^c \end{bmatrix} + \begin{bmatrix} Z_{mn}^{aa} & Z_{mn}^{ab} & Z_{mn}^{ac} \\ Z_{mn}^{ba} & Z_{mn}^{bb} & Z_{mn}^{bc} \\ Z_{mn}^{ca} & Z_{mn}^{cb} & Z_{mn}^{cc} \end{bmatrix} \begin{bmatrix} I_{mn}^a \\ I_{mn}^b \\ I_{mn}^c \end{bmatrix} \tag{8.2}$$

$$\mathbf{V}_m = \mathbf{V}_n + \mathbf{Z}_{mn} \mathbf{I}_{mn} , \tag{8.3}$$

where, $Z_{mn}^{\phi\psi} = r_{mn}^{\phi\psi} + jx_{mn}^{\phi\psi}$ denotes the complex impedance of line (m, n) across phases ϕ and ψ . Here, (8.2) and (8.3) are presented where $\mathcal{P}_{mn} = \{a, b, c\}$. For lines with less than three phases ($|\mathcal{P}_{mn}| = 1$, or $|\mathcal{P}_{mn}| = 2$) (8.3) becomes:

$$[\mathbf{V}_m]_{\mathcal{P}_{mn}} = [\mathbf{V}_n]_{\mathcal{P}_{mn}} + [\mathbf{Z}_{mn}]_{\mathcal{P}_{mn}, \mathcal{P}_{mn}} [\mathbf{I}_{mn}]_{\mathcal{P}_{mn}} , \tag{8.4}$$

by employing the same indexing notation as in [11]. In this notation, rows of all terms in (8.4), and columns of \mathbf{Z}_{mn} , corresponding to $\phi \notin \mathcal{P}_{mn}$ are removed. For example, for a single phase line (m, n) where $\mathcal{P}_{mn} = \{\phi\}$, (8.4) is stated as:

$$V_m^\phi = V_n^\phi + Z_{mn}^{\phi\phi} I_{mn}^\phi .$$

For a two phase line (m, n) where $\mathcal{P}_{mn} = \{a, b\}$, (8.4) is stated as:

$$\begin{bmatrix} V_m^a \\ V_m^b \end{bmatrix} = \begin{bmatrix} V_n^a \\ V_n^b \end{bmatrix} + \begin{bmatrix} Z_{mn}^{aa} & Z_{mn}^{ab} \\ Z_{mn}^{ba} & Z_{mn}^{bb} \end{bmatrix} \begin{bmatrix} I_{mn}^a \\ I_{mn}^b \end{bmatrix} .$$

For a two phase line (m, n) where $\mathcal{P}_{mn} = \{a, c\}$, (8.4) is stated as:

$$\begin{bmatrix} V_m^a \\ V_m^c \end{bmatrix} = \begin{bmatrix} V_n^a \\ V_n^c \end{bmatrix} + \begin{bmatrix} Z_{mn}^{aa} & Z_{mn}^{ac} \\ Z_{mn}^{ca} & Z_{mn}^{cc} \end{bmatrix} \begin{bmatrix} I_{mn}^a \\ I_{mn}^c \end{bmatrix} .$$

Kirchoff's Current law at node m is given in its full (8.5) and compact (8.6) forms:

$$\sum_{l:(l,m) \in \mathcal{E}} \begin{bmatrix} I_{lm}^a \\ I_{lm}^b \\ I_{lm}^c \end{bmatrix} = \begin{bmatrix} i_m^a \\ i_m^b \\ i_m^c \end{bmatrix} + \sum_{n:(m,n) \in \mathcal{E}} \begin{bmatrix} I_{mn}^a \\ I_{mn}^b \\ I_{mn}^c \end{bmatrix} \tag{8.5}$$

$$\sum_{l:(l,m) \in \mathcal{E}} \mathbf{I}_{lm} = \mathbf{i}_m + \sum_{n:(m,n) \in \mathcal{E}} \mathbf{I}_{mn} . \tag{8.6}$$

Figure 8.1 shows a simple network with node voltage, node current, line current, and line impedance.

Complex power on a line is defined at either end of the line as:

$$\begin{aligned} S_{mn,m}^\phi &= V_m^\phi (I_{mn}^\phi)^* \\ S_{mn,n}^\phi &= V_n^\phi (I_{mn}^\phi)^* \end{aligned} \quad , \quad (8.7)$$

where $S_{mn,m}^\phi = P_{mn,m}^\phi + jQ_{mn,m}^\phi \in \mathbb{C}$ is the power from node m to node n at node m , and $S_{mn,n}^\phi = P_{mn,n}^\phi + jQ_{mn,n}^\phi \in \mathbb{C}$ is the power from node m to node n at node n . The vector of complex power flow on line (m, n) at node m is $\mathbf{S}_{mn,m} = [S_{mn,m}^a \ S_{mn,m}^b \ S_{mn,m}^c]^T$ for node m where $\mathbf{S}_{mn,m} = \mathbf{P}_{mn,m} + j\mathbf{Q}_{mn,m}$. The vector of complex power flow on line (m, n) at node n is $\mathbf{S}_{mn,n} = [S_{mn,n}^a \ S_{mn,n}^b \ S_{mn,n}^c]^T$ where $\mathbf{S}_{mn,n} = \mathbf{P}_{mn,n} + j\mathbf{Q}_{mn,n}$. A complex load is served at each node, where the voltage dependent load on a phase $s_n^\phi(V_n^\phi) = p_n^\phi(V_n^\phi) + jq_n^\phi(V_n^\phi) \in \mathbb{C}$ is:

$$s_n^\phi(V_n^\phi) = \left(A_{PQ,n}^\phi + A_{I,n}^\phi |V_n^\phi| + A_{Z,n}^\phi |V_n^\phi|^2 \right) d_n^\phi + w_n^\phi - jc_n^\phi = V_n^\phi (i_n^\phi)^* \quad , \quad (8.8)$$

where c_n^ϕ denotes capacitance, and $A_{PQ,n}^\phi$, $A_{I,n}^\phi$, and $A_{Z,n}^\phi$ are demand ZIP model [38] parameters such that $A_{PQ,n}^\phi + A_{I,n}^\phi + A_{Z,n}^\phi = 1 \ \forall \phi \in \mathcal{P}_n \ \forall n \in \mathcal{N}$. The vector of complex loads at node n is $\mathbf{s}_n = [s_n^a \ s_n^b \ s_n^c]^T$ where $\mathbf{s}_n = \mathbf{p}_n + j\mathbf{q}_n$. Figure 8.2 shows power flow and node loads on a simple network.

In 8.8, the complex DER dispatch is:

$$w_n^\phi = u_n^\phi + jv_n^\phi \quad , \quad (8.9)$$

where the vector of complex DER dispatch at node n is $\mathbf{w}_n = [w_n^a \ w_n^b \ w_n^c]^T$ where $\mathbf{w}_n = \mathbf{u}_n + j\mathbf{v}_n$.

Throughout this work, we use the symbol \circ to represent the Hadamard Product (HP) of two matrices (or vectors) of the same dimension, also known of the element-wise product, defined as:

$$C = A \circ B = B \circ A \Rightarrow C_{ij} = A_{ij}B_{ij} = B_{ij}A_{ij} \quad ,$$

where i indicates the row and j indicates the column of the vector or matrix.

Chapter 9

A Discussion of Semidefinite Programming for Optimal Power Flow Problems

9.1 Introduction

Power flow models are often nonlinear (very often quadratic) and nonconvex, due to the nonlinear relations between voltage, current, and complex power. To give an example of the nonlinear nature of power flow models, consider line $(m, n) \in \mathcal{E}$, where the complex power at node m is $S_{mn,m} = V_m I_{mn}^*$. A model incorporating line power flows, node voltage and line current would therefore have quadratic equality constraints. Substituting the variable for current, by using the line voltage difference divided by line admittance, $I_{mn} = Y_{mn} (V_m - V_n)$, the power flow on the line at node m is $S_{mn,m} = V_m Y_{mn}^* (V_m^* - V_n^*) = Y_{mn}^* (V_m V_m^* - V_m V_n^*)$. However, this model is now quadratic in voltage, and contains quadratic inequality constraints. While this nonlinear equation can be linearized by variable substitution, it may be difficult to regain the original variables. Furthermore, nonlinear constraints, especially nonlinear equality constraints, often cause problems numerical solver convergence.

Semidefinite programming (SDP) is a useful method for transforming and approximating optimization programs with nonlinear or nonconvex objectives or constraints [28]. This is especially true for quadratic constraint quadratic programs (QCQP), which many OPF problems are (as seen in the above example). SDP for OPF applications has been studied extensively in recent history, with much literature addressing single phase networks, some earlier works include [7, 22]. More recent literature addresses multiphase networks [11, 50]. In this work, we will use SDP as a shorthand for both semidefinite programming and semidefinite program.

An SDP is an optimization program with a positive semidefinite matrix variable, which will be denoted as \mathbf{X} . Linear operators, such as the trace, $\text{Tr}(\cdot)$, are often used to incorporate inequality or equality constraints and craft objective functions [28]. Constraints that are

quadratic in \mathbf{X} can be incorporated with linear matrix inequalities. The matrix variable \mathbf{X} , is often formed from a vector \mathbf{x} right multiplied by its complex conjugate transpose, such that $\mathbf{X} = \mathbf{x}\mathbf{x}^H$. To recover the vector \mathbf{x} from the matrix \mathbf{X} , the solution to the SDP, X , must have a rank of one. However, the condition that \mathbf{X} is rank-one is not convex [28]. Therefore this constraint is often removed from the SDP to obtain a semidefinite relaxation (SDR), a convex relaxation of the original SDP. The SDR is better suited for solver utilizing interior point methods. While a solver may not return a matrix that is strictly rank-one, if the ratio of the largest nonzero eigenvalue to the second largest nonzero eigenvalue is large enough, the matrix may be considered to be rank-one.

We now provide a summary of select literature on OPF SDPs for single and multiphase networks. We will discuss the successes of SDPs, and also drawbacks that may preclude them from being practically applicable.

9.2 Previous Research in SDP for OPFs

Literature on semidefinite programming has mainly focused on single phase networks, and the results show the potential of SDP and SDR as a viable method for solving nonlinear and nonconvex OPF problems. One of the earliest works utilizing SDP for OPF applications is [7], in which the authors derive an OPF SDP, and solve the SDP using interior point methods. In [22], the authors investigate conditions under which the SDP and SDR primal and dual problems will converge to the same solution, and under which a rank-one solution is obtainable. The authors of [23] discuss geometric interpretations of power flow physics, and show that the optimal Pareto-optimal points do not change under convex relaxations. The authors also discuss line power bounds and angle constraints.

The authors of [24] investigate limitations of semidefinite programming in solving OPF problems. They propose modifications to the SDP to replicate OPF solutions for five node and seven node networks. They authors found that their approach in modifying constraints was unsuccessful, and found varying levels of success modifying the SDP objective.

The authors present simulations on simple networks that show convergence to rank-one solutions with both binding non binding line flow constraints, with results verified by a separate solver. However, when line flow the constraint bounds are tightened, a rank-one solution is unobtainable, though the new problem is feasible.

The authors of [27] study sufficiency conditions for the exactness of SDP convex relaxations; the conditions under which a rank-one solution is obtainable. The authors propose a lemma (Lemma 1 in [27]) that states that a nondegenerate feasible solution to a SDP will have rank greater than 1 if the number of equality constraints plus binding inequality constraints to the SDP is greater than or equal to twice problem dimension.

The authors propose a theorem (Theorem 2 in [27]) stating that if a primal nondegenerate solution in the optimal solution set of the primal SDP problem has equality constraints and binding inequality constraints in number greater than twice the problem dimensionality, then there are no rank-one solutions in the optimal solution set. This theorem places strict

bounds on the number of equality constraints that a SDP can have in order to possibly yield a rank-one optimal solution, which is less than twice the problem dimensionality. The authors provide remarks on SDP formulation and common constraints on voltage and generation (DER dispatch).

The authors perform numerical studies on several test cases. Using test cases from literature, the authors show that while all the test cases follow the sufficient condition outlined in [27], a unique rank-one solution could not be found.

The authors then empirically investigate the effect on a network's load profile has on obtaining an exact relaxation. They found that in gridding several loads on a network, roughly 93.7% of cases had a unique optimal solution, however only 6.3% of all cases yielded a unique rank-one solution, so that for a vast majority of cases the relaxation is inexact.

In [29], the authors investigate implementation of an SDP OPF formulation for both radial (acyclic) and mesh (cyclic) networks. The authors explore different formulations and line capacity constraints and their relation to obtaining an exact SDP relaxation.

The authors discuss four types of common line capacity constraints and equivalent forms for an SDP, showing that the four line constraints have similar nonconvex feasible regions. Simulations on a simple three bus mesh network show that only one of the constraints yield a rank-1 solution for all values of maximum line voltage angle difference, while the other three only do so for certain values. The authors conclude from this example that problem formulation and constraint type are important to factors in successfully obtaining an exact relaxation. The authors prove that for a mesh (cyclic) network of size 3, an exact relaxation can be obtained if the minimum reactive DER dispatch is unbounded for a lossless case, and if the real and reactive DER dispatch is unbounded for a lossy case.

The authors then propose adding a penalty function to the OPF objective, penalizing DER reactive power dispatch, in order to obtain a low-rank or rank-1 solution. The authors define a degree of sub-optimality for this modified OPF, and discuss how the modified OPF SDP solution can be used to find the global optimal solution to the original OPF.

Simulation results on mesh (cyclic) test networks show that the original OPF is unable to obtain rank-1 solutions, however the modified OPF yields rank-1 solutions with appropriate weighting on the additional reactive power dispatch penalty. Simulations results also show that the weight on the additional penalty does not significantly impact DER real power dispatch compared to the original OPF, but does significantly alter the DER reactive power dispatch.

In [31] and [32], the authors investigate physical network conditions that will lead to an SDP producing a globally optimal solution. The authors investigate two networks which can be equivalently modeled, showing that the SDR converges for one and not the other.

From these examples, it can be surmised that SDP has drawbacks that may preclude it from being widely applicable to many different networks,

Recently, the literature on SDP OPF formulations has expanded to study multiphase networks. In [11], the authors derive an unbalanced multi-phase power flow model for radial networks, and transform the problem into an equivalent semi-definite program (SDP) formulation. The authors discuss a convex relaxation to the equivalent SDP that such that

the relaxed equivalent SDP is convex. The authors derive a distributed solution such that the SDP can be implemented within subnetworks on a radial network. They leverage an algorithm using alternating direction method of multipliers (ADMM) to solve several local SDP problems accounting for a global objective and constraints.

The authors successfully transform a nonlinear optimization problem into an equivalent SDP. They furthermore apply a rank relaxation to the equivalent SDP such that the relaxed problem is convex. The authors show that if the relaxed SDP has a solution with rank 1, then the solution is optimal for both the relaxed problem and the equivalent SDP.

The authors provide an intuitive argument that builds upon that of [23, 51], as to why the multiphase SDP should converge to a rank-one solution for a radial (acyclic) network. While the authors present simulations that show the success of their method, for certain cases a rank-one solution was not obtainable unless the substation voltage was changed from 1 to 1.02 p.u.

The authors of [50] build upon the work in [11] by developing an algorithm to solve an OPF should the convex relaxation of the SDP fail.

Literature on SDP OPFs has shown great success in utilizing SDP to solve nonlinear OPFs. However the literature also outlines several properties of SDP that may preclude it from being practically implementable.

9.3 Extensions of the SDP OPF for Control of Voltage Phasors

Many of the OPFs discussed in recent literature papers are economic dispatch problems. In this section, we will derive objective functions and constraints and objective functions for control of voltage phasors for the purposes of grid reconfiguration. The work in this section is not intended as a definitive study on SDP OPFs for controlling voltage magnitude and phase angle. Instead, it is a preliminary foray into the method for comparative purposes.

Summary of Nomenclature and SDP/SDR Derivation

In this section, we outline pertinent nomenclature and derive relations that can be incorporated into an SDP OPF. The nomenclature and derivation are based on that in [11], with some modifications.

All node voltage phasor vectors \mathbf{V}_m , $m \in \mathcal{N}$ are collected into the vector $\mathbf{v} \in \mathbb{C}^{3(N+1)}$:

$$\mathbf{v} = \left[\mathbf{V}_0^T \quad \mathbf{V}_1^T \quad \dots \quad \mathbf{V}_N^T \right]^T, \quad (9.1)$$

and all node current phasor vectors \mathbf{i}_m , $(m) \in \mathcal{N}$ are collected into the vector $\mathbf{i} \in \mathbb{C}^{3(N+1)}$:

$$\mathbf{i} = \left[\mathbf{i}_0^T \quad \mathbf{i}_1^T \quad \dots \quad \mathbf{i}_N^T \right]^T. \quad (9.2)$$

The vectors \mathbf{i} and \mathbf{v} are related by the symmetric admittance matrix $\mathbf{Y} \in \mathbb{C}^{3(N+1) \times 3(N+1)}$ such that:

$$\mathbf{i} = \mathbf{Y}\mathbf{v} , \quad (9.3)$$

with \mathbf{Y} as defined in [11]. The voltage (current) on phase ϕ at node n can be obtained by multiplying the voltage (current) vector by the transpose of vector \bar{e}_n^ϕ , as defined in [11]:

$$\begin{aligned} V_n^\phi &= (\bar{e}_n^\phi)^T \mathbf{v} \\ i_n^\phi &= (\bar{e}_n^\phi)^T \mathbf{i} = (\bar{e}_n^\phi)^T \mathbf{Y}\mathbf{v} . \end{aligned} \quad (9.4)$$

The hermitian matrix $\mathbf{V} \in \mathbb{C}^{3(N+1) \times 3(N+1)}$ is defined as:

$$\mathbf{V} = \mathbf{v}\mathbf{v}^H . \quad (9.5)$$

The squared magnitude of the voltage phasor V_n^ϕ is:

$$\begin{aligned} |V_n^\phi|^2 &= (V_n^\phi)^* V_n^\phi = \mathbf{v}^H \bar{e}_n^\phi (\bar{e}_n^\phi)^T \mathbf{v} = \mathbf{v}^H \Phi_{V,n}^\phi \mathbf{v} \dots \\ &= \text{Tr} \left(\mathbf{v}^H \Phi_{V,n}^\phi \mathbf{v} \right) = \text{Tr} \left(\Phi_{V,n}^\phi \mathbf{v}\mathbf{v}^H \right) = \text{Tr} \left(\Phi_{V,n}^\phi \mathbf{V} \right) , \end{aligned} \quad (9.6)$$

where $\Phi_{V,n}^\phi = \bar{e}_n^\phi (\bar{e}_n^\phi)^T \in \mathbb{R}^{3(N+1) \times 3(N+1)}$. Minimum and maximum voltage magnitude constraints are incorporated into the OPF as:

$$\underline{V}_n^\phi \leq |V_n^\phi| \leq \bar{V}_n^\phi \Rightarrow (\underline{V}_n^\phi)^2 \leq \text{Tr} \left(\Phi_{V,n}^\phi \mathbf{V} \right) \leq (\bar{V}_n^\phi)^2 . \quad (9.7)$$

The complex load on phase ϕ at node n is defined by (8.8), and can be expressed as:

$$\begin{aligned} s_n^\phi &= V_n^\phi (i_n^\phi)^* = (i_n^\phi)^* V_n^\phi = \mathbf{i}^H \bar{e}_n^\phi (\bar{e}_n^\phi)^T \mathbf{v} = \mathbf{v}^H \mathbf{Y}^H \bar{e}_n^\phi (\bar{e}_n^\phi)^T \mathbf{v} = \mathbf{v}^H \mathbf{Y}_n^\phi \mathbf{v} \dots \\ &= \text{Tr} \left(\mathbf{v}^H \mathbf{Y}_n^\phi \mathbf{v} \right) = \text{Tr} \left(\mathbf{Y}_n^\phi \mathbf{v}\mathbf{v}^H \right) = \text{Tr} \left(\mathbf{Y}_n^\phi \mathbf{V} \right) , \end{aligned} \quad (9.8)$$

where $\mathbf{Y}_n^\phi = \mathbf{Y}^H \bar{e}_n^\phi (\bar{e}_n^\phi)^T \in \mathbb{C}^{3(N+1) \times 3(N+1)}$. The active (real) and reactive (imaginary) parts of the complex load are:

$$\begin{aligned} p_n^\phi &= \frac{1}{2} \left(\mathbf{v}^H \mathbf{Y}_n^\phi \mathbf{v} + \mathbf{v}^H (\mathbf{Y}_n^\phi)^H \mathbf{v} \right) = \frac{1}{2} \text{Tr} \left(\left(\mathbf{Y}_n^\phi + (\mathbf{Y}_n^\phi)^H \right) \mathbf{V} \right) = \text{Tr} \left(\Phi_{p,n}^\phi \mathbf{V} \right) \\ q_n^\phi &= \frac{1}{j2} \left(\mathbf{v}^H \mathbf{Y}_n^\phi \mathbf{v} - \mathbf{v}^H (\mathbf{Y}_n^\phi)^H \mathbf{v} \right) = \frac{1}{j2} \text{Tr} \left(\left(\mathbf{Y}_n^\phi - (\mathbf{Y}_n^\phi)^H \right) \mathbf{V} \right) = \text{Tr} \left(\Phi_{q,n}^\phi \mathbf{V} \right) , \end{aligned} \quad (9.9)$$

where $\Phi_{p,n}^\phi = \frac{1}{2} \left(\mathbf{Y}_n^\phi + (\mathbf{Y}_n^\phi)^H \right)$ and $\Phi_{q,n}^\phi = \frac{1}{j2} \left(\mathbf{Y}_n^\phi - (\mathbf{Y}_n^\phi)^H \right)$.

From (8.8), the DER real and reactive power dispatch on phase ϕ at node n , u_n^ϕ and v_n^ϕ , respectively, are:

$$\begin{aligned} u_n^\phi &= p_n^\phi - \left(A_{PQ,n}^\phi + A_{Z,n}^\phi |V_n^\phi|^2 \right) \text{Re} \{ d_n^\phi \} \\ &= \text{Tr} \left(\Phi_{p,n}^\phi \mathbf{V} \right) - \left(A_{PQ,n}^\phi + A_{Z,n}^\phi \text{Tr} \left(\Phi_{V,n}^\phi \mathbf{V} \right) \right) \text{Re} \{ d_n^\phi \} \\ v_n^\phi &= q_n^\phi - \left(A_{PQ,n}^\phi + A_{Z,n}^\phi |V_n^\phi|^2 \right) \text{Im} \{ d_n^\phi \} + c_n^\phi \\ &= \text{Tr} \left(\Phi_{q,n}^\phi \mathbf{V} \right) - \left(A_{PQ,n}^\phi + A_{Z,n}^\phi \text{Tr} \left(\Phi_{V,n}^\phi \mathbf{V} \right) \right) \text{Im} \{ d_n^\phi \} + c_n^\phi . \end{aligned} \quad (9.10)$$

With this definition, we can define bounds on the DER complex power dispatch. The first is to limit the real and reactive power independently, as in [11]:

$$\begin{aligned} \underline{u}_n^\phi &\leq u_n^\phi \leq \bar{u}_n^\phi \\ \underline{v}_n^\phi &\leq v_n^\phi \leq \bar{v}_n^\phi . \end{aligned} \tag{9.11}$$

The second bound on DER complex power dispatch is an approximation on apparent power constraint with N_c half-spaces, as derived in Appendix C:

$$\cos(\delta_k)u_n^\phi + \sin(\delta_k)v_n^\phi \leq \bar{w}_n^\phi, \quad \frac{k2\pi}{N_c}, \quad k = 0, 1 \dots N_c . \tag{9.12}$$

The third bound on DER complex dispatch is a bound on apparent power of the form, as in [33]:

$$|u_n^\phi + jv_n^\phi| \leq \bar{w}_n^\phi \equiv \begin{bmatrix} (\bar{w}_n^\phi)^2 & u_n^\phi & v_n^\phi \\ u_n^\phi & -1 & 0 \\ v_n^\phi & 0 & -1 \end{bmatrix} \preceq 0 , \tag{9.13}$$

where \succeq (\preceq) denotes the LHS matrix is positive (negative) semidefinite.

The authors of [29], propose modifying the objective function of an SDP by penalizing the reactive power sourced (output by DER into the grid). The penalty is takes the form:

$$\begin{aligned} g(\mathbf{V}) &= - \sum_{\substack{n \in \mathcal{G} \\ \phi \in \mathcal{P}_n}} v_n^\phi = - \sum_{\substack{n \in \mathcal{G} \\ \phi \in \mathcal{P}_n}} q_n^\phi - \left(A_{PQ,n}^\phi + A_{Z,n}^\phi |V_n^\phi|^2 \right) \mathbf{Im} \{ d_n^\phi \} + c_n^\phi \\ &= - \sum_{\substack{n \in \mathcal{G} \\ \phi \in \mathcal{P}_n}} \text{Tr} \left(\Phi_{q,n}^\phi \mathbf{V} \right) - \left(A_{PQ,n}^\phi + A_{Z,n}^\phi \text{Tr} \left(\Phi_{V,n}^\phi \mathbf{V} \right) \right) \mathbf{Im} \{ d_n^\phi \} + c_n^\phi . \end{aligned} \tag{9.14}$$

Simulation Parameters

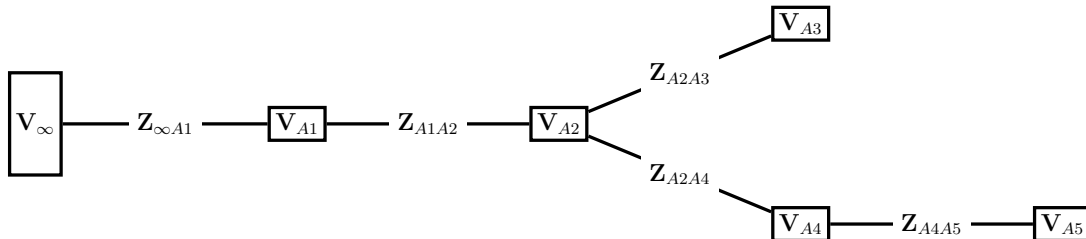


Figure 9.1: Diagram of simple network used in SDP OPF Simulations.

In this section we discuss a simple network that we perform simulations with SDP OPFs on. For simplicity, the network is single phase. DER is placed at nodes $\mathcal{G} = \{A2, A3, A5\}$

with an apparent capacity limit of 0.05 p.u. DER is assumed to be inverters capable of four quadrant operation, and thus can source and sink real and reactive power independently.

The voltage obtained from solving power flow with no DER dispatch, $u_n = v_n = 0$ with a Newton-Raphson method [48] is given in Table 9.1.

Node	V_n [p.u.]	V_n [p.u.]
∞	$1.0000 - j0.0000$	$1.0000 \angle 0.0000^\circ$
A1	$0.9943 - j0.0033$	$0.9943 \angle -0.1873^\circ$
A2	$0.9714 - j0.0163$	$0.9715 \angle -0.9587^\circ$
A3	$0.9654 - j0.0191$	$0.9656 \angle -1.1317^\circ$
A4	$0.9654 - j0.0201$	$0.9656 \angle -1.1903^\circ$
A5	$0.9638 - j0.0225$	$0.9641 \angle -1.3370^\circ$

Table 9.1: Voltage from solving power flow [48] with zero DER dispatch.

In the next section, we derive and discuss simulation results of several SDP formulations for controlling voltage magnitude and angle on a network. As in [29], we penalize DER reactive power dispatch with (9.14), and a weight of ε .

We consider the solution \mathbf{V} to be rank-one if it only has one positive nonzero eigenvalue, or if $|\lambda_1/\lambda_2| \geq 10^6$, where λ_1 and λ_2 are the first and second largest nonzero eigenvalues of \mathbf{V} , respectively. The eigenvalue decomposition of \mathbf{V} is $\mathbf{V} = \mathbf{U}\mathbf{\Lambda}\mathbf{U}^H = \mathbf{v}\mathbf{v}^H$, and thus $\mathbf{v} = \sum_k \sqrt{\lambda_k} \mathbf{u}_k$ where λ_k and \mathbf{u}_k are the eigenvalues and eigenvectors of \mathbf{V} , respectively. Thus if $\mathcal{O}(|\lambda_1/\lambda_2|) \sim 10^6$ then $\mathcal{O}(\sqrt{|\lambda_1/\lambda_2|}) \sim 10^3$.

Extension of SDP Method for Control of Voltage Magnitude

Voltage Magnitude Reference Tracking

We first consider a tracking problem in which an SDP seeks to minimize the absolute difference between the voltage magnitude at a node, and a reference. For a multiphase network, this is written as (9.15), where the voltage magnitude reference for phase ϕ at node k is ν_k^ϕ :

$$\begin{aligned}
 & \underset{\mathbf{V}}{\text{minimize}} && \sum_{\phi \in \mathcal{P}_k} \left| \text{Tr} \left(\Phi_{V,k}^\phi \mathbf{V} \right) - \left(\nu_k^\phi \right)^2 \right| + \varepsilon g(\mathbf{V}) \\
 & \text{subject to} && (9.10), (9.13), (9.14) \quad \forall \phi \in \mathcal{P}_n, \forall n \in \mathcal{G} \\
 & && 0.95 \leq |V_n^\phi| \leq 1.05, (9.7) \quad \forall \phi \in \mathcal{P}_n, \forall n \in \mathcal{N} \\
 & && \mathbf{V}_1 = \begin{bmatrix} 1 & 1 \angle -120^\circ & 1 \angle 120^\circ \end{bmatrix}^T .
 \end{aligned} \tag{9.15}$$

The objective function can be transformed into a linear objective function and two linear constraints by introducing a new variable $\gamma_{V,k}^\phi$ such that:

$$\begin{aligned}
 & \underset{\mathbf{V}, \gamma_k^\phi}{\text{minimize}} && \sum_{\phi \in \mathcal{P}_k} \gamma_k^\phi + \varepsilon g(\mathbf{V}) \\
 & \text{subject to} && (9.10), (9.13), (9.14) \quad \forall \phi \in \mathcal{P}_n, \forall n \in \mathcal{G} \\
 & && 0.95 \leq |V_n^\phi| \leq 1.05, (9.7) \quad \forall \phi \in \mathcal{P}_n, \forall n \in \mathcal{N} \\
 & && \mathbf{V}_1 = \begin{bmatrix} 1 & 1\angle -120^\circ & 1\angle 120^\circ \end{bmatrix}^T \\
 & && \text{Tr} \left(\Phi_{V,k}^\phi \mathbf{V} \right) - \left(\nu_k^\phi \right)^2 \leq \gamma_{V,k}^\phi \quad \forall \phi \in \mathcal{P}_k \\
 & && - \text{Tr} \left(\Phi_{V,k}^\phi \mathbf{V} \right) + \left(\nu_k^\phi \right)^2 \leq \gamma_{V,k}^\phi \quad \forall \phi \in \mathcal{P}_k .
 \end{aligned} \tag{9.16}$$

The OPF can also be cast as a quadratic minimization, as in (9.17):

$$\begin{aligned}
 & \underset{\mathbf{V}}{\text{minimize}} && \sum_{\phi \in \mathcal{P}_k} \left(\text{Tr} \left(\Phi_{V,k}^\phi \mathbf{V} \right) - \left(\nu_k^\phi \right)^2 \right)^2 + \varepsilon g(\mathbf{V}) \\
 & \text{subject to} && (9.10), (9.13), (9.14) \quad \forall \phi \in \mathcal{P}_n, \forall n \in \mathcal{G} \\
 & && 0.95 \leq |V_n^\phi| \leq 1.05, (9.7) \quad \forall \phi \in \mathcal{P}_n, \forall n \in \mathcal{N} \\
 & && \mathbf{V}_1 = \begin{bmatrix} 1 & 1\angle -120^\circ & 1\angle 120^\circ \end{bmatrix}^T ,
 \end{aligned} \tag{9.17}$$

and transformed by introducing the variable γ_k^ϕ and a semidefinite matrix, as in [32]:

$$\begin{aligned}
 & \underset{\mathbf{V}, \gamma_k^\phi}{\text{minimize}} && \sum_{\phi \in \mathcal{P}_k} \gamma_k^\phi + \varepsilon g(\mathbf{V}) \\
 & \text{subject to} && (9.10), (9.13), (9.14) \quad \forall \phi \in \mathcal{P}_n, \forall n \in \mathcal{G} \\
 & && 0.95 \leq |V_n^\phi| \leq 1.05, (9.7) \quad \forall \phi \in \mathcal{P}_n, \forall n \in \mathcal{N} \\
 & && \mathbf{V}_1 = \begin{bmatrix} 1 & 1\angle -120^\circ & 1\angle 120^\circ \end{bmatrix}^T \\
 & && \begin{bmatrix} \gamma_k^\phi & \left(\text{Tr} \left(\Phi_{V,k}^\phi \mathbf{V} \right) - \left(\nu_k^\phi \right)^2 \right) \\ \left(\text{Tr} \left(\Phi_{V,k}^\phi \mathbf{V} \right) - \left(\nu_k^\phi \right)^2 \right) & 1 \end{bmatrix} \succeq 0 \quad \forall \phi \in \mathcal{P}_k .
 \end{aligned} \tag{9.18}$$

Simulations were run on the network shown in Figure 9.1, with the OPF of (9.16), with the node $k = A2$ given a reference. We perform simulations for voltage magnitude references varying from 0.95 to 1.0 in increments of 0.005 p.u. Additionally, the DER reactive power dispatch is penalized as in [29] with ε varying from 0 to 0.5 in increments of 0.05.

Figure 9.2 gives the results a simulation of (9.16) with varying voltage magnitude reference and reactive power dispatch penalty. It can be seen that for a voltage magnitude

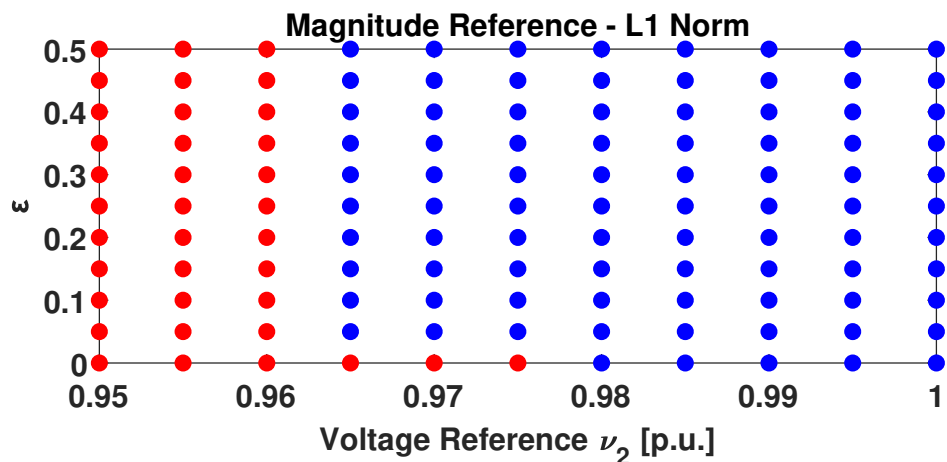


Figure 9.2: Results of OPF (9.16) simulations with varying voltage magnitude reference and reactive power dispatch penalty. Blue dots represent cases with rank-one solutions. Red dots represent cases where a rank-one solution was not obtained.

reference of $\nu_{A2} \geq 0.98$ p.u., the unmodified OPF converges to a rank-one solution. For magnitude references of $0.965 \leq \nu_{A2} \leq 0.975$ p.u., the original OPF did not reach a rank-one solution, and a small penalty on DER reactive power dispatch led to a rank-one solution. For magnitude references of $0.95 \leq \nu_{A2} \leq 0.96$, no penalty weighting led a rank-one solution. The ratio of eigenvalues for these cases was always less than 10^4 .

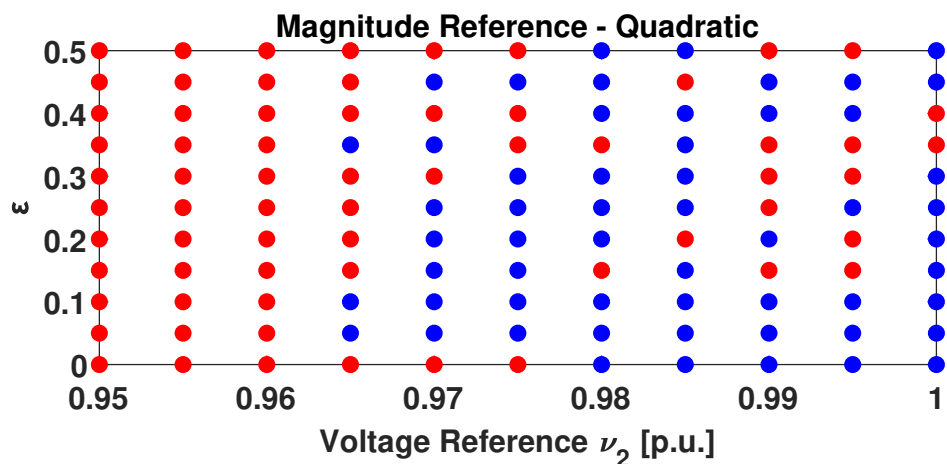


Figure 9.3: Results of OPF (9.16) simulations with varying voltage magnitude reference and reactive power dispatch penalty. Blue dots represent cases with rank-one solutions. Red dots represent cases where a rank-one solution was not obtained.

Figure 9.3 gives the results a simulation of (9.18) with varying voltage magnitude reference and reactive power dispatch penalty. This case has similar results to the previous simulation. Higher voltage magnitude references cases did not require modification of the OPF

objective function. Cases where the voltage magnitude references was $0.965 \leq \nu_{A2} \leq 0.975$ p.u., required a small penalty to obtain a rank-one solution. Finally, the cases where $0.95 \leq \nu_{A2} \leq 0.96$ did not converge to a rank-one solution despite with any weighting on DER reactive power dispatch.

Minimization of Voltage Magnitude Difference

The previous OPFs can be extended to minimize the difference between voltage magnitude across different phases at a node, between the same phase at different nodes, or between different phases at different nodes:

$$E_{kl}^\phi = \left| V_k^\phi \right|^2 - \left| V_l^\phi \right|^2 = \text{Tr} \left(\Phi_{V,k}^\phi \mathbf{V} \right) - \text{Tr} \left(\Phi_{V,l}^\phi \mathbf{V} \right) = \text{Tr} \left(\Phi_{V,kl}^\phi \mathbf{V} \right), \quad (9.19)$$

where $\Phi_{V,kl}^\phi = \Phi_{V,k}^\phi - \Phi_{V,l}^\phi$. An OPF minimizing the absolute value of the difference between voltage magnitude of phase ϕ at node k and node l is:

$$\begin{aligned} & \underset{\mathbf{V}}{\text{minimize}} && \sum_{\phi \in \mathcal{P}_{kl}} \left| \text{Tr} \left(\Phi_{V,kl}^\phi \mathbf{V} \right) \right| + \varepsilon g(\mathbf{V}) \\ & \text{subject to} && (9.10), (9.13), (9.14) \quad \forall \phi \in \mathcal{P}_n, \forall n \in \mathcal{G} \\ & && 0.95 \leq |V_n^\phi| \leq 1.05, (9.7) \quad \forall \phi \in \mathcal{P}_n, \forall n \in \mathcal{N} \\ & && \mathbf{V}_1 = \left[1 \quad 1\angle -120^\circ \quad 1\angle 120^\circ \right]^T. \end{aligned} \quad (9.20)$$

This objective can likewise be transformed into a linear objective function and two linear constraints as in:

$$\begin{aligned} & \underset{\mathbf{V}, \gamma_{kl}^\phi}{\text{minimize}} && \sum_{\phi \in \mathcal{P}_{kl}} \gamma_{kl}^\phi + \varepsilon g(\mathbf{V}) \\ & \text{subject to} && (9.10), (9.13), (9.14) \quad \forall \phi \in \mathcal{P}_n, \forall n \in \mathcal{G} \\ & && 0.95 \leq |V_n^\phi| \leq 1.05, (9.7) \quad \forall \phi \in \mathcal{P}_n, \forall n \in \mathcal{N} \\ & && \mathbf{V}_1 = \left[1 \quad 1\angle -120^\circ \quad 1\angle 120^\circ \right]^T \\ & && \text{Tr} \left(\Phi_{V,kl}^\phi \mathbf{V} \right) \leq \gamma_{V,kl}^\phi \quad \forall \phi \in \mathcal{P}_{kl} \\ & && - \text{Tr} \left(\Phi_{V,kl}^\phi \mathbf{V} \right) \leq \gamma_{V,kl}^\phi \quad \forall \phi \in \mathcal{P}_{kl}. \end{aligned} \quad (9.21)$$

The OPF minimizing voltage magnitude difference can also be cast a quadratic minimization

as in (9.22):

$$\begin{aligned}
 & \underset{\mathbf{V}}{\text{minimize}} && \sum_{\phi \in \mathcal{P}_{kl}} \left(\text{Tr} \left(\Phi_{V,kl}^{\phi} \mathbf{V} \right) \right)^2 + \varepsilon g(\mathbf{V}) \\
 & \text{subject to} && (9.10), (9.13), (9.14) \quad \forall \phi \in \mathcal{P}_n, \forall n \in \mathcal{G} \\
 & && 0.95 \leq |V_n^{\phi}| \leq 1.05, (9.7) \quad \forall \phi \in \mathcal{P}_n, \forall n \in \mathcal{N} \\
 & && \mathbf{V}_1 = \begin{bmatrix} 1 & 1\angle -120^\circ & 1\angle 120^\circ \end{bmatrix}^T .
 \end{aligned} \tag{9.22}$$

This can likewise be transformed into the SDR of (9.23):

$$\begin{aligned}
 & \underset{\mathbf{V}, \gamma_{kl}^{\phi}}{\text{minimize}} && \sum_{\phi \in \mathcal{P}_{kl}} \gamma_{kl}^{\phi} + \varepsilon g(\mathbf{V}) \\
 & \text{subject to} && (9.10), (9.13), (9.14) \quad \forall \phi \in \mathcal{P}_n, \forall n \in \mathcal{G} \\
 & && 0.95 \leq |V_n^{\phi}| \leq 1.05, (9.7) \quad \forall \phi \in \mathcal{P}_n, \forall n \in \mathcal{N} \\
 & && \mathbf{V}_1 = \begin{bmatrix} 1 & 1\angle -120^\circ & 1\angle 120^\circ \end{bmatrix}^T \\
 & && \begin{bmatrix} \gamma_{kl}^{\phi} & \text{Tr} \left(\Phi_{V,kl}^{\phi} \mathbf{V} \right) \\ \text{Tr} \left(\Phi_{V,kl}^{\phi} \mathbf{V} \right) & 1 \end{bmatrix} \succeq 0 \quad \forall \phi \in \mathcal{P}_{kl} .
 \end{aligned} \tag{9.23}$$

We performed simulations on the network shown in Figure 9.1, with $k = A3$ and $l = A5$. The penalty weighting on DER reactive power dispatch varied from 0 to 1 in increments of 0.1. With the OPF of (9.21), no rank-one solution was obtained. Similarly, with the OPF of (9.23), no rank-one solution was obtained. For all values of ε , $\mathcal{O}(|\lambda_1/\lambda_2|) \sim 10^3$ for all values of ε . The simulation results prompt further study of this problem.

Voltage Magnitude Difference Bounds

Bounds on the difference in voltage magnitude can be enforced using (9.19):

$$\begin{aligned}
 & \underset{\mathbf{V}, \gamma_{kl}^{\phi}}{\text{minimize}} && \sum_{\phi \in \mathcal{P}_{kl}} \varepsilon g(\mathbf{V}) \\
 & \text{subject to} && (9.10), (9.13), (9.14) \quad \forall \phi \in \mathcal{P}_n, \forall n \in \mathcal{G} \\
 & && 0.95 \leq |V_n^{\phi}| \leq 1.05, (9.7) \quad \forall \phi \in \mathcal{P}_n, \forall n \in \mathcal{N} \\
 & && \mathbf{V}_1 = \begin{bmatrix} 1 & 1\angle -120^\circ & 1\angle 120^\circ \end{bmatrix}^T \\
 & && \underline{E}_{kl}^{\phi} \leq \text{Tr} \left(\Phi_{V,kl}^{\phi} \mathbf{V} \right) \leq \overline{E}_{kl}^{\phi} \quad \forall \phi \in \mathcal{P}_{kl} .
 \end{aligned} \tag{9.24}$$

We performed simulations with $k = A3$ and $l = A5$. We performed multiple simulations with the penalty weighting on DER reactive power dispatch varied from 0 to 1 in increments of 0.1. For the no control case, the squared voltage magnitude of nodes $A3$ and $A5$ are

$|V_{A3}|^2 = 0.9323$ and $|V_{A5}|^2 = 0.9294$, respectively. With a magnitude difference bound of $-0.01 \leq E_{kl}^\phi \leq 0.01$ no rank one solution was found, and $\mathcal{O}(|\lambda_1/\lambda_2|) \sim 10^3$ for all values of ε . With a magnitude difference bound of $-0.005 \leq E_{kl}^\phi \leq 0.005$, no rank one solution was found, and $\mathcal{O}(|\lambda_1/\lambda_2|) \sim 10^3$ for all values of ε . With a magnitude difference bound of $-0.001 \leq E_{kl}^\phi \leq 0.001$, no rank one solution was found, and $\mathcal{O}(|\lambda_1/\lambda_2|) \sim 10^3$ for all values of ε . The simulation results prompt further study of this problem.

Extension of SDP Method for Control of Voltage Angle

Consider an off-diagonal index of \mathbf{V} corresponding to the product of the phasor of a phase ϕ at node m and the complex conjugate of the phasor for phase ϕ at node n , which can be expressed in polar form:

$$\begin{aligned} V_m^\phi (V_n^\phi)^* &= |V_m^\phi| |V_n^\phi| \angle (\theta_m^\pi - \theta_n^\pi) \\ &= |V_m^\phi| |V_n^\phi| [\cos(\theta_m^\pi - \theta_n^\pi) + j \sin(\theta_m^\pi - \theta_n^\pi)] . \end{aligned} \quad (9.25)$$

We now define $\theta_{mn}^\phi = \theta_m^\phi - \theta_n^\phi$. The ratio of the real and imaginary components of $V_m^\phi (V_n^\phi)^*$ is defined by the tangent function:

$$\frac{\mathbf{Im} \{V_m^\phi (V_n^\phi)^*\}}{\mathbf{Re} \{V_m^\phi (V_n^\phi)^*\}} = \frac{|V_m^\phi| |V_n^\phi| \sin(\theta_{mn}^\phi)}{|V_m^\phi| |V_n^\phi| \cos(\theta_{mn}^\phi)} = \tan(\theta_{mn}^\phi) . \quad (9.26)$$

The real and imaginary components of $V_m^\phi (V_n^\phi)^*$ are defined as:

$$\begin{aligned} \mathbf{Re} \{V_m^\phi (V_n^\phi)^*\} &= \frac{1}{2} [V_m^\phi (V_n^\phi)^* + (V_m^\phi)^* V_n^\phi] = \frac{1}{2} [\text{Tr}(\Phi_{mn}^\phi \mathbf{V}) + \text{Tr}(\Phi_{nm}^\phi \mathbf{V})] \\ \mathbf{Im} \{V_m^\phi (V_n^\phi)^*\} &= \frac{1}{j2} [V_m^\phi (V_n^\phi)^* - (V_m^\phi)^* V_n^\phi] = \frac{1}{j2} [\text{Tr}(\Phi_{mn}^\phi \mathbf{V}) - \text{Tr}(\Phi_{nm}^\phi \mathbf{V})] , \end{aligned} \quad (9.27)$$

where the matrices Φ_{mn}^ϕ and Φ_{nm}^ϕ are defined as:

$$\Phi_{mn}^\phi = \bar{e}_n^\phi (\bar{e}_m^\phi)^T, \quad \Phi_{nm}^\phi = \bar{e}_m^\phi (\bar{e}_n^\phi)^T, \quad (9.28)$$

using the same notation for \bar{e}_m^ϕ and \bar{e}_n^ϕ as in [11]. Thus, we can use (9.26), (9.27), and (9.28) to obtain relationships defining an off diagonal element of \mathbf{V} in terms of the its angle:

$$\begin{aligned} \mathbf{Re} \{V_m^\phi (V_n^\phi)^*\} \sin(\theta_{mn}^\phi) &= \mathbf{Im} \{V_m^\phi (V_n^\phi)^*\} \cos(\theta_{mn}^\phi) \\ \text{Tr}(\Phi_{Re,mn}^\phi \mathbf{V}) \sin(\theta_{mn}^\phi) &= \text{Tr}(\Phi_{Im,mn}^\phi \mathbf{V}) \cos(\theta_{mn}^\phi) \\ \Phi_{Re,mn} &= \frac{1}{2} [\Phi_{mn}^\phi + \Phi_{nm}^\phi], \quad \Phi_{Im,mn} = \frac{1}{j2} [\Phi_{mn}^\phi - \Phi_{nm}^\phi] . \end{aligned} \quad (9.29)$$

While 9.29 can be used to directly assign voltage angles, it is likely to not be practically applicable as choosing a feasible set of angles may prove difficult or impossible.

Voltage Angle Difference Bounds

On the interval $\langle -\pi/2, \pi/2 \rangle$, $a \leq b \Rightarrow \tan(a) \leq \tan(b)$, and thus we can take advantage of this property to introduce upper and lower bounds on voltage phasor angle using the previous analysis. Defining a lower angle bound as $\underline{\theta}_{mn}^\phi$, and an upper angle bound as $\bar{\theta}_{mn}^\phi$, we can introduce a new constraint:

$$\underline{\theta}_{mn}^\phi \leq \theta_{mn}^\phi \leq \bar{\theta}_{mn}^\phi \Rightarrow \tan(\underline{\theta}_{mn}^\phi) \leq \tan(\theta_{mn}^\phi) \leq \tan(\bar{\theta}_{mn}^\phi) , \quad (9.30)$$

where $\underline{\theta}_{mn}^\phi$, $\bar{\theta}_{mn}^\phi$ and θ_{mn}^ϕ are all on the interval $\langle -\pi, \pi \rangle$. With the definition of the real and imaginary parts of $V_m^\phi (V_n^\phi)^*$ from (9.26), this can be rewritten as:

$$\tan(\underline{\theta}_{mn}^\phi) \leq \frac{\mathbf{Im} \{ V_m^\phi (V_n^\phi)^* \}}{\mathbf{Re} \{ V_m^\phi (V_n^\phi)^* \}} \leq \tan(\bar{\theta}_{mn}^\phi) , \quad (9.31)$$

which can be rewritten by multiplying by the denominator:

$$\tan(\underline{\theta}_{mn}^\phi) \mathbf{Re} \{ V_m^\phi (V_n^\phi)^* \} \leq \mathbf{Im} \{ V_m^\phi (V_n^\phi)^* \} \leq \tan(\bar{\theta}_{mn}^\phi) \mathbf{Re} \{ V_m^\phi (V_n^\phi)^* \} . \quad (9.32)$$

Using the trace operator, this can be rewritten as a constraint for the voltage angle lower bound:

$$\tan(\underline{\theta}_{mn}^\phi) \text{Tr} \left(\Phi_{Re,mn}^\phi \mathbf{V} \right) \leq \text{Tr} \left(\Phi_{Im,mn}^\phi \mathbf{V} \right) , \quad (9.33)$$

and voltage angle upper bound:

$$\text{Tr} \left(\Phi_{Im,mn}^\phi \mathbf{V} \right) \leq \tan(\bar{\theta}_{mn}^\phi) \text{Tr} \left(\Phi_{Re,mn}^\phi \mathbf{V} \right) . \quad (9.34)$$

An example OPF that incorporates bounds on voltage angle difference is given by (9.35):

$$\begin{aligned} & \underset{\mathbf{V}}{\text{minimize}} && f(\mathbf{V}) + \varepsilon g(\mathbf{V}) \\ & \text{subject to} && (9.10), (9.13), (9.14) \quad \forall \phi \in \mathcal{P}_n, \forall n \in \mathcal{G} \\ & && 0.95 \leq |V_n^\phi| \leq 1.05, (9.7) \quad \forall \phi \in \mathcal{P}_n, \forall n \in \mathcal{N} \\ & && \mathbf{V}_1 = \begin{bmatrix} 1 & 1\angle -120^\circ & 1\angle 120^\circ \end{bmatrix}^T \\ & && \tan(\underline{\theta}_{kl}^\phi) \text{Tr} \left(\Phi_{Re,kl}^\phi \mathbf{V} \right) \leq \text{Tr} \left(\Phi_{Im,kl}^\phi \mathbf{V} \right) \quad \forall \phi \in \mathcal{P}_{kl} \\ & && \text{Tr} \left(\Phi_{Im,kl}^\phi \mathbf{V} \right) \leq \tan(\bar{\theta}_{kl}^\phi) \text{Tr} \left(\Phi_{Re,kl}^\phi \mathbf{V} \right) \quad \forall \phi \in \mathcal{P}_{kl} . \end{aligned} \quad (9.35)$$

We perform simulations on the network show in Figure 9.1. The objective function of (9.35) is $f(\mathbf{V}) = |V_{A2}|^2 = \text{Tr}(\Phi_{V,2}\mathbf{V})$. We place angle bounds where $k = A3$ and $l = A5$.

With angle bounds of $\underline{\theta}_{kl}^\phi = -0.005$ and $\bar{\theta}_{kl}^\phi = 0.005$, a rank-one solution is obtained with $\varepsilon = 0$ and $\mathcal{O}|\lambda_1/\lambda_2| \approx 10^7$. Solving power flow with the optimal DER dispatch from 9.35,

$V_{A3} = 0.9743\angle -1.1142^\circ$ and $V_{A5} = 0.9737\angle -1.1630^\circ$. The resultant voltage angles are within the imposed bounds.

With angle bounds of $\underline{\theta}_{kl}^\phi = -0.001$ and $\bar{\theta}_{kl}^\phi = 0.001$, a rank-one solution is obtained with $\varepsilon = 0$ and $\mathcal{O}|\lambda_1/\lambda_2| \approx 10^7$. Solving power flow with the optimal DER dispatch from 9.35, $V_{A3} = 0.9733\angle -1.1368^\circ$ and $V_{A5} = 0.9724\angle -1.1366^\circ$. The resultant voltage angles are within the imposed bounds.

While simulation results are promising, the lack of success in controlling voltage magnitude motivates the concerted analysis of controlling voltage magnitude and angle within an SDP formulation.

9.4 Conclusions

This chapter provided a discussion of the literature on SDP for OPF problems, and a preliminary study into SDP for controlling voltage magnitude and angle. While literature has detailed the success of SDP as a method for solving nonlinear and nonconvex OPFs, these works also highlighted drawbacks to the method. Simulation results motivate further analysis.

The first part of this chapter discusses recent works on SDP OPFs that show the method's promise, however, these works also outline why it may not be a viable method with current solvers. In [24], simulations have shown that a rank-one solution may not be obtainable, even for a feasible problem, when load line flow constraints are tightened. In [27], analysis has shown that too many equality constraints and binding inequality constraints will prevent convergence to a rank-one solution. In [29], to rectify convergence issues with certain cyclic networks, the authors suggest a possible solution of augmenting the objective function to penalize DER reactive power dispatch, thus changing the original problem. Finally, simulation results in [11] show that SDP convergence is sensitive to slack bus voltage. Recent literature points to methods for addressing some of these issues with iterative methods [26, 50, 51].

The second part of this chapter explores SDP as a method for solving OPFs for controlling voltage magnitude and angle. We derive SDP formulations for several OPFs for management of voltage magnitude and angle. Simulation results show that an OPF that tracks a voltage magnitude target will converge to a rank-one solution for higher target values, will converge to a rank-one solution for certain target values with a penalty on DER reactive power dispatch, and will not converge to a rank-one solution for lower target values.

A second simulation in which an OPF seeks to minimize voltage magnitude difference failed to produce a rank-one solution, despite the OPF modification proposed in [29]. A third simulation in which an OPF seeks to place constraints on voltage magnitude difference failed to produce a rank-one solution, despite the OPF modification proposed in [29]. Finally, a fourth simulation in which an OPF seeks to impose constraints on voltage angle difference successfully produced rank-one solutions for several bounds, without necessitating

the OPF modification proposed in [29]. These simulation results motivate further analysis into controlling voltage magnitude with SDP OPFs.

This work is not an exhaustive or definitive study on the efficacy of SDP OPFs in controlling voltage magnitude and angle, but rather an preliminary exploration. The lack of rank-one solutions for minimizing voltage magnitude difference, and lack of objective that minimizes voltage angle difference motivates the need for the investigation of other power flow models for DER optimization.

Chapter 10

Derivation of a Linearized Unbalanced Power Flow Model

10.1 Introduction

From the discussion of semidefinite programming presented in Chapter 9, it is clear that SDP and current solvers currently have drawbacks that may preclude its application to solve OPF large, multiphase, or meshed (cyclic) networks. With this in mind, we seek a novel model for unbalanced power flow model that can easily be incorporated into a convex optimization program.

Baran and Wu developed the *DistFlow* single phase power flow model in [9], and a simplified version of the *DistFlow* model in [8]. The simplified version contains linear power flow equations, except for the loss terms which are quadratic in real and reactive line power flows.

The *DistFlow* and its linearized version, often referred to as *LinDistFlow*, have been used for optimization and control of distribution network resources, along with network state estimation. In [12], the authors utilize a modified version of the simplified *simplified DistFlow* equations to develop local volt/var control schemes. The authors of [25] employ simplified *simplified DistFlow* in developing localized voltage regulation algorithms. In [10], the authors take advantage of the simplified *simplified DistFlow* system of equations to investigate linear approximations of the the power flow manifold.

The *DistFlow* has also been extended to three phase systems, as have the *simplified DistFlow* system of equations. Gan and Low [14] extend the *DistFlow* to three phases, and apply simplifying assumptions to obtain linear version of the *simplified DistFlow*. The authors conclude that for networks with small line losses and nearly balanced voltages, the linear approximation is accurate. The authors of [20] develop localized single phase and three phase voltage control schemes using the single phase and three phase *simplified DistFlow* equations. The authors also derive a version of the three phase *simplified DistFlow* for voltage regulation in [39]. The authors also derive approximations for previously omitted

nonlinear terms.

As the *simplified DistFlow* and its three phase counterpart are linear, the systems of equations can be incorporated into a linear program (LP) or quadratic program (QP), or other convex optimization programs. However, the models of [14], [20], and [39] do not contain the voltage phasor angle. To this end, we build upon the three phase *simplified DistFlow* by adding equations for voltage phase angle.

10.2 Derivation of Power and Losses for Unbalanced Approximate Power Flow

We now derive complex power and loss terms on a line $(m, n) \in \mathcal{E}$. This derivation follows that of [14] and [39] for three phases systems. Our derivation arrives at the same result as in [14], but with different nomenclature.

Power Referenced to Line Receiving Node

We now derive complex power and losses for lines $(l, m) \in \mathcal{E}$ and $(m, n) \in \mathcal{E}$ that connect to node $m \in \mathcal{N}$. This derivation follows that of [14] and [39] for three phases systems. Our derivation arrives at the same result as in [14], but with different nomenclature and method.

To start, we take the HP of \mathbf{V}_m and the complex conjugate (non-transposed) of (8.6):

$$\sum_{l:(l,m) \in \mathcal{E}} \mathbf{V}_m \circ \mathbf{I}_{lm}^* = \mathbf{V}_m \circ \mathbf{i}_m^* + \sum_{n:(m,n) \in \mathcal{E}} \mathbf{V}_m \circ \mathbf{I}_{mn}^* . \quad (10.1)$$

The \mathbf{V}_m term inside the summation on the RHS is substituted using (8.3):

$$\sum_{l:(l,m) \in \mathcal{E}} \mathbf{V}_m \circ \mathbf{I}_{lm}^* = \mathbf{V}_m \circ \mathbf{i}_m^* + \sum_{n:(m,n) \in \mathcal{E}} \mathbf{V}_n \circ \mathbf{I}_{mn}^* + (\mathbf{Z}_{mn} \mathbf{I}_{mn}) \circ \mathbf{I}_{mn}^* . \quad (10.2)$$

Here, we define the per phase complex power as $\mathbf{S}_{lm,m}^\phi = \mathbf{V}_m^\phi \left(\mathbf{I}_{lm}^\phi \right)^*$, and $\mathbf{S}_{mn,n}^\phi = \mathbf{V}_n^\phi \left(\mathbf{I}_{mn}^\phi \right)^*$, and the 3×1 vectors of complex power phasors $\mathbf{S}_{lm,m} = \mathbf{V}_m \circ \mathbf{I}_{lm}^*$ and $\mathbf{S}_{mn,n} = \mathbf{V}_n \circ \mathbf{I}_{mn}^*$ where $\mathbf{S}_{mn,n}$ is the power from node m to node n at node n , such that:

$$\sum_{l:(l,m) \in \mathcal{E}} \mathbf{S}_{lm,m} = \mathbf{s}_m + \sum_{n:(m,n) \in \mathcal{E}} \mathbf{S}_{mn,n} + \mathbf{L}_{mn} . \quad (10.3)$$

As we define $I_{mn}^\phi = 0 \forall \phi \notin \mathcal{P}_{mn}$ and $I_{mn}^\phi = 0 \forall \phi \notin \mathcal{P}_{mn}$, then clearly $S_{mn,n}^\phi = 0 \forall \phi \notin \mathcal{P}_{mn}$.

The term $\mathbf{L}_{mn} \in \mathbf{C}^{3 \times 1}$ is a nonlinear and non-convex loss term. Thus this equation will be difficult to incorporate into an optimization framework. We therefore introduce the following assumption:

A1: \mathbf{L}_{mn} is constant $\forall (m, n) \in \mathcal{E}$

Applying **A1** to (10.3) gives a linear equation for the conservation of complex power at node $m \in \mathcal{N}$, (10.4).

$$\sum_{l:(l,m) \in \mathcal{E}} \mathbf{S}_{lm,m} \approx \mathbf{s}_m + \sum_{n:(m,n) \in \mathcal{E}} \mathbf{S}_{mn,n} + \mathbf{L}_{mn} . \quad (10.4)$$

Additionally, following the analysis in [9] and [14], we introduce a second assumption:

$$\mathbf{A2:} \quad \mathbf{L}_{mn} = \begin{bmatrix} 0 & 0 & 0 \end{bmatrix}^T \quad \forall (m,n) \in \mathcal{E}$$

Assumption **A2** states that line losses are small compared to line flows, such that $|\mathbf{L}_{mn}^\phi| \ll |S_{mn}^\phi| \quad \forall \phi \in \mathcal{P}_{mn} \quad \forall (m,n) \in \mathcal{E}$ and can therefore be neglected. With this assumption applied to (10.4), we arrive at a simplified equation for the conservation of complex power (10.5):

$$\sum_{l:(l,m) \in \mathcal{E}} \mathbf{S}_{lm} \approx \mathbf{s}_m + \sum_{n:(m,n) \in \mathcal{E}} \mathbf{S}_{mn} . \quad (10.5)$$

It should be noted that when **A2** is applied, we will drop the second subscript denoting the node the power is referenced at. This is because if losses are assumed to be 0, then the power at the transmitting node and receiving node of a line are equivalent, such that $\mathbf{S}_{mn,m} = \mathbf{S}_{mn,n} = \mathbf{S}_{mn} \quad \forall (m,n) \in \mathcal{E}$, and $S_{mn}^\phi = 0 \quad \forall \phi \notin \mathcal{P}_{mn}$.

Power Referenced to Line Transmitting Node

In the previous subsection, we derived three phase complex power flow for lines connected to node $m \in \mathcal{N}$, with the power referenced to the receiving end of the line. While the transmitting and receiving end of a line $(m,n) \in \mathcal{E}$ can be arbitrarily chosen, referencing power at one end or the other may improve accuracy of a model, especially when using measured voltage and power values.

We now derive a similar set of equation to (10.2) – (10.5), however with line complex power defined at the line's transmitting node. We again start by taking the HP of \mathbf{V}_m and the complex conjugate (non-transposed) of (8.6):

$$\sum_{l:(l,m) \in \mathcal{E}} \mathbf{V}_m \circ \mathbf{I}_{lm}^* = \mathbf{V}_m \circ \mathbf{i}_m^* + \sum_{n:(m,n) \in \mathcal{E}} \mathbf{V}_m \circ \mathbf{I}_{mn}^* . \quad (10.6)$$

The \mathbf{V}_m term inside the summation on the LHS is substituted using (8.3) on line $(l,m) \in \mathcal{E}$:

$$\sum_{l:(l,m) \in \mathcal{E}} \mathbf{V}_l \circ \mathbf{I}_{lm}^* - (\mathbf{Z}_{lm} \mathbf{I}_{lm}) \circ \mathbf{I}_{lm}^* = \mathbf{V}_m \circ \mathbf{i}_m^* + \sum_{n:(m,n) \in \mathcal{E}} \mathbf{V}_m \circ \mathbf{I}_{mn}^* . \quad (10.7)$$

Here, we define the per phase complex power as $\mathbf{S}_{lm,l}^\phi = \mathbf{V}_l^\phi \left(\mathbf{I}_{lm}^\phi \right)^*$ and $\mathbf{S}_{mn,m}^\phi = \mathbf{V}_m^\phi \left(\mathbf{I}_{mn}^\phi \right)^*$. The 3×1 vector of complex power phasors are defined as $\mathbf{S}_{lm,l} = \mathbf{V}_l \circ \mathbf{I}_{lm}^*$ and $\mathbf{S}_{mn,m} = \mathbf{V}_m \circ \mathbf{I}_{mn}^*$ where $\mathbf{S}_{mn,m}$ is the power from node m to node n at node m , such that:

$$\sum_{l:(l,m) \in \mathcal{E}} \mathbf{S}_{lm,l} - \mathbf{L}_{lm} = \mathbf{s}_m + \sum_{n:(m,n) \in \mathcal{E}} \mathbf{S}_{mn,m} . \quad (10.8)$$

As we define $I_{mn}^\phi = 0 \forall \phi \notin \mathcal{P}_{mn}$, then clearly $S_{mn,m}^\phi = 0 \forall \phi \notin \mathcal{P}_{mn}$.

Similarly to (10.3), $\mathbf{L}_{lm} \in \mathbf{C}^{3 \times 1}$ is a nonlinear and non-convex loss term. Applying **A1** on line $(l, m) \in \mathcal{E}$ to (10.8) gives a linear equation for the conservation of complex power at node m , (10.9):

$$\sum_{l:(l,m) \in \mathcal{E}} \mathbf{S}_{lm,l} - \mathbf{L}_{lm} \approx \mathbf{s}_m + \sum_{n:(m,n) \in \mathcal{E}} \mathbf{S}_{mn,m} . \quad (10.9)$$

Additionally, applying **A2** further simplifies (10.9) into (10.10):

$$\sum_{l:(l,m) \in \mathcal{E}} \mathbf{S}_{lm} \approx \mathbf{s}_m + \sum_{n:(m,n) \in \mathcal{E}} \mathbf{S}_{mn} . \quad (10.10)$$

It should be noted that (10.5) and (10.10) are equivalent, as when **A2** is applied to a line $(m, n) \in \mathcal{E}$, $S_{mn,m}^\phi = S_{mn,n}^\phi = S_{mn}^\phi \forall \phi \in \mathcal{P}_{mn}$ and $\mathbf{S}_{mn,m} = \mathbf{S}_{mn,n} = \mathbf{S}_{mn}$ when losses are neglected.

10.3 Derivation of Voltage Magnitude Relations for Unbalanced Approximate Power Flow

In this section, we present a derivation for squared voltage magnitudes and complex multiphase power for unbalanced systems. This section follows derivations in [14, 39], however we present it in this work to keep a uniform nomenclature with the next section, to motivate the extension of the model to consider voltage angles in the following section, and to highlight a common structure shared between the voltage magnitude/complex power flow and voltage angle/complex power flow relationships.

The reader should note that here we present the derivation for a line with three phases where $\mathcal{P}_{mn} = \{a, b, c\}$. For lines with less than three phases ($|\mathcal{P}_{mn}| = 1$ or $|\mathcal{P}_{mn}| = 2$), all equations should be indexed by \mathcal{P}_{mn} as (8.4) is.

As in the previous section, Section 10.2, we will derive equations relating voltage magnitude to complex power flow first referencing voltage and power to the receiving node of a line, then the transmitting node.

Derivation of Magnitude Equation with Voltage and Power Referenced to Line Receiving Node

To start, we consider line $(m, n) \in \mathcal{E}$, and take the Hadamard Product of (8.3) and its complex conjugate (non-transposed):

$$\mathbf{V}_m \circ \mathbf{V}_m^* = (\mathbf{V}_n + \mathbf{Z}_{mn} \mathbf{I}_{mn}) \circ (\mathbf{V}_n + \mathbf{Z}_{mn} \mathbf{I}_{mn})^* . \quad (10.11)$$

This can be rewritten by distributing the terms on the RHS:

$$\mathbf{V}_m \circ \mathbf{V}_m^* = \mathbf{V}_n \circ \mathbf{V}_n^* + \mathbf{V}_n \circ (\mathbf{Z}_{mn} \mathbf{I}_{mn})^* + (\mathbf{Z}_{mn} \mathbf{I}_{mn}) \circ \mathbf{V}_n^* + (\mathbf{Z}_{mn} \mathbf{I}_{mn}) \circ (\mathbf{Z}_{mn} \mathbf{I}_{mn})^* . \quad (10.12)$$

Now, we define the real scalar:

$$E_m^\phi = |V_m^\phi|^2 = V_m^\phi (V_m^\phi)^* , \quad (10.13)$$

the 3×1 real vector:

$$\mathbf{E}_m = \begin{bmatrix} E_m^a & E_m^b & E_m^c \end{bmatrix}^T = \mathbf{V}_m \circ \mathbf{V}_m^* , \quad (10.14)$$

and the 3×1 real vector:

$$\mathbf{H}_{mn} = (\mathbf{Z}_{mn} \mathbf{I}_{mn}) \circ (\mathbf{Z}_{mn} \mathbf{I}_{mn})^* = (\mathbf{V}_m - \mathbf{V}_n) \circ (\mathbf{V}_m - \mathbf{V}_n)^* . \quad (10.15)$$

With these definitions, we also take advantage of the commutative property of the HP and group the second and third terms of the RHS of (10.12) inside the real operator, as they are the complex conjugate of each other:

$$\mathbf{E}_m = \mathbf{E}_n + 2 \operatorname{Re} \{ (\mathbf{Z}_{mn} \mathbf{I}_{mn})^* \circ \mathbf{V}_n \} + \mathbf{H}_{mn} . \quad (10.16)$$

We expand $(\mathbf{Z}_{mn} \mathbf{I}_{mn})^* \circ \mathbf{V}_n$ to obtain:

$$\mathbf{E}_m = \mathbf{E}_n + 2 \operatorname{Re} \left\{ \begin{bmatrix} V_n^a (Z_{mn}^{aa} I_{mn}^a + Z_{mn}^{ab} I_{mn}^b + Z_{mn}^{ac} I_{mn}^c)^* \\ V_n^b (Z_{mn}^{ba} I_{mn}^a + Z_{mn}^{bb} I_{mn}^b + Z_{mn}^{bc} I_{mn}^c)^* \\ V_n^c (Z_{mn}^{ca} I_{mn}^a + Z_{mn}^{cb} I_{mn}^b + Z_{mn}^{cc} I_{mn}^c)^* \end{bmatrix} \right\} + \mathbf{H}_{mn} . \quad (10.17)$$

Now, we use the definition of complex power at the receiving node where $(I_{mn}^\phi)^* = S_{mn,n}^\phi / V_n^\phi$, and define the term $\gamma_n^{\phi\psi} = V_n^\phi / V_n^\psi$, thus expand (10.17) to (10.18):

$$\mathbf{E}_m = \mathbf{E}_n + 2 \operatorname{Re} \left\{ \begin{bmatrix} (Z_{mn}^{aa})^* S_{mn,n}^a + \gamma_n^{ab} (Z_{mn}^{ab})^* S_{mn,n}^b + \gamma_n^{ac} (Z_{mn}^{ac})^* S_{mn,n}^c \\ \gamma_n^{ba} (Z_{mn}^{ba})^* S_{mn,n}^a + (Z_{mn}^{bb})^* S_{mn,n}^b + \gamma_n^{bc} (Z_{mn}^{bc})^* S_{mn,n}^c \\ \gamma_n^{ca} (Z_{mn}^{ca})^* S_{mn,n}^a + \gamma_n^{cb} (Z_{mn}^{cb})^* S_{mn,n}^b + (Z_{mn}^{cc})^* S_{mn,n}^c \end{bmatrix} \right\} + \mathbf{H}_{mn} . \quad (10.18)$$

The 3×1 vector on the RHS can be separated into a 3×3 matrix multiplied by the 3×1 vector $\mathbf{S}_{mn,n}$:

$$\mathbf{E}_m = \mathbf{E}_n + 2 \operatorname{Re} \left\{ \begin{bmatrix} (Z_{mn}^{aa})^* & \gamma_n^{ab} (Z_{mn}^{ab})^* & \gamma_n^{ac} (Z_{mn}^{ac})^* \\ \gamma_n^{ba} (Z_{mn}^{ba})^* & (Z_{mn}^{bb})^* & \gamma_n^{bc} (Z_{mn}^{bc})^* \\ \gamma_n^{ca} (Z_{mn}^{ca})^* & \gamma_n^{cb} (Z_{mn}^{cb})^* & (Z_{mn}^{cc})^* \end{bmatrix} \begin{bmatrix} S_{mn,n}^a \\ S_{mn,n}^b \\ S_{mn,n}^c \end{bmatrix} \right\} + \mathbf{H}_{mn} . \quad (10.19)$$

Defining the matrix $\Gamma_n \in \mathbb{C}^{3 \times 3}$ as:

$$\Gamma_n = \mathbf{V}_n (1/\mathbf{V}_n)^T = \begin{bmatrix} 1 & \gamma_n^{ab} & \gamma_n^{ac} \\ \gamma_n^{ba} & 1 & \gamma_n^{bc} \\ \gamma_n^{ca} & \gamma_n^{cb} & 1 \end{bmatrix} , \quad (10.20)$$

we can use the definition of the HP to separate the 3×3 matrix into two 3×3 matrices as in:

$$\mathbf{E}_m = \mathbf{E}_n + 2 \operatorname{Re} \{ (\Gamma_n \circ \mathbf{Z}_{mn}^*) \mathbf{S}_{mn,n} \} + \mathbf{H}_{mn} . \quad (10.21)$$

Finally, we apply the real operator (Re) on the RHS, separating the complex power vector into its active and reactive components, $\mathbf{S}_{mn,n} = \mathbf{P}_{mn,n} + j\mathbf{Q}_{mn,n}$, to arrive at:

$$\begin{aligned} \mathbf{E}_m &= \mathbf{E}_n + 2\mathbf{M}_{mn,n}\mathbf{P}_{mn,n} - 2\mathbf{N}_{mn,n}\mathbf{Q}_{mn,n} + \mathbf{H}_{mn} \\ \mathbf{M}_{mn,n} &= \operatorname{Re} \{ \Gamma_n \circ \mathbf{Z}_{mn}^* \} \\ \mathbf{N}_{mn,n} &= \operatorname{Im} \{ \Gamma_n \circ \mathbf{Z}_{mn}^* \} . \end{aligned} \quad (10.22)$$

We have derived equations that govern the relationship between squared voltage magnitudes and complex power flow across line (m, n) . This system of equations is nonlinear and nonconvex system, and therefore cannot be incorporated into a convex optimization framework without the use of approximations or convex relaxations. However, this system can be linearized with the following assumptions:

A3: \mathbf{H}_{mn} is constant $\forall (m, n) \in \mathcal{E}$

A4: $\gamma_n^{\phi\psi}$ are constant $\forall \phi, \psi \in \mathcal{P}_n, \phi \neq \psi, \forall n \in \mathcal{N}$

Application of assumptions **A3** and **A4** to (10.23) results in a linear model that relates the squared magnitudes of nodal voltages and complex power flows to DER injected power.

$$\mathbf{E}_m \approx \mathbf{E}_n + 2\mathbf{M}_{mn,n}\mathbf{P}_{mn,n} - 2\mathbf{N}_{mn,n}\mathbf{Q}_{mn,n} + \mathbf{H}_{mn} . \quad (10.23)$$

The magnitude equations can be further simplified via logical choices for the constant parameters of **A3** and **A4**. Following the analysis presented in [9], we choose $\mathbf{H}_{mn} = [0 \ 0 \ 0]^T \forall (m, n) \in \mathcal{E}$. As in [14] and [39], we assign the $\gamma_n^{\phi\psi}$ such that:

$$\begin{aligned} \gamma_n^{ab} = \alpha \quad \gamma_n^{bc} = \alpha \quad \gamma_n^{ac} = \alpha^2 \\ \gamma_n^{ba} = \alpha^2 \quad \gamma_n^{cb} = \alpha^2 \quad \gamma_n^{ca} = \alpha \end{aligned} \quad \forall n \in \mathcal{N} \equiv \Gamma_n = \begin{bmatrix} 1 & \alpha & \alpha^2 \\ \alpha^2 & 1 & \alpha \\ \alpha & \alpha^2 & 1 \end{bmatrix} \quad \forall n \in \mathcal{N} , \quad (10.24)$$

where $\alpha = 1\angle 120^\circ = \frac{1}{2}(-1 + j\sqrt{3})$ and $\alpha^2 = \alpha^{-1} = \alpha^* = 1\angle 240^\circ$.

With these choices for \mathbf{H}_{mn} and $\gamma_n^{\phi\psi}$, we obtain a linear system of equations relation the difference in voltage magnitude across line (m, n) to real and reactive power flows on the line:

$$\mathbf{E}_m \approx \mathbf{E}_n + 2\mathbf{M}_{mn}\mathbf{P}_{mn,n} - 2\mathbf{N}_{mn}\mathbf{Q}_{mn,n} , \quad (10.25)$$

$$\mathbf{M}_{mn} = \frac{1}{2} \begin{bmatrix} 2r_{mn}^{aa} & -r_{mn}^{ab} + \sqrt{3}x_{mn}^{ab} & -r_{mn}^{ac} - \sqrt{3}x_{mn}^{ac} \\ -r_{mn}^{ba} - \sqrt{3}x_{mn}^{ba} & 2r_{mn}^{bb} & -r_{mn}^{bc} + \sqrt{3}x_{mn}^{bc} \\ -r_{mn}^{ca} + \sqrt{3}x_{mn}^{ca} & -r_{mn}^{cb} - \sqrt{3}x_{mn}^{cb} & 2r_{mn}^{cc} \end{bmatrix} , \quad (10.26)$$

$$\mathbf{N}_{mn} = \frac{1}{2} \begin{bmatrix} -2x_{mn}^{aa} & x_{mn}^{ab} + \sqrt{3}r_{mn}^{ab} & x_{mn}^{ac} - \sqrt{3}r_{mn}^{ac} \\ x_{mn}^{ba} - \sqrt{3}r_{mn}^{ba} & -2x_{mn}^{bb} & x_{bc} + \sqrt{3}r_{mn}^{bc} \\ x_{mn}^{ca} + \sqrt{3}r_{mn}^{ca} & x_{mn}^{cb} - \sqrt{3}r_{mn}^{cb} & -2x_{mn}^{cc} \end{bmatrix}. \quad (10.27)$$

Magnitude Equation Reference to Line Transmitting Node

Similar to Section 10.2, the magnitude equations can be rederived to reference node voltages at the transmitting end of the line.

To start, consider line $(m, n) \in \mathcal{E}$ with the voltage difference due to line impedance taken on the left side. We then take the Hadamard Product of (8.3) and its complex conjugate (non-transposed):

$$(\mathbf{V}_m - \mathbf{Z}_{mn}\mathbf{I}_{mn}) \circ (\mathbf{V}_m - \mathbf{Z}_{mn}\mathbf{I}_{mn})^* = \mathbf{V}_n \circ \mathbf{V}_n^*. \quad (10.28)$$

This can be rewritten by distributing the terms on the LHS:

$$\mathbf{V}_m \circ \mathbf{V}_m^* - \mathbf{V}_m \circ (\mathbf{Z}_{mn}\mathbf{I}_{mn})^* - (\mathbf{Z}_{mn}\mathbf{I}_{mn}) \circ \mathbf{V}_m^* + (\mathbf{Z}_{mn}\mathbf{I}_{mn}) \circ (\mathbf{Z}_{mn}\mathbf{I}_{mn})^* = \mathbf{V}_n \circ \mathbf{V}_n^*. \quad (10.29)$$

With the definitions of \mathbf{E}_m , \mathbf{E}_n , \mathbf{H}_{mn} , we again take advantage of the commutative property of the HP and group the second and third terms of the LHS of (10.29) inside the real operator:

$$\mathbf{E}_m - 2 \operatorname{Re} \{ (\mathbf{Z}_{mn}\mathbf{I}_{mn})^* \circ \mathbf{V}_m \} + \mathbf{H}_{mn} = \mathbf{E}_n. \quad (10.30)$$

At this point, we will focus on the terms inside the real operator (**Re**) and expand $(\mathbf{Z}_{mn}\mathbf{I}_{mn})^* \circ \mathbf{V}_m$ to obtain:

$$\mathbf{E}_m - 2 \operatorname{Re} \left\{ \begin{bmatrix} V_m^a (Z_{mn}^{aa} I_{mn}^a + Z_{mn}^{ab} I_{mn}^b + Z_{mn}^{ac} I_{mn}^c)^* \\ V_m^b (Z_{mn}^{ba} I_{mn}^a + Z_{mn}^{bb} I_{mn}^b + Z_{mn}^{bc} I_{mn}^c)^* \\ V_m^c (Z_{mn}^{ca} I_{mn}^a + Z_{mn}^{cb} I_{mn}^b + Z_{mn}^{cc} I_{mn}^c)^* \end{bmatrix} \right\} + \mathbf{H}_{mn} = \mathbf{E}_n. \quad (10.31)$$

Now, we use the definition of complex power at the line transmitting node, where $(I_{mn}^\phi)^* = S_{mn}^\phi / V_m^\phi$, and define the term $\gamma_m^{\phi\psi} = V_m^\phi / V_m^\psi$, thus expand (10.31) to (10.32):

$$\mathbf{E}_m - 2 \operatorname{Re} \left\{ \begin{bmatrix} (Z_{mn}^{aa})^* S_{mn,m}^a + \gamma_m^{ab} (Z_{mn}^{ab})^* S_{mn,m}^b + \gamma_m^{ac} (Z_{mn}^{ac})^* S_{mn,m}^c \\ \gamma_m^{ba} (Z_{mn}^{ba})^* S_{mn,m}^a + (Z_{mn}^{bb})^* S_{mn,m}^b + \gamma_m^{bc} (Z_{mn}^{bc})^* S_{mn,m}^c \\ \gamma_m^{ca} (Z_{mn}^{ca})^* S_{mn,m}^a + \gamma_m^{cb} (Z_{mn}^{cb})^* S_{mn,m}^b + (Z_{mn}^{cc})^* S_{mn,m}^c \end{bmatrix} \right\} + \mathbf{H}_{mn} = \mathbf{E}_n. \quad (10.32)$$

The 3×1 vector on the RHS can be separated into a 3×3 matrix multiplied by the 3×1 vector \mathbf{S}_{mn} .

$$\mathbf{E}_m - 2 \operatorname{Re} \left\{ \begin{bmatrix} (Z_{mn}^{aa})^* & \gamma_m^{ab} (Z_{mn}^{ab})^* & \gamma_m^{ac} (Z_{mn}^{ac})^* \\ \gamma_m^{ba} (Z_{mn}^{ba})^* & (Z_{mn}^{bb})^* & \gamma_m^{bc} (Z_{mn}^{bc})^* \\ \gamma_m^{ca} (Z_{mn}^{ca})^* & \gamma_m^{cb} (Z_{mn}^{cb})^* & (Z_{mn}^{cc})^* \end{bmatrix} \begin{bmatrix} S_{mn,m}^a \\ S_{mn,m}^b \\ S_{mn,m}^c \end{bmatrix} \right\} + \mathbf{H}_{mn} = \mathbf{E}_n. \quad (10.33)$$

With the definition of $\Gamma_m \in \mathbb{C}^{3 \times 3}$ as $\Gamma_m = \mathbf{V}_m (1/\mathbf{V}_m)^T$, we can use the definition of the HP to separate the 3×3 matrix into two 3×3 matrices as in:

$$\mathbf{E}_m - 2 \operatorname{Re} \{ (\Gamma_m \circ \mathbf{Z}_{mn}^*) \mathbf{S}_{mn,m} \} + \mathbf{H}_{mn} = \mathbf{E}_n . \quad (10.34)$$

Finally, we apply the real operator on the LHS, separating the complex power vector into its active and reactive components, $\mathbf{S}_{mn,m} = \mathbf{P}_{mn,m} + j\mathbf{Q}_{mn,m}$, to arrive at:

$$\begin{aligned} \mathbf{E}_m &= \mathbf{E}_n + 2\mathbf{M}_{mn,m}\mathbf{P}_{mn,m} - 2\mathbf{N}_{mn,m}\mathbf{Q}_{mn,m} - \mathbf{H}_{mn} \\ \mathbf{M}_{mn,m} &= \operatorname{Re} \{ \Gamma_m \circ \mathbf{Z}_{mn}^* \} \\ \mathbf{N}_{mn,m} &= \operatorname{Im} \{ \Gamma_m \circ \mathbf{Z}_{mn}^* \} . \end{aligned} \quad (10.35)$$

It is interesting to note, at this point, that (10.22) and (10.35) are quite similar, with the difference being that (10.22) has the matrix Γ_n and line powers $\mathbf{S}_{mn,n}$ defined at node n and the higher order term \mathbf{H}_{mn} positive on the RHS, while (10.35) has the matrix Γ_m and line powers $\mathbf{S}_{mn,m}$ defined at node m and the higher order term \mathbf{H}_{mn} negative on the RHS.

As with the previously derived magnitude equations with power and voltage referred to the receiving node, these equations are nonlinear and nonconvex, and we employ the assumptions **A3** and **A4** in the same manner. Application of assumptions **A3** and **A4** to (10.35) results in a linear model that relates the squared magnitudes of nodal voltages and complex power flows to DER injected power.

$$\mathbf{E}_m \approx \mathbf{E}_n + 2\mathbf{M}_{mn,m}\mathbf{P}_{mn,m} - 2\mathbf{N}_{mn,m}\mathbf{Q}_{mn,m} - \mathbf{H}_{mn} . \quad (10.36)$$

Similar to the previous derivation, choosing $\mathbf{H}_{mn} = [0 \ 0 \ 0]^T \forall (m, n) \in \mathcal{E}$, and $\gamma^{\phi\psi}$ such that:

$$\begin{aligned} \gamma_m^{ab} = \alpha \quad \gamma_m^{bc} = \alpha \quad \gamma_m^{ac} = \alpha^2 \\ \gamma_m^{ba} = \alpha^2 \quad \gamma_m^{cb} = \alpha^2 \quad \gamma_m^{ca} = \alpha \end{aligned} \quad \forall m \in \mathcal{N} \equiv \Gamma_m = \begin{bmatrix} 1 & \alpha & \alpha^2 \\ \alpha^2 & 1 & \alpha \\ \alpha & \alpha^2 & 1 \end{bmatrix} \quad \forall m \in \mathcal{N} , \quad (10.37)$$

we arrive at a linearized relation between voltage magnitude and complex power:

$$\mathbf{E}_m \approx \mathbf{E}_n + 2\mathbf{M}_{mn}\mathbf{P}_{mn,m} - 2\mathbf{N}_{mn}\mathbf{Q}_{mn,m} , \quad (10.38)$$

with \mathbf{M}_{mn} and \mathbf{N}_{mn} defined by (10.26) and (10.27), respectively.

10.4 Derivation of Voltage Angle Relations for Unbalanced Approximate Power Flow

We now derive an extension of the power and magnitude system that relates differences in voltage angles between adjacent nodes to complex power flows. This derivation shares many similarities with the analysis of Section 10.3. The derivation presented here represents a three phase line, $\mathcal{P}_{mn} = \{a, b, c\}$. For lines with less than three phases ($|\mathcal{P}_{mn}| = 1$ or $|\mathcal{P}_{mn}| = 2$), all equations should be indexed by \mathcal{P}_{mn} as (8.4) is.

This work adds to that of [14] and [39] by adding an equation for voltage angle.

Motivational Example

Consider a line $(m, n) \in \mathcal{E}$. For simplicity, we assume the line is single phase, and therefore omit the phase superscript ϕ . The power across (m, n) at node m is:

$$S_{mn,m} = V_m I_{mn}^* = V_m (V_m - V_n)^* / Z_{mn}^* .$$

Multiplying the numerator and denominator the impedance of the line Z_{mn} :

$$S_{mn,m} = |V_m|^2 Z_{mn} / |Z_{mn}|^2 - V_m V_n^* Z_{mn} / |Z_{mn}|^2 .$$

For simplicity, we will assume that $|Z_{mn}| = 1$, and expand the terms of previous equation into their respective complex components:

$$S_{mn,m} = |V_m|^2 (r_{mn} + jx_{mn}) - |V_m| |V_n| (\cos(\theta_m - \theta_n) + j \sin(\theta_m - \theta_n)) (r_{mn} + jx_{mn}) .$$

Grouping the real and reactive power components:

$$\begin{aligned} S_{mn,m} &= |V_m|^2 r_{mn} - |V_m| |V_n| (r_{mn} \cos(\theta_m - \theta_n) - x_{mn} \sin(\theta_m - \theta_n)) \dots \\ &\quad + j (|V_m|^2 x_{mn} - |V_m| |V_n| (x_{mn} \cos(\theta_m - \theta_n) + r_{mn} \sin(\theta_m - \theta_n))) . \end{aligned}$$

At this point, it is clear that power flow across the line (m, n) is dependent on the both the difference in voltage magnitude between node m and n , but also the difference in voltage angle between node m and n . To further illustrate the dependence on voltage angle, we assume that the voltage magnitude at node m and node n are equal such that $|V_m| = |V_n|$:

$$\begin{aligned} S_{mn,m} &= |V_m|^2 (r_{mn} - r_{mn} \cos(\theta_m - \theta_n) + x_{mn} \sin(\theta_m - \theta_n)) \dots \\ &\quad + j |V_m|^2 (x_{mn} - x_{mn} \cos(\theta_m - \theta_n) - r_{mn} \sin(\theta_m - \theta_n)) . \end{aligned}$$

From this equation, it is clear that differences in voltage angle between the two node m and n will cause power to flow on (m, n) . The power and magnitude equations presented in this work, [14], and [39], and the SDP formulation in [11], are suited to control the real and reactive power flow on lines of a distribution network.

However, these formulations are not suited to the scenario of closing a switch between two nodes, where power will begin to flow on the newly created line. With the switch open, the nodes are disconnected, and no power flows, and therefore power flow cannot be controlled.

We seek to build upon the approximate unbalanced power flow model to allow for control of voltage angle, such that control of the complete phasor is possible. Such control will enable “cleaner” switching actions wherein a minimal voltage difference across an open switch will prevent otherwise large, and potentially equipment damaging or dangerous, power surges.

Angle Equations with Voltage and Power Referenced to Line Receiving Node

We begin by taking the HP of the complex conjugate of (8.3) and \mathbf{V}_n :

$$\mathbf{V}_m^* \circ \mathbf{V}_n = \mathbf{V}_n^* \circ \mathbf{V}_n + (\mathbf{Z}_{mn} \mathbf{I}_{mn})^* \circ \mathbf{V}_n . \quad (10.39)$$

With the results from the Section 10.3, we can substitute both terms on the RHS, and expand the LHS with the polar representations of voltage phasors:

$$\begin{bmatrix} |V_m^a| |V_n^a| \angle (-\theta_m^a + \theta_n^a) \\ |V_m^b| |V_n^b| \angle (-\theta_m^b + \theta_n^b) \\ |V_m^c| |V_n^c| \angle (-\theta_m^c + \theta_n^c) \end{bmatrix} = \mathbf{E}_n + (\Gamma_n \circ \mathbf{Z}_{mn}^*) \mathbf{S}_{mn,n} . \quad (10.40)$$

To be consistent with convention in the power and magnitude equations, we multiply both sides by -1 . We then take the imaginary component of both sides:

$$\begin{bmatrix} |V_m^a| |V_n^a| \sin(\theta_m^a - \theta_n^a) \\ |V_m^b| |V_n^b| \sin(\theta_m^b - \theta_n^b) \\ |V_m^c| |V_n^c| \sin(\theta_m^c - \theta_n^c) \end{bmatrix} = -\mathbf{Im} \{ (\Gamma_n \circ \mathbf{Z}_{mn}^*) \mathbf{S}_{mn,n} \} . \quad (10.41)$$

Finally, we apply the imaginary operator to the RHS of (10.41):

$$\begin{bmatrix} |V_m^a| |V_n^a| \sin(\theta_m^a - \theta_n^a) \\ |V_m^b| |V_n^b| \sin(\theta_m^b - \theta_n^b) \\ |V_m^c| |V_n^c| \sin(\theta_m^c - \theta_n^c) \end{bmatrix} = -\mathbf{N}_{mn,n} \mathbf{P}_{mn,n} - \mathbf{M}_{mn,n} \mathbf{Q}_{mn,n} , \quad (10.42)$$

with $\mathbf{M}_{mn,n}$ and $\mathbf{N}_{mn,n}$ defined as in (10.23).

Inspection of the voltage angle equation reveals some interesting properties compared to the voltage magnitude equations of (10.22). The RHS of Eqs. (10.22) and (10.42) are the real and imaginary parts of the same argument (except for a scaling factor of one-half).

The angle equation (10.42) is nonlinear and nonconvex, and therefore difficult to incorporate into an OPF. Therefore, we introduce the following three assumptions:

A4: $\gamma_n^{\phi\psi}$ are constant $\forall \phi, \psi \in \mathcal{P}_n, \phi \neq \psi, \forall n \in \mathcal{N}$

A5: $|\nabla_m^\phi|$ and $|\nabla_n^\phi|$ are constant $\forall \phi \in \mathcal{P}_{mn}, \forall (m, n) \in \mathcal{N}$

A6: $\sin(\theta_m^\phi - \theta_n^\phi) \approx \theta_m^\phi - \theta_n^\phi$, via small angle approximation, $\forall \phi \in \mathcal{P}_{mn}, \forall (m, n) \in \mathcal{E}$

It should be noted that **A4** is the same as in Section 10.3, and is applied to both the magnitude and angle equations. Furthermore, the reader should note that **A5** is only applied to (10.42). We now define $|V_n^\phi| = e_n^\phi \forall \phi \in \mathcal{P}_n \forall n \in \mathcal{N}$ with $\mathbf{e}_n = [e_n^a \ e_n^b \ e_n^c]^T \forall n \in \mathcal{N}$ as

a set of fixed voltage magnitude references, assumed to be constant despite control action. Application of **A4**, **A5**, and **A6** to (10.42), gives a linear version of (10.42):

$$\mathbf{e}_m \circ \mathbf{e}_n \circ \Theta_m \approx \mathbf{e}_m \circ \mathbf{e}_n \circ \Theta_n - \mathbf{N}_{mn,n} \mathbf{P}_{mn,n} - \mathbf{M}_{mn,n} \mathbf{Q}_{mn,n} , \quad (10.43)$$

where $\Theta_m = [\theta_m^a \ \theta_m^b \ \theta_m^c]^T$. This linear equation can further be simplified by selecting $\gamma_n^{\phi\psi}$ as in (10.24) so that \mathbf{M}_{mn} and \mathbf{N}_{mn} are defined as in (10.26) and (10.27), respectively:

$$\mathbf{e}_m \circ \mathbf{e}_n \circ \Theta_m \approx \mathbf{e}_m \circ \mathbf{e}_n \circ \Theta_n - \mathbf{N}_{mn} \mathbf{P}_{mn,n} - \mathbf{M}_{mn} \mathbf{Q}_{mn,n} . \quad (10.44)$$

Should the network voltage magnitudes be unknown or unmeasurable, they can be assumed to be that of the typical substation nominal voltage magnitude of 1, thus (10.44) becomes (10.45):

$$\Theta_m \approx \Theta_n - \mathbf{N}_{mn} \mathbf{P}_{mn,n} - \mathbf{M}_{mn} \mathbf{Q}_{mn,n} . \quad (10.45)$$

Angle Equations with Voltage Referenced to Line Transmitting Node

Similar the previous two sections, we can rederive the angle equation by referencing the voltage ratios γ and power to the transmitting node of the line. We start with by taking the HP of \mathbf{V}_m and the complex conjugate (non-transposed) of KVL on line (m, n) :

$$\mathbf{V}_m^* \circ \mathbf{V}_m = \mathbf{V}_n^* \circ \mathbf{V}_m + (\mathbf{Z}_{mn} \mathbf{I}_{mn}) \circ \mathbf{V}_m . \quad (10.46)$$

With the definitions of the power and magnitude equation derivations, we rearrange both sides:

$$\mathbf{E}_m = \begin{bmatrix} |V_m^a| |V_n^a| \angle (\theta_m^a - \theta_n^a) \\ |V_m^b| |V_n^b| \angle (\theta_m^b - \theta_n^b) \\ |V_m^c| |V_n^c| \angle (\theta_m^c - \theta_n^c) \end{bmatrix} + (\Gamma_m \circ \mathbf{Z}_{mn}^*) \mathbf{S}_{mn,m} . \quad (10.47)$$

Taking the imaginary components of both sides eliminates the LHS:

$$0 = \begin{bmatrix} |V_m^a| |V_n^a| \sin (\theta_m^a - \theta_n^a) \\ |V_m^b| |V_n^b| \sin (\theta_m^b - \theta_n^b) \\ |V_m^c| |V_n^c| \sin (\theta_m^c - \theta_n^c) \end{bmatrix} + \mathbf{Im} \{ (\Gamma_m \circ \mathbf{Z}_{mn}^*) \mathbf{S}_{mn,m} \} . \quad (10.48)$$

Applying the \mathbf{Im} operator and subtracting the second term from both sides leads to an equation similar to that of (10.49):

$$\begin{bmatrix} |V_m^a| |V_n^a| \sin (\theta_m^a - \theta_n^a) \\ |V_m^b| |V_n^b| \sin (\theta_m^b - \theta_n^b) \\ |V_m^c| |V_n^c| \sin (\theta_m^c - \theta_n^c) \end{bmatrix} = -\mathbf{N}_{mn,m} \mathbf{P}_{mn,m} - \mathbf{M}_{mn,m} \mathbf{Q}_{mn,m} . \quad (10.49)$$

Applying **A4**, **A5**, and **A6** to (10.49) gives (10.50):

$$\mathbf{e}_m \circ \mathbf{e}_n \circ \Theta_m \approx \mathbf{e}_m \circ \mathbf{e}_n \circ \Theta_n - \mathbf{N}_{mn,m} \mathbf{P}_{mn,m} - \mathbf{M}_{mn,m} \mathbf{Q}_{mn,m} . \quad (10.50)$$

This linear equation can further be simplified by selecting $\gamma_n^{\phi\psi}$ as in (10.24) so that \mathbf{M}_{mn} and \mathbf{N}_{mn} are defined as in (10.26) and (10.27), respectively:

$$\mathbf{e}_m \circ \mathbf{e}_n \circ \Theta_m \approx \mathbf{e}_m \circ \mathbf{e}_n \circ \Theta_n - \mathbf{N}_{mn} \mathbf{P}_{mn,m} - \mathbf{M}_{mn} \mathbf{Q}_{mn,m} . \quad (10.51)$$

If the voltage magnitudes are unknown, 10.44 can be simplified by assuming all voltage magnitudes are roughly 1, giving 10.52:

$$\Theta_m \approx \Theta_n - \mathbf{N}_{mn} \mathbf{P}_{mn,m} - \mathbf{M}_{mn} \mathbf{Q}_{mn,m} . \quad (10.52)$$

10.5 Linearized Unbalanced Power Flow Model

We now present a set of equations comprising a LUPFM for multiphase radial and mesh networks.

In the previous sections, we have derived an equation for unbalanced multiphase power flow, equations relating voltage magnitude to complex unbalanced power flow, and equations relating voltage angle to complex unbalanced power flow. For each of these, linearizing assumptions were applied only to the respective equations, without considering the other equations. We now apply assumptions to all three equations to obtain a comprehensive and linear approximate power flow model.

The first equation is for a complex load on phase ϕ at node n , where $A_{PQ,n}^\phi + A_{Z,n}^\phi = 1 \forall \phi \in \mathcal{P}_n, \forall n \in \mathcal{N}$ and $A_{I,n}^\phi = 0 \forall \phi \in \mathcal{P}_n, \forall n \in \mathcal{N}$:

$$\begin{aligned} s_n^\phi (V_n^\phi) &= \left(A_{PQ,n}^\phi + A_{Z,n}^\phi E_n^\phi \right) d_n^\phi + w_n^\phi - j c_n^\phi \\ \mathbf{s}_n (\mathbf{V}_n) &= (\mathbf{A}_{PQ,n} + \mathbf{A}_{Z,n} \circ \mathbf{E}_n) \circ \mathbf{d}_n + \mathbf{w}_n - j \mathbf{c}_n . \end{aligned} \quad (10.53)$$

A2 is applied to the power equation, such that:

$$\begin{aligned} \mathbf{S}_{mn,m} = \mathbf{S}_{mn,n} = \mathbf{S}_{mn} \quad \forall (m,n) \in \mathcal{E} \\ \sum_{l:(l,m) \in \mathcal{E}} \mathbf{S}_{lm} \approx \mathbf{s}_m + \sum_{n:(m,n) \in \mathcal{E}} \mathbf{S}_{mn} . \end{aligned} \quad (10.54)$$

A3 is applied to the magnitude equation where $\mathbf{H}_{mn} = \begin{bmatrix} 0 & 0 & 0 \end{bmatrix}^T \forall (m,n) \in \mathcal{E}$, and **A4** is applied with $\Gamma_m = \Gamma_n = \Gamma$ according to (10.24), such that:

$$\mathbf{E}_m \approx \mathbf{E}_n + 2\mathbf{M}_{mn} \mathbf{P}_{mn} - 2\mathbf{N}_{mn} \mathbf{Q}_{mn} , \quad (10.55)$$

with \mathbf{M}_{mn} and \mathbf{N}_{mn} and defined as in (10.58).

A4 with $\Gamma_m = \Gamma_n = \Gamma$ according to (10.24), **A5**, and **A6** are applied to the angle equation, such that:

$$\mathbf{e}_m \circ \mathbf{e}_n \circ \Theta_m \approx \mathbf{e}_m \circ \mathbf{e}_n \circ \Theta_n - \mathbf{N}_{mn} \mathbf{P}_{mn} - \mathbf{M}_{mn} \mathbf{Q}_{mn} . \quad (10.56)$$

with \mathbf{M}_{mn} and \mathbf{N}_{mn} and defined as in (10.58) Finally, if no fixed voltage references are chosen or available, they can be assigned as 1, such that $e_n^\phi = 1 \forall \phi \in \mathcal{P}_n \forall n \in \mathcal{N}$:

$$\Theta_m \approx \Theta_n - \mathbf{N}_{mn} \mathbf{P}_{mn} - \mathbf{M}_{mn} \mathbf{Q}_{mn} . \quad (10.57)$$

with \mathbf{M}_{mn} and \mathbf{N}_{mn} and defined as in (10.58):

$$\mathbf{M}_{mn} = \frac{1}{2} \begin{bmatrix} 2r_{mn}^{aa} & -r_{mn}^{ab} + \sqrt{3}x_{mn}^{ab} & -r_{mn}^{ac} - \sqrt{3}x_{mn}^{ac} \\ -r_{mn}^{ba} - \sqrt{3}x_{mn}^{ba} & 2r_{mn}^{bb} & -r_{mn}^{bc} + \sqrt{3}x_{mn}^{bc} \\ -r_{mn}^{ca} + \sqrt{3}x_{mn}^{ca} & -r_{mn}^{cb} - \sqrt{3}x_{mn}^{cb} & 2r_{mn}^{cc} \end{bmatrix} \quad (10.58)$$

$$\mathbf{N}_{mn} = \frac{1}{2} \begin{bmatrix} -2x_{mn}^{aa} & x_{mn}^{ab} + \sqrt{3}r_{mn}^{ab} & x_{mn}^{ac} - \sqrt{3}r_{mn}^{ac} \\ x_{mn}^{ba} - \sqrt{3}r_{mn}^{ba} & -2x_{mn}^{bb} & x_{mn}^{bc} + \sqrt{3}r_{mn}^{bc} \\ x_{mn}^{ca} + \sqrt{3}r_{mn}^{ca} & x_{mn}^{cb} - \sqrt{3}r_{mn}^{cb} & -2x_{mn}^{cc} \end{bmatrix} .$$

The linear model presented in this section assumes three phase nodes and lines. For lines with $\mathcal{P}_{mn} \neq \{a, b, c\}$, (10.55), (10.56), (10.57), and (10.58) should be indexed as described in Section 8.1.

Chapter 11

Accuracy Analysis of Linearized Unbalanced Power Flow Approximation

The LUPFM contains several linearizing assumptions with selection of nominal parameters, thus investigation into the accuracy of these approximations is warranted. Such an analysis can give insight into not only the accuracy of the assumptions, but also under what conditions the assumptions fail to reflect actual power flow.

To investigate this accuracy, we perform a Monte Carlo simulation on a modified version of the IEEE 13 node test feeder [18], the topology of which can be seen in 11.1. In this version, the voltage regulator between nodes 650 and 632 is omitted, the transformer between nodes 633 and 634 is replaced by a line of configuration 601 and length of 50 feet, and the switch between node 671 and 692 is replaced by a line with configuration 601 and length of 50 feet. A node representing a transmission line is appended to the network, connecting to node 650, with a fixed voltage reference of $\begin{bmatrix} 1 & 1\angle 240^\circ & 1\angle 120^\circ \end{bmatrix}^T$. This node is treated as an infinite bus such that connection with the distribution network does not affect transmission line voltage. Node phases are given in Table A.6, and line phases and per-unit impedances are given in Table A.7.

Node are assigned complex power demands with the real, and reactive, demand components randomly chosen from uniform distribution between 0 and a maximum real, and reactive demand, respectively. The maximum component demands are independently increased in increments of 0.01 p.u. from 0.01 p.u. to 0.15 p.u. At each combination of maximum real and reactive demand, 25 simulations are conducted. At each simulation, base power flow is solved using a Newton-Raphson method comprising the load model (8.8), KVL (8.4), and KCL (8.6), adapted from [48]. Approximate power flow is solved with a Newton-Raphson method of the LUPFM comprised of (10.53), (10.54), (10.55), (10.58), and either (10.56) or (10.57).

To explore the effect of using fixed known or measured voltage magnitudes values in the

angle equations, we consider two cases for approximate power flow. The first, which will be referred to as case 1, assumes that all voltage magnitudes are either unknown or are close enough to 1, such that $e_n^\phi = 1 \forall \phi \in \mathcal{P}_n, \forall n \in \mathcal{N}$ in (10.44). In the second case, referred to as case 2, e_n^ϕ are fixed to the voltage magnitudes from the results of solving the base case power flow.

The error between base and approximate power flow results are given by (11.1) - (11.4), where the overline notation indicates the approximate power flow solution.

$$\varepsilon_{\text{magnitude}} = \max_{\phi \in \mathcal{P}_n, n \in \mathcal{N}} \left| |V_n^\phi| - \left| \overline{V}_n^\phi \right| \right| \quad (11.1)$$

$$\varepsilon_{\text{angle}} = \max_{\phi \in \mathcal{P}_n, n \in \mathcal{N}} \left| \angle V_n^\phi - \angle \overline{V}_n^\phi \right| \quad (11.2)$$

$$\varepsilon_{\text{vector}} = \max_{\phi \in \mathcal{P}_n, n \in \mathcal{N}} \left| V_n^\phi - \overline{V}_n^\phi \right| \quad (11.3)$$

$$\varepsilon_{\text{power}} = \max_{\phi \in \mathcal{P}_{mn}, (m,n) \in \mathcal{E}} \left| S_{mn,n}^\phi - \overline{S}_{mn}^\phi \right|. \quad (11.4)$$

The maximum voltage magnitude error across all phases and nodes is given by (11.1). The maximum voltage angle error across all phases and nodes is given by (11.2). The maximum voltage phasor error across all phases and nodes is given by (11.3), which is also known as the total vector error. The maximum error in apparent power across all phases and nodes is given by (11.4).

Figure 11.2 plots the maximum voltage magnitude error between the voltage from solving power flow with KVL and KCL, and approximate voltage solving power flow with the linearized equations. A quadratic trend in error is quite visible as substation power increases. When the substation power is 1 p.u., the voltage magnitude error remains under 0.005 p.u. for all tested cases. As the substation power increases (as do the node loads) the magnitude errors become more pronounced, increasing to a range between 0.005 p.u. and 0.01 p.u. as the substation power reaches 1.5 p.u. As the approximate power flow magnitude relation (10.25) is same for both approximate power flow cases, there is no difference in magnitude error between cases.

Figure 11.3 gives the error in apparent power between base case power flow and approximate power flow. As the linearized power equations, (8.8) and (10.5), are the same for case 1 and case 2 there is no difference in error between case 1 and case for the iterations. Similar to the other errors, the apparent power error follows a quadratic trend in increasing substation power. When substation power is 1.0 p.u, the error remains under 0.04 p.u.

Figure 11.4a gives the maximum voltage angle error for all nodes and phases for increasing substation power for the case 1 of approximate power flow, where $e_n^\phi = 1 \forall \phi \in \mathcal{P}_n \forall n \in \mathcal{N}$ in (10.44). When substation power is 1.0 p.u., the errors are less than 0.2° . The maximum total vector error for all phases and nodes across increasing substation power is given in Figure 11.4b. This is the magnitude of the greatest voltage vector difference between the real and approximate power flow solutions. This can be thought of as a ball in which the voltage from the approximate power flow solution resides in.

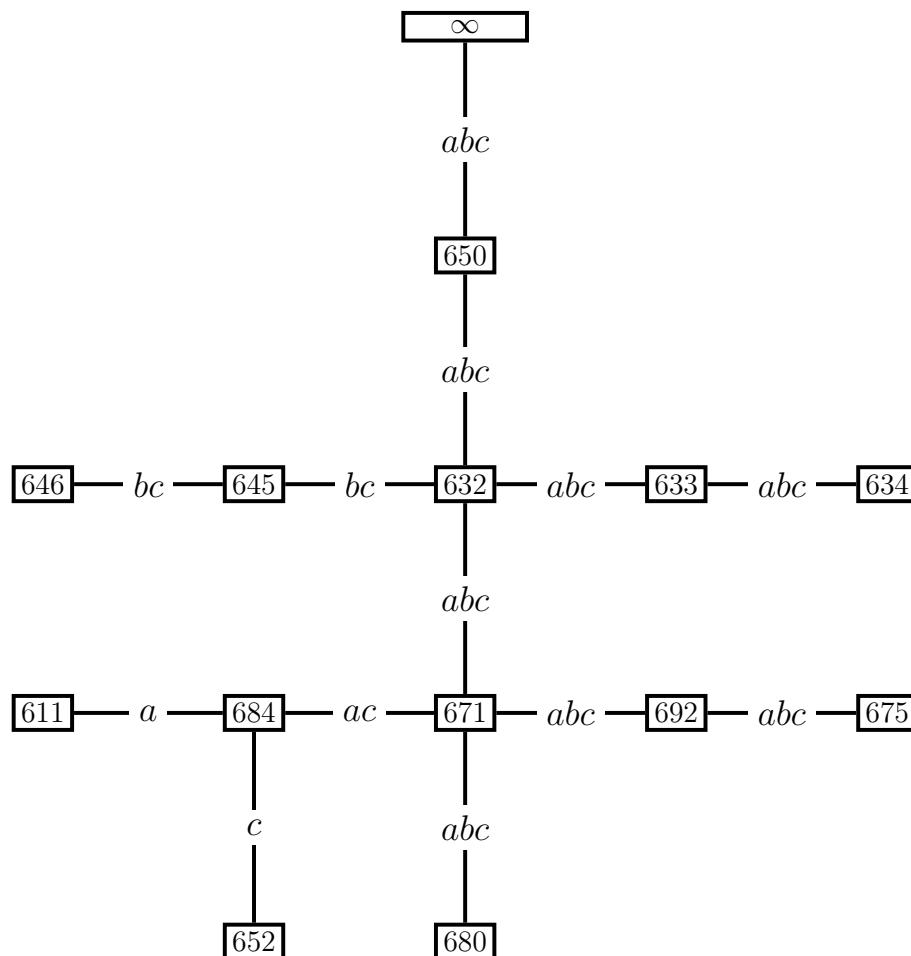


Figure 11.1: Modified IEEE 13 node feeder topology for Monte Carlo accuracy analysis of unbalanced approximate power flow mode. Note absence of voltage regulator between nodes 650 and 632, transformer between nodes 633 and 634, and switch between nodes 671 and 692.

Figure 11.5a gives the maximum voltage angle error for all nodes and phases for increasing substation power for the case 2 of approximate power flow where the voltage magnitudes in (10.44) are assigned from the results of base case power flow. It can clearly be seen that the errors are less than the previous case. When substation power is 1.0 p.u., the errors are less than 0.2° . The maximum total vector error for all phases and nodes across increasing substation power is given in Figure 11.5b. Similarly, this error is lower than that of approximate power flow case 1. It is clear that using measured voltage magnitudes in (10.44) and (10.51) increases the accuracy of the approximation.

As base case and approximate power flow are solved with a node representing the transmission line treated as a slack bus with nominal voltage phasor, it is clear the errors are compounded along the network moving away from the transmission line node. Nodes fur-

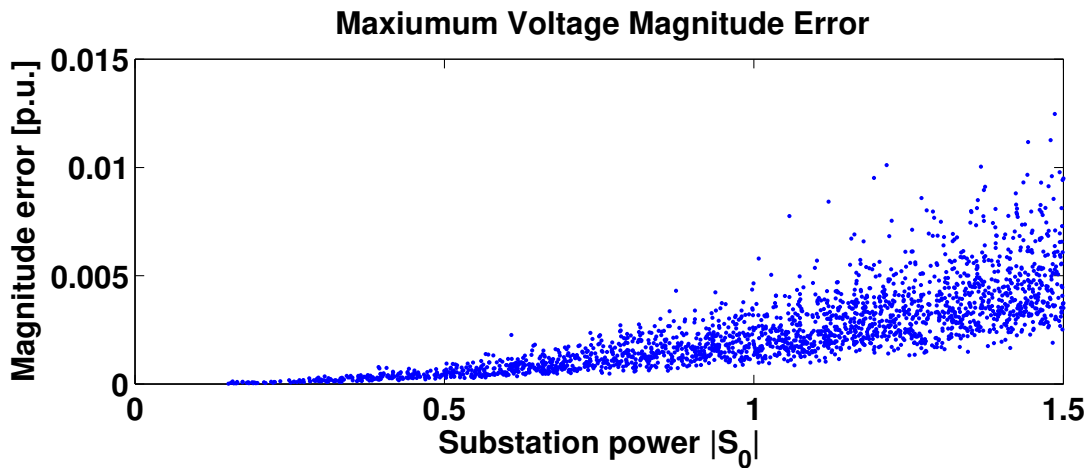


Figure 11.2: Maximum voltage magnitude error across all phases and nodes from Monte Carlo simulation.

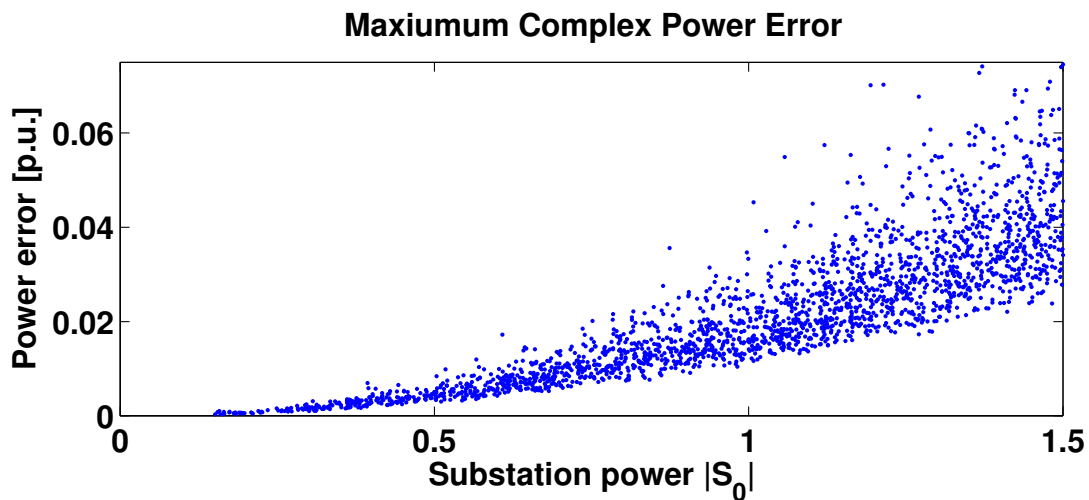
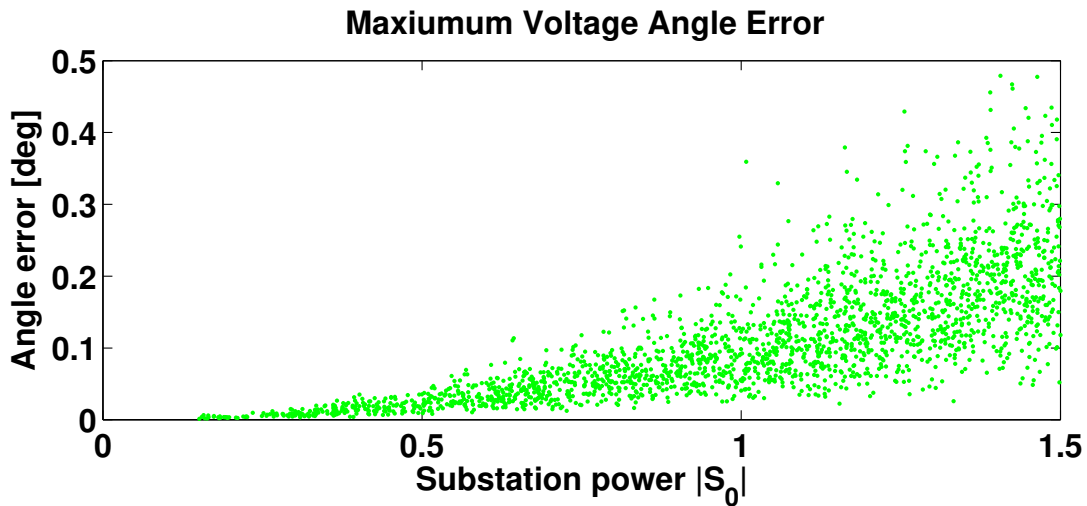


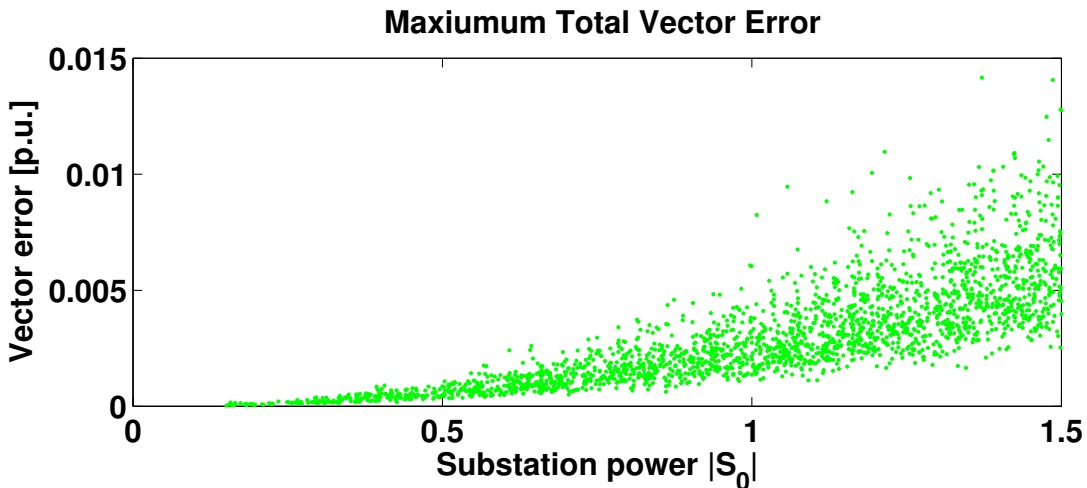
Figure 11.3: Apparent power error from Monte Carlo simulation.

ther away from the substation are more likely to have larger errors in voltage magnitude and angle due to error accumulation. Additionally, nodes with large demands, and therefore large power flows on connecting lines will also have larger errors due the necessity of neglecting losses for linearization.

Conversely, “tail nodes” or nodes that are far from the substation and have only one path to the substation will have accurate approximate power flows. This is due to the conservation of complex power, (10.5). Errors will compound from tail these nodes toward the substation, as losses are neglected in (10.5) and (10.10) to obtaining linear equations.

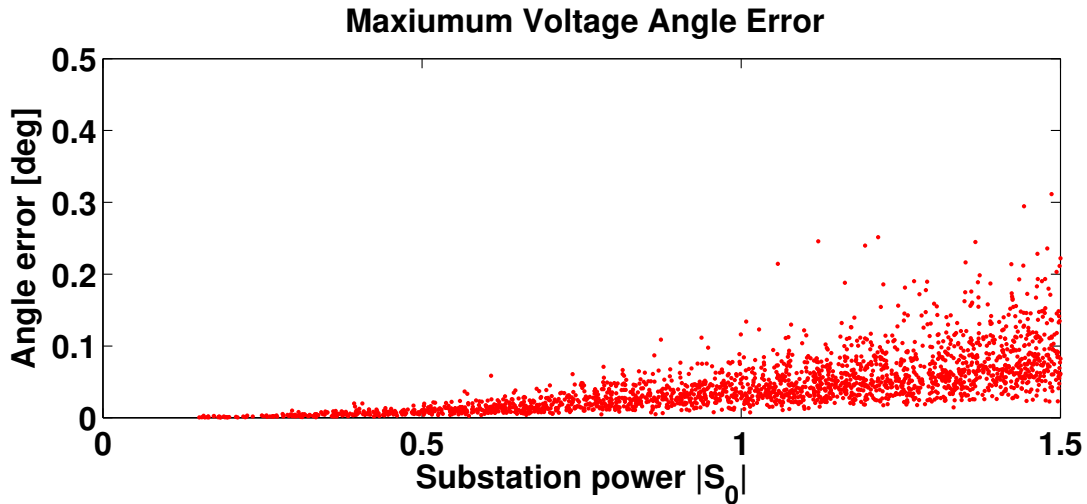


(a) Maximum voltage angle error across all phases and nodes from Monte Carlo simulation, for case where all voltage magnitudes are assumed to be 1 in angle equations, (10.44).

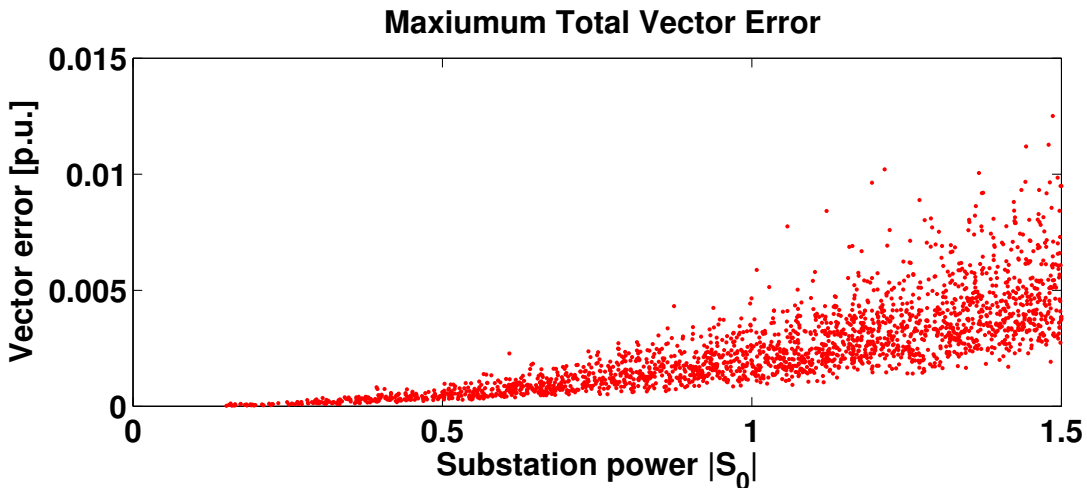


(b) Maximum voltage total vector error across all phases and nodes from Monte Carlo simulation, for case where all voltage magnitudes are assumed to be 1 in angle equations, (10.44).

Figure 11.4: Monte Carlo simulation results for voltage angle error and total vector error for case where all voltage magnitudes are assumed to be 1 in (10.44).



(a) Maximum voltage angle error across all phases and nodes from Monte Carlo simulation, for case where voltage magnitudes in (10.44) are fixed to the values from solving power flow.



(b) Maximum voltage total vector error across all phases and nodes from Monte Carlo simulation, for case where voltage magnitudes in (10.44) are fixed to the values from solving power flow.

Figure 11.5: Monte Carlo simulation results for voltage angle error and total vector error for case where voltage magnitudes in (10.44) are assigned to the values from solving power flow.

Chapter 12

Applications of the Linearized Unbalanced Power Flow Model

Control and optimization of DER on balanced networks is a topic that has encompassed much research effort. In recent years, these efforts have been extended to multiphase unbalanced networks, presenting new challenges in mathematical modeling and application of optimization techniques. In this chapter, we discuss two applications of the equations for LUPFM for optimal control of DER on distribution networks.

12.1 Voltage Magnitude Balancing

In this section, we discuss an experiment in which we incorporate linearized power, magnitude, and angle equations in an OPF that controls DERs to regulate and balance voltage magnitudes on an unbalanced radial distribution network. Voltage balancing is an important objective as many three phase loads (induction motors for instance) are sensitive to high levels of imbalance. Furthermore, many 3-phase voltage regulation equipment actuates based solely on single phase measurements. Therefore, significant levels of imbalance can lead to improper operation of these devices.

The goal of this experiment is to minimize the total voltage magnitude imbalance across the feeder. Voltage magnitude imbalance is defined as the absolute error of the difference of voltage magnitude between two difference phases at a node. The voltage imbalance at node n is defined as:

$$\Upsilon_n = \sum_{\substack{\phi \in \mathcal{P}_n, \psi \in \mathcal{P}_n \\ \phi \neq \psi}} \left| |V_n^\phi| - |V_n^\psi| \right|. \quad (12.1)$$

For nodes with one phase ($|\mathcal{P}_n| = 1$) $\Upsilon_n = 0$ The total network voltage magnitude imbalance is define as:

$$\Upsilon_{\mathcal{N}} = \sum_{n \in \mathcal{N}} \sum_{\substack{\phi \in \mathcal{P}_n, \psi \in \mathcal{P}_n \\ \phi \neq \psi}} \left| |V_n^\phi| - |V_n^\psi| \right|. \quad (12.2)$$

We design an OPF to minimize network voltage magnitude imbalance, regulate system voltage magnitude to within acceptable limits. The OPF also account for DER apparent power constraints and regulates the dispatch. This OPF, (12.3) is:

$$\begin{aligned}
 & \underset{u_n^\phi, v_n^\phi, E_n^\phi, P_{mn}^\phi, Q_{mn}^\phi}{\text{minimize}} && \sum_{n \in \mathcal{N}} \left[\sum_{\substack{\phi \in \mathcal{P}_n, \psi \in \mathcal{P}_n \\ \phi \neq \psi}} (E_n^\phi - E_n^\psi)^2 \right] + \left[\sum_{\phi \in \mathcal{P}_n} \rho_w |w_n^\phi|^2 \right] \\
 & \text{subject to} && (10.53), (10.54), (10.55), (10.58), (10.56) \\
 & && \underline{E}_n^\phi \leq E_n^\phi \leq \overline{E}_n^\phi \quad \forall \phi \in \mathcal{P}_n, \quad \forall n \in \mathcal{N} \\
 & && |w_n^\phi| \leq \overline{w}_n^\phi \quad \forall \phi \in \mathcal{P}_n, \quad \forall n \in \mathcal{N} .
 \end{aligned} \tag{12.3}$$

In 12.3, the DER dispatch apparent power constraints, $|w_n^\phi| \leq \overline{w}_n^\phi \quad \forall \phi \in \mathcal{P}_n, \quad \forall n \in \mathcal{N}$ can be approximated by a series of linear equations as derived in Appendix C, such that (12.3) is a true quadratic program.

It should be noted that comparison of either case to an SDP formulation of (12.3) we were not able to obtain a rank-one solution to an equivalent problem formulated as an SDP.

Voltage Magnitude Balance Experiment on a Radial Network

We perform this experiment on a modified version of the IEEE 13 node test feeder [18], the topology of which can be seen in 12.1. In this version, the voltage regulator between nodes 650 and 632 is omitted, the transformer between nodes 633 and 634 is replaced by a line of configuration 601 and length of 50 feet, and the switch between node 671 and 692 is replaced by a line with configuration 601 and length of 50 feet. Additionally, a node representing a transmission line is appended to the network, connecting to node 650, with a fixed voltage reference of $\begin{bmatrix} 1 & 1\angle 240^\circ & 1\angle 120^\circ \end{bmatrix}^T$. This node is treated as an infinite bus such that connection with the distribution network does not affect transmission line voltage. A transformer is placed between node 650 and the transmission line, with impedance as specified in [18]. Node parameters and phases can be found in Table A.6. Line parameters, phases and impedances can be found in Table A.7.

All capacitors, listed in Table A.9, are omitted. Node demands, listed in Table A.8, are specified by [18], are multiplied by a factor of 1.125, and are assumed to follow the model of (8.8) with $A_{PQ,n}^\phi = 0.85$, $A_{I,n}^\phi = 0$, and $A_{Z,n}^\phi = 0.15 \quad \forall \phi \in \mathcal{P}_n \quad \forall n \in \mathcal{N}$.

DER are placed on all existing phases of nodes 632, 675, 680, and 684. DER are assumed to be single phase inverters capable of four quadrant operation, where the dispatch of one phase is independent of others at the same node. The DER have an apparent power limit of 0.025 p.u., or 125 kW. DER placement, phases and apparent power capacity can be found in Table A.10. The penalty on DER dispatch is weighted with $\rho_w = 0.5$. Voltage magnitude bounds were $0.95 \leq |V_n^\phi| \leq 1.05$ such that $\underline{E}_n^\phi = 0.9025$ and $\overline{E}_n^\phi = 1.1025$.

The first case we consider is the base case with no DER dispatch, where $w_n^\phi = 0 \forall \phi \in \mathcal{P}_n \forall n \in \mathcal{N}$. The second case is the control case, where DER dispatch is given by (12.3). For both cases, power flow is solved using a Newton-Raphson method adapted from [48], comprised of (8.4), (8.6), and (8.8).

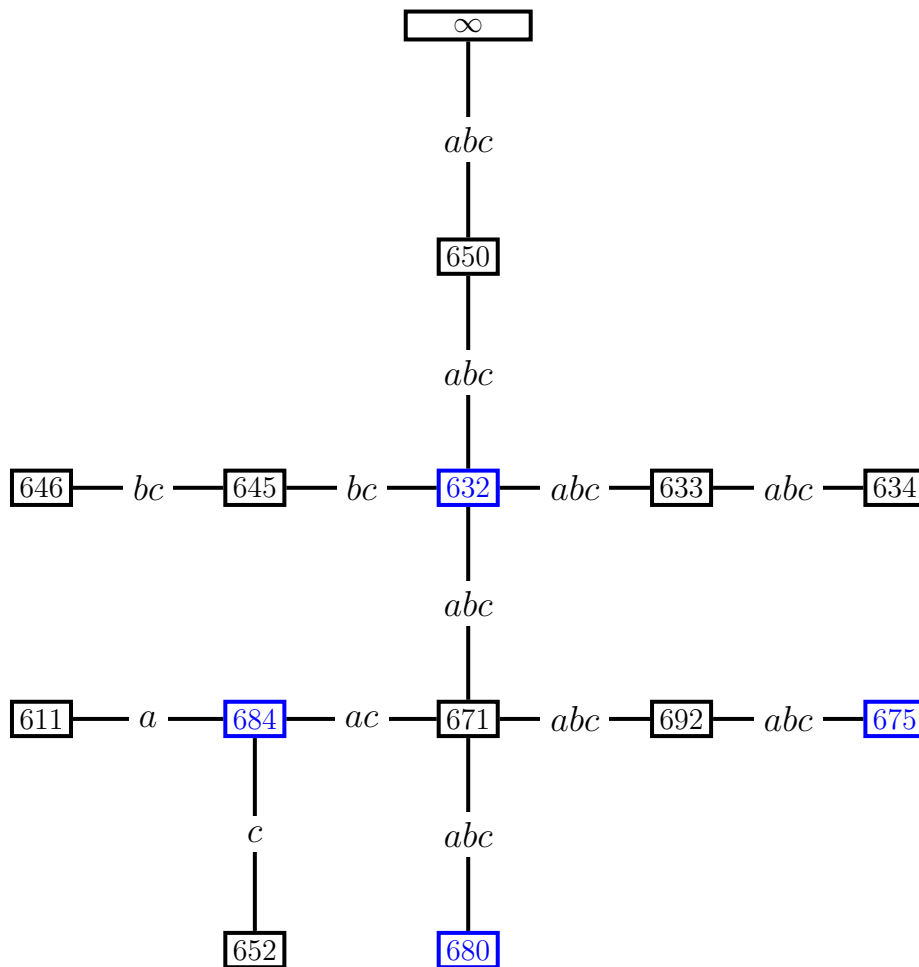


Figure 12.1: Modified IEEE 13 node feeder topology. Note absence of voltage regulator between nodes 650 and 632, transformer between nodes 633 and 634, and switch between nodes 671 and 692. DER are present at blue nodes.

Figure 12.2 shows the voltage magnitudes for the base case of the voltage balancing scenario. A significant imbalance in the voltage magnitude between phase b and phases a and c is clearly visible. Additionally, there are several minimum voltage violations on phase c .

Figure 12.3 shows the voltage magnitudes for the control case of the voltage balancing scenario. The reduction in voltage magnitude imbalance between the base case and control case is easily seen.

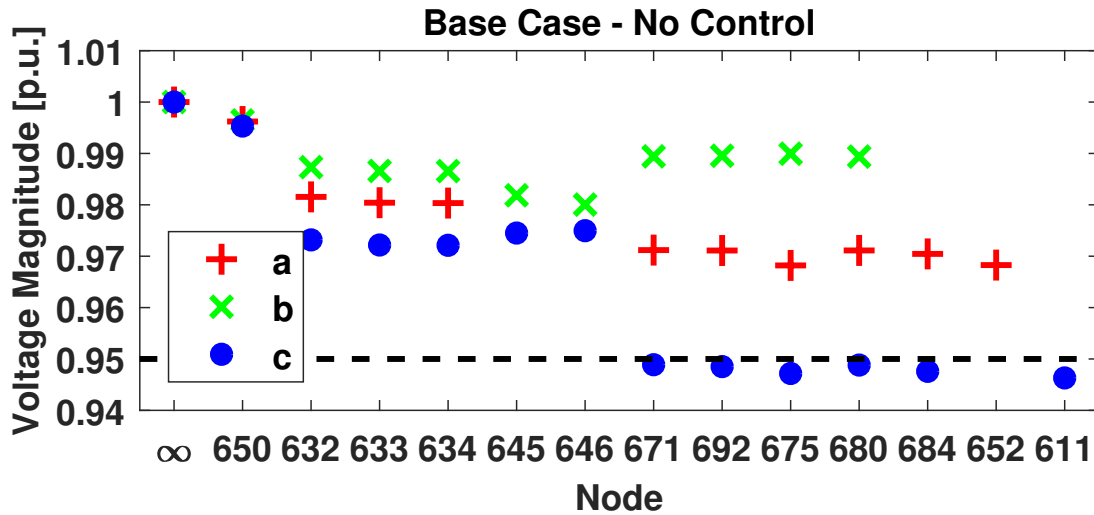


Figure 12.2: Base case (no control) of voltage balancing scenario for modified IEEE 13 node feeder.

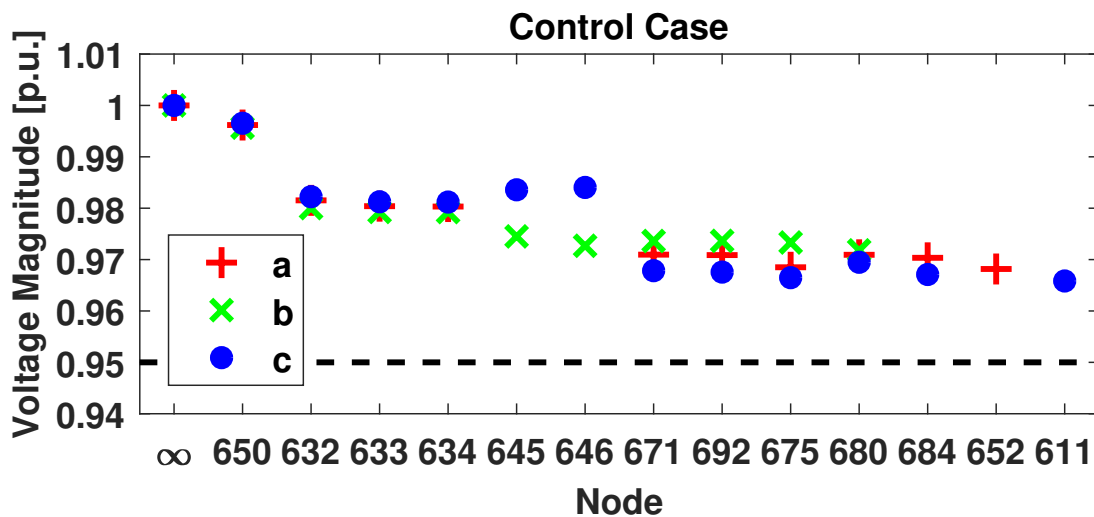


Figure 12.3: Control case of voltage balancing scenario for modified IEEE 13 node feeder, with DER dispatch from (12.3).

Figure 12.4 plots the voltage imbalance for the base case and control for each node, as given by (12.1). The reduction in imbalance is clearly visible, and more pronounced at nodes further from the substation. As nodes 652 and 611 have only 1 phase each, there is no metric of voltage imbalance and therefore the imbalance is not plotted for these nodes. The total network imbalance, as defined by (12.2), is 0.4533 for the base case and 0.0797 for the control case. The optimal DER dispatch from (12.3) for the IEEE 13 node network is given in Table 12.1.

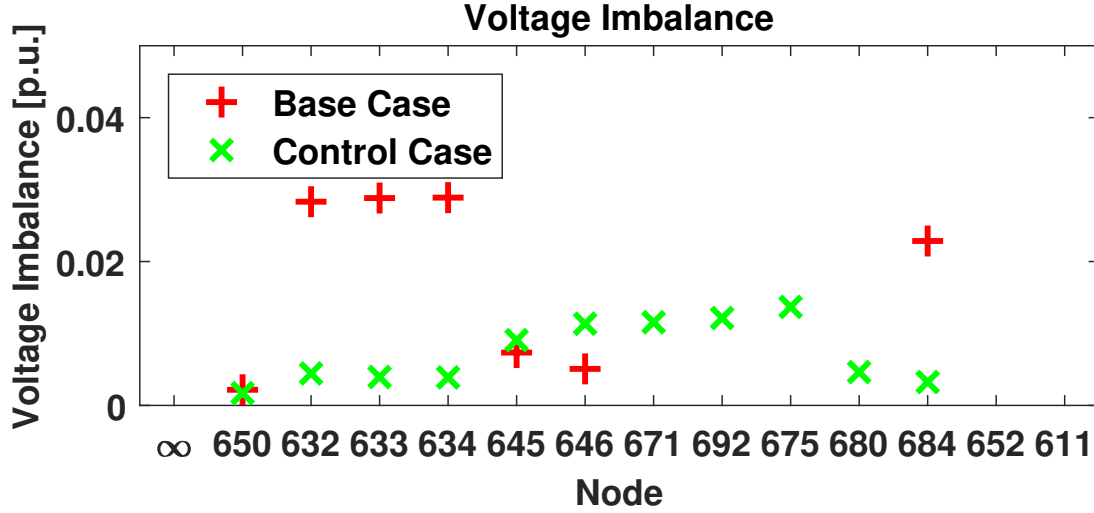


Figure 12.4: Comparison of voltage magnitude imbalance for IEEE 13 node feeder between base case and control case.

Node	Phase a w_n^a	Phase b w_n^b	Phase c w_n^c
632	$0.00600 - j0.00174$	$-0.00573 - j0.00956$	$0.00077 + j0.01159$
675	$-0.01242 + j0.00386$	$0.01277 + j0.01571$	$-0.00236 - j0.01980$
680	$-0.01197 + j0.00354$	$0.01109 + j0.01533$	$-0.00115 - j0.01896$
684	$-0.01110 + j0.00381$	-	$-0.00159 - j0.01837$

Table 12.1: Optimal DER dispatch for voltage magnitude balancing from (12.3).

Voltage Magnitude Balancing Experiment on a Mesh Network

We consider a second experiment for voltage magnitude balancing on a multiphase mesh network. This mesh network includes nodes and lines with multiple phases, lines with phases that are a subset of the set of phases of the connected nodes. The topology of the mesh network is given by Figure 12.5.

All lines are assigned the configuration of 601 from the IEEE 13 node test feeder [18], with a length of 150 meters. The line between $(\infty, M1)$ is treated the same as in the transformer between the transmission line and substation in [18]. Node parameters and phases are given in Table A.11. Line nodes, phases, and impedance are given in Table A.12.

Node demands are given in Table A.13. All demands follow the model of (8.8) with $A_{PQ,n}^\phi = 0.85$, $A_{I,n}^\phi = 0$, and $A_{Z,n}^\phi = 0.15 \forall \phi \in \mathcal{P}_n \forall n \in \mathcal{N}$. Capacitor parameters are given in Table A.14.

DER were placed at nodes $\mathcal{G} = \{M2, M3, M4, M6, M7\}$. DER is assumed to be able to source or sink both real and reactive power independently. DER on difference phases on a node is assumed to be able to operate independently. DER operation is assumed to

be limited by a maximum apparent power capacity, \overline{w}_n^ϕ . DER placement and parameters are given in Table A.15. Voltage magnitude bounds were $0.95 \leq |V_n^\phi| \leq 1.05$ such that $\underline{E}_n^\phi = 0.9025$ and $\overline{E}_n^\phi = 1.1025$.

The first case we consider is the base case with no DER dispatch, where $w_n^\phi = 0 \forall \phi \in \mathcal{P}_n \forall n \in \mathcal{N}$. The second case is the control case, where DER dispatch is given by (12.3). For both cases, power flow is solved using a Newton-Raphson method adapted from [48], comprised of (8.4), (8.6), and (8.8).

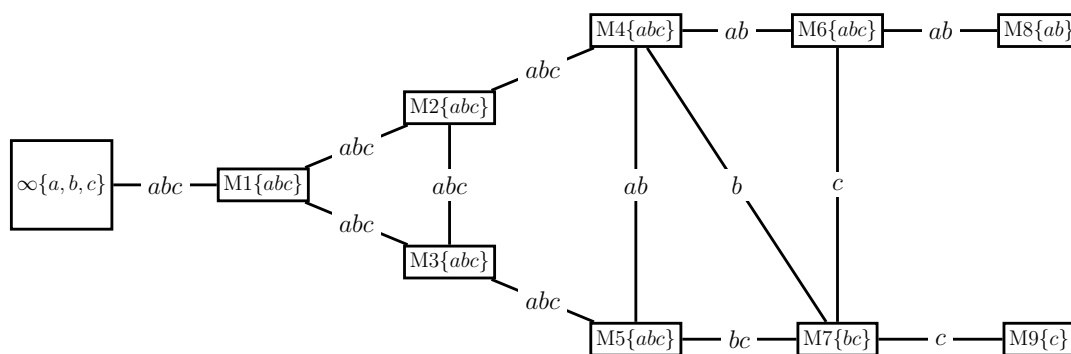


Figure 12.5: Nine node mesh network. Node names and phases \mathcal{P}_m are shown, as well as the line phases \mathcal{P}_{mn} .

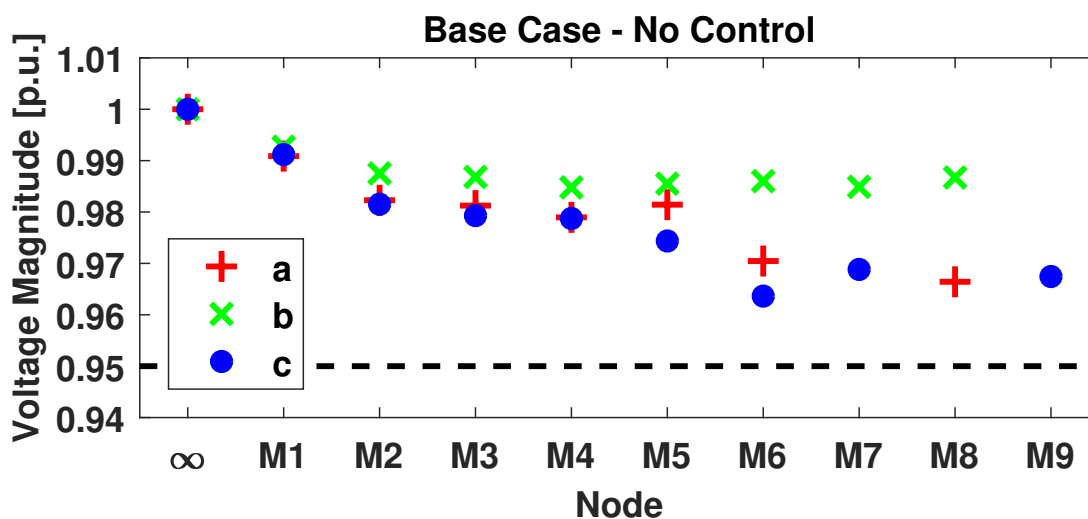


Figure 12.6: Base case (no control) of voltage balancing scenario for nine node mesh network.

Figure 12.6 gives the voltage magnitude for the base case (no control) of the voltage magnitude balancing experiment on the nine node mesh network. Significant imbalance can be seen in nodes $M6 - M8$, where voltage magnitudes differ by more than 1 p.u.

Figure 12.7 shows the power flow results, applying the optimal DER dispatch from (12.3). The decrease in voltage magnitude imbalance from the base case is clearly visible.

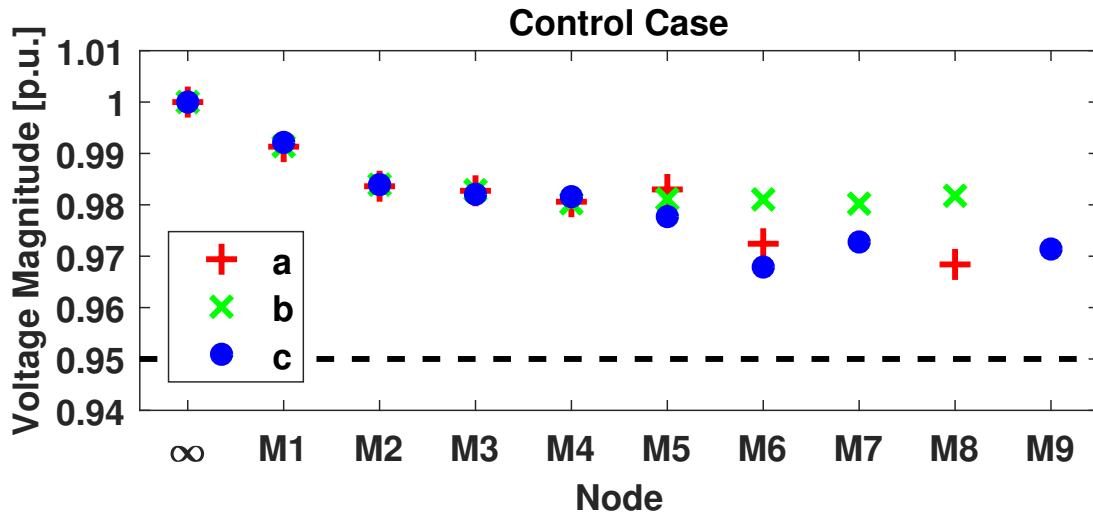


Figure 12.7: Control case of voltage balancing scenario for nine node mesh network, with DER dispatch from (12.3).

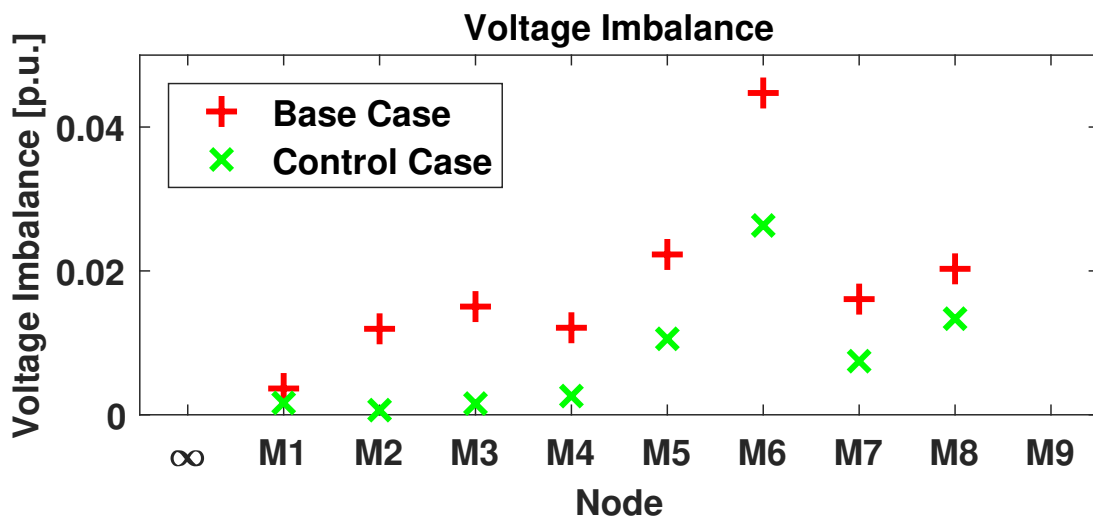


Figure 12.8: Comparison of voltage magnitude imbalance for nine node mesh network between base case and control case.

Figure 12.8 gives the voltage imbalance at each node. The total imbalance for the base case is 0.146, and the total imbalance for the control case is 0.064. Table 12.2 gives the optimal DER dispatch from 12.3.

Node	Phase a w_n^a	Phase b w_n^b	Phase c w_n^c
M2	-0.00721 - j0.00339	0.00294 + j0.00956	0.00088 - j0.00996
M3	-0.00837 - j0.00314	0.00315 + j0.00949	0
M4	0	0.00307 + j0.00952	0.00224 - j0.00975
M6	-0.00858 - j0.00513	0.00258 + j0.00966	-0.00079 - j0.00997
M7	-	0.00359 + j0.00933	-0.00048 - j0.00999

Table 12.2: Optimal DER dispatch for voltage magnitude balancing from (12.3).

Increasing OPF Accuracy Through Sequential Linear/Quadratic Programming

Sequential linear programming (SLP) or Sequential quadratic programming can be employed to increase the accuracy of OPFs. Algorithm 1 describes the process. Convergence of Algorithm 1 is not proven, but we provide observations.

When employing Algorithm 1, simulation results show convergence for almost all networks and scenarios when voltage angle is excluded from the LUPFM as a variable. When voltage angle is included in the LUPFM, 1 usually does not converge, with differences in \mathbf{X} and \mathbf{X}^* corresponding to voltage angle. This is likely due to the small angle approximation in the LUPFM.

12.2 Phasor Difference Minimization for Switching Operations

We now present results of two experiments in which the power, magnitude, and angle equations were incorporated into an OPF with the objective of minimizing the phasor difference between nodes at either end of an open switch (we will refer to this as phasor tracking), while regulating system voltage magnitudes to within acceptable limits. The OPF decision variables were DER real and reactive power injections at select nodes, which were capacity constrained (i.e. four-quadrant resources).

In these experiments, we considered closing the switch between two points on a network. To minimize arc flashing, sudden and large real or reactive power surges across the switch, disturbances to the network, and protection equipment damage, we desire to match the voltage phasors at the ends of the open switch. To this end, we proposed the following OPF to minimize the voltage phasor difference between one nodes k and l , while providing feeder

Algorithm 1 Sequential Quadratic Programming for Increasing OPF Accuracy

1. Solve base OPF (12.3) to obtain optimal network state \mathbf{X}^* and DER complex power dispatch \mathbf{W}^* .
 2. Solve power flow with current optimal DER dispatch \mathbf{W}^* , to obtain network state \mathbf{X} .
 3. Update linearized terms in LUPFM from \mathbf{X} .
 - 3.1 Replace (10.54) in (12.3) with (10.4) or (10.9) if first iteration. Update \mathbf{L}_{mn} , $(m, n) \in \mathcal{E}$ from \mathbf{X} .
 - 3.2 Replace (10.55) in (12.3) with (10.19) or (10.33) if first iteration. Update \mathbf{H}_{mn} , $(m, n) \in \mathcal{E}$ from \mathbf{X} .
 - 3.3 Update $\gamma_n^{\phi\psi}$, $n \in \mathcal{N}$ from \mathbf{X} in (10.19) or (10.33).
 - 3.4 Replace (10.57) in (12.3) with (10.43) or (10.50) if first iteration. Update $\gamma_n^{\phi\psi}$, $n \in \mathcal{N}$ from \mathbf{X} .
 - 3.5 Update (10.43) or (10.50), with e_m^ϕ , $\phi \in \mathcal{P}_m$, $m \in \mathcal{N}$ and e_n^ϕ , $\phi \in \mathcal{P}_n$, $n \in \mathcal{N}$ from \mathbf{X} .
 4. Solve updated OPF (12.3) to obtain new optimal network state \mathbf{X}^* and DER complex power dispatch \mathbf{W}^* .
 5. Solve power flow with current optimal DER dispatch \mathbf{W}^* , to obtain network state \mathbf{X} .
 6. Check for convergence of \mathbf{X} and \mathbf{X}^* .
 - 6.1 If convergence not achieved, repeat steps 3 - 6.
 - 6.2 If convergence achieved, stop.
-

voltage support:

$$\begin{aligned}
 & \underset{u_n^\phi, v_n^\phi, y_n^\phi, \theta_n^\phi, P_n^\phi, Q_n^\phi}{\text{minimize}} && \rho_E C_E + \rho_\theta C_\theta + \rho_w C_w \\
 & \text{subject to} && (10.53), (10.54), (10.55), (10.58), (10.56) \\
 & && \underline{E}_n^\phi \leq E_n^\phi \leq \overline{E}_n^\phi \quad \forall \phi \in \mathcal{P}_n, \forall n \in \mathcal{N}_1 \cup \mathcal{N}_2 \\
 & && |w_n^\phi| \leq \overline{w}_n^\phi \quad \forall \phi \in \mathcal{P}_n, \forall n \in \mathcal{N}_1 \cup \mathcal{N}_2,
 \end{aligned} \tag{12.4}$$

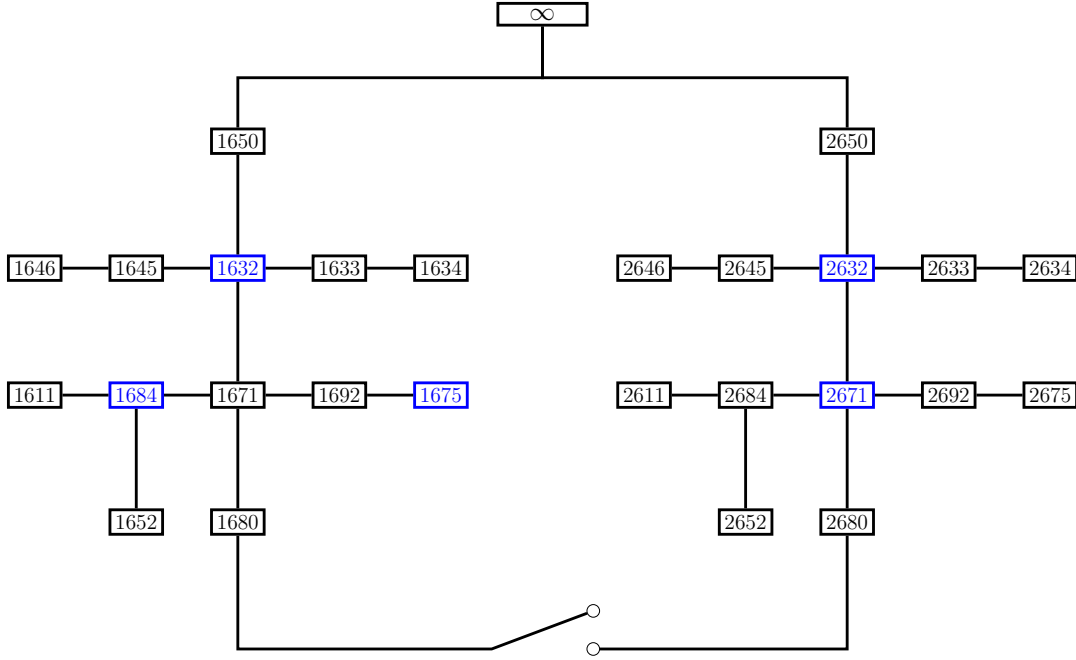


Figure 12.9: Networks \mathcal{N}_1 and \mathcal{N}_2 connected to the same transmission line, with open switch between nodes 1680 and 2680.

where

$$C_E = \sum_{\phi \in \mathcal{P}_{kl}} \left(E_k^\phi - E_l^\phi \right)^2, \quad (12.5)$$

$$C_\theta = \sum_{\phi \in \mathcal{P}_{kl}} \left(\theta_k^\phi - \theta_l^\phi \right)^2, \quad (12.6)$$

$$C_w = \sum_{n \in \mathcal{N}} \sum_{\phi \in \mathcal{P}_n} |w_n^\phi|^2. \quad (12.7)$$

The OPF objective function is a weighted sum of three terms: C_E is the sum of squared magnitude tracking error for all nodes and phases with an assigned magnitude reference, C_θ is the sum of squared angle tracking error for all nodes and phases with an assigned angle reference, and C_w is the sum of the squared magnitudes of all DER dispatch. Voltage magnitude bounds were $0.95 \leq |V_n^\phi| \leq 1.05$ such that $\underline{E}_n^\phi = 0.9025$ and $\overline{E}_n^\phi = 1.1025$. DER dispatch is constrained by its apparent power capacity.

In 12.4, the DER dispatch apparent power constraints, $|w_n^\phi| \leq \bar{w} \forall \phi \in \mathcal{P}_n, \forall n \in \mathcal{N}$ can be approximated by a series of linear equations as derived in Appendix C, such that (12.4) is a true quadratic program.

It should be noted that comparison of either case to an SDP formulation of (12.4) we were not able to obtain a rank-one solution to an equivalent problem formulated as an SDP for either scenario.

Phasor Difference Minimization on a Radial Network

The first experiment was conducted on two modified versions of the IEEE 13 node distribution test feeder model [18]. Feeder topology, line configuration, line impedance, line length, and spot loads are specified in [18] and outlined in Appendix A.2. We consider two networks, \mathcal{N}_1 and \mathcal{N}_2 , connected to the same transmission line as in Figure 12.9. For clarity, we concatenate the number 1 to the front of nodes within \mathcal{N}_1 and the number 2 for nodes within \mathcal{N}_2 (e.g. node 671 of \mathcal{N}_1 is now 1671 and node 634 of \mathcal{N}_2 is now 2634). The transmission line, indexed by ∞ and denoted in Figure 12.9 by ∞ , is treated as an infinite bus, with fixed voltage reference of $\mathbf{V}_\infty = \begin{bmatrix} 1 & 1\angle 240^\circ & 1\angle 120^\circ \end{bmatrix}^T$ p.u..

The first network, \mathcal{N}_1 , is a modified version of the IEEE 13 node test feeder model. The voltage regulator between nodes 1650 and 1632 is omitted, the transformer between nodes 1633 and 1634 is replaced by a line of configuration 601 and length of 50 feet, and the switch between node 1671 and 1692 is replaced by a line with configuration 601 and length of 50 feet. All loads are assumed to be Wye connected. We place Wye connected $0.01 + j0.004$ p.u. loads on all phases at node 1680. Capacitors in \mathcal{N}_1 were multiplied by a factor of 0.5. Four quadrant capable DER were placed at on all existing phases at nodes $\mathcal{G}_\infty = \{1632, 1675, 1684\}$. We assumed each DER can inject or sink both real and reactive power separately on each phase of the feeder. All DER were constrained by an apparent power capacity limit on each phase of 250 kVA, or 0.05 p.u.

The second network, \mathcal{N}_2 , is also a modified version of the IEEE 13 node test feeder model. The voltage regulator between nodes 2650 and 2632 is omitted, the transformer between nodes 2633 and 2634 is replaced by a line of configuration 601 and length of 50 feet, and the switch between node 2671 and 2692 is replaced by a line with configuration 601 and length of 50 feet. All loads are assumed to be Wye connected. We place Wye connected $0.01 + j0.004$ p.u. loads on all phases at node 2680. Capacitors in \mathcal{N}_1 were multiplied by a factor of 0.5. Four quadrant capable DER were placed at on all existing phases at nodes $\mathcal{G}_\infty = \{2632, 2671\}$. We assumed each DER can inject or sink both real and reactive power separately on each phase of the feeder. All DER were constrained by an apparent power capacity limit on each phase of 250 kVA, or 0.05 p.u.

Loads follow the voltage dependent load model of (8.8) with parameters $A_{PQ,n}^\phi = 0.85$ and $A_{Z,n}^\phi = 0.15 \forall \phi \in \{a, b, c\}, \forall n \in \mathcal{N}_1, \forall n \in \mathcal{N}_2$. To create a load imbalance between the two networks, we multiply all loads in \mathcal{N}_1 by a factor of 0.75 and all loads in \mathcal{N}_2 by a factor of 1.5. An open switch was placed between node $k = 1680$ of \mathcal{N}_1 and node $l = 2680$ of \mathcal{N}_2 , with a line with configuration 601 and length of 500 feet.

The weighting on the three components of the objective function of (12.4) are $\rho_E = 1000$, $\rho_\theta = 1000$, and $\rho_w = 1$. Results from this experiment can be seen in Table 12.3. We consider three cases: “No Control” (NC) where all DER dispatch is 0, “Magnitude Control” (MC) where the optimal DER dispatch is obtained solving (12.4) with $\rho_\theta = 0$, and “Phasor Control” (PC) where the optimal DER dispatch is obtained solving (12.4). For each case, power flow is solved with the zero (NC) or optimal DER dispatch from (12.4) (MC,PC). For

all cases, power flow is solved using a Newton-Raphson method adapted from [48], comprised of (8.4), (8.6), and (8.8).

It can clearly be seen that with MC, the difference in per phase magnitudes of 1680 and 2680 are driven toward zero, however the voltage angle difference still remains large and on the order of the NC case. With PC, both the voltage magnitude differences and phase angle differences are minimized.

The last row of Table 12.3 gives the hypothetical instantaneous complex power phasor should the switch be closed with the voltages at node 1680 and node 2680 listed in Table 12.3. We define this as:

$$\mathbf{S}_{mn}^\dagger = \mathbf{V}_n \circ [\mathbf{Y}_{mn} (\mathbf{V}_m - \mathbf{V}_n)]^* \quad , \quad (12.8)$$

where $m = 1680$, $n = 2680$, and \mathbf{Y}_{mn} is the admittance matrix of line (m, n) , defined as $\mathbf{Y}_{mn} = [\mathbf{Z}_{mn}]_{\mathcal{P}_{mn}, \mathcal{P}_{mn}}^{-1}$. It is important to note that this power is not the steady state value after the switch is closed, but rather the instantaneous power that would flow with the given instantaneous voltage difference and line admittance. While this power value will change and reach a steady state value over time, a transient analysis is outside the scope of this work. The optimal DER dispatch is given in Table 12.4.

Phasor Difference Minimization on a Mesh Network

We consider a second experiment on a meshed (cyclic) network, and use the mesh network from Section 12.1. Network topology can be seen in 12.5, and parameters are listed in Appendix A.3.

Loads follow the voltage dependent load model of (8.8) with parameters $A_{PQ,n}^\phi = 0.85$ and $A_{Z,n}^\phi = 0.15 \forall \phi \in \{a, b, c\}, \forall n \in \mathcal{N}$.

DER is placed at nodes $\mathcal{G} = \{M2, M3, M4, M6, M7\}$ with an apparent power capacity limit of 0.10 p.u. DER is assumed to be four quadrant operation capable single phase inverters. Voltage magnitude bounds were $0.95 \leq |V_n^\phi| \leq 1.05$ such that $\underline{E}_n^\phi = 0.9025$ and $\overline{E}_n^\phi = 1.1025$.

A switch is placed between nodes $M5$ and $M6$. The OPF (12.4) is employed with $k = M5$ and $l = M6$ to optimally dispatch DER to minimize the phasor difference, with objective function weights $\rho_E = 1000$, $\rho_\theta = 1000$, and $\rho_w = 1$.

Table 12.5 gives the results of this simulation, where we consider the three cases from the previous simulation. It can be seen that the voltage magnitude difference is greatly reduced for the ‘‘MC’’ case, however the hypothetical power $\left(S_{M5, M6}^\phi\right)^\dagger$ remains roughly as large as the ‘‘NC’’ case. When full phasor control ‘‘PC’’ is applied, both the magnitude difference and angle difference are minimized, and the hypothetical power real power is smaller than the ‘‘NC’’ and ‘‘MC’’ cases. Table 12.6 gives the DER dispatch from (12.4).

	Phase ϕ	No Control	Magnitude Control	Phasor Control
Node 1680 Voltage Phasor [p.u.] V_{1680}^ϕ	<i>a</i>	0.9829 \angle -1.6337	0.9685 \angle -1.8576	0.9686 \angle -2.6685
	<i>b</i>	0.9946 \angle -120.7197	0.9922 \angle -120.8156	0.9928 \angle -121.0663
	<i>c</i>	0.9715 \angle 118.7010	0.9512 \angle 118.9686	0.9506 \angle 117.8855
Node 2680 Voltage Phasor [p.u.] V_{2680}^ϕ	<i>a</i>	0.9619 \angle -3.3306	0.9673 \angle -3.1513	0.9684 \angle -2.6695
	<i>b</i>	0.9872 \angle -121.3947	0.9923 \angle -121.4730	0.9926 \angle -121.0704
	<i>c</i>	0.9350 \angle 117.4363	0.9501 \angle 117.3944	0.9504 \angle 117.8839
Magnitude Difference [p.u.] $ V_{1680}^\phi - V_{2680}^\phi $	<i>a</i>	0.0211	0.0012	0.0002
	<i>b</i>	0.0074	-0.0001	0.0002
	<i>c</i>	0.0365	0.0011	0.0003
Angle Difference [°] $\theta_{1680}^\phi - \theta_{2680}^\phi$	<i>a</i>	1.6969	1.2937	0.0010
	<i>b</i>	0.6751	0.6574	0.0041
	<i>c</i>	1.2648	1.5742	0.0016
Hypothetical Power [p.u.] $(S_{1680,2680}^\phi)^\dagger$	<i>a</i>	1.6423 + j0.8614	1.2447 + j-0.2292	0.0055 + j0.0108
	<i>b</i>	1.1633 + j0.7256	0.8762 + j-0.1223	0.0058 + j0.0108
	<i>c</i>	1.6301 + j1.0542	1.1868 + j-0.4280	0.0057 + j0.0115

Table 12.3: Results of phasor matching for switching action simulation showing comparison between no control, magnitude only control, and phasor control.

Node	Phase A	Phase B	Phase C
1632	$0.0312 + j0.0189$	$0.0329 + j0.0197$	$0.0383 + j0.0214$
1675	$0.0433 + j0.0251$	$0.0436 + j0.0244$	$0.0440 + j0.0238$
1684	$0.0431 + j0.0253$	0	$0.0441 + j0.0236$
2632	$-0.0349 + j-0.0139$	$-0.0273 + j-0.0188$	$-0.0378 + j-0.0328$
2671	$-0.0472 + j-0.0166$	$-0.0419 + j-0.0273$	$-0.0381 + j-0.0324$

Table 12.4: Optimal DER dispatch for phasor matching for switching action from (12.4).

	Phase ϕ	No Control	Magnitude Control	Phasor Control
Node M5 Voltage Phasor [p.u.] V_{1680}^ϕ	<i>a</i>	0.9814 \angle -0.9993	0.9838 \angle -0.7946	0.9816 \angle -1.6856
	<i>b</i>	0.9855 \angle -120.9524	0.9804 \angle -120.8273	0.9968 \angle -120.4100
	<i>c</i>	0.9744 \angle 118.4329	0.9902 \angle 118.4258	0.9629 \angle 119.2720
Node M6 Voltage Phasor [p.u.] V_{2680}^ϕ	<i>a</i>	0.9705 \angle -1.2197	0.9792 \angle -1.1027	0.9762 \angle -1.7256
	<i>b</i>	0.9860 \angle -121.3005	0.9795 \angle -120.8356	0.9941 \angle -120.4713
	<i>c</i>	0.9636 \angle 117.7875	0.9882 \angle 117.8604	0.9517 \angle 119.1503
Magnitude Difference [p.u.] $ V_{M5}^\phi - V_{M6}^\phi $	<i>a</i>	0.0110	0.0046	0.0054
	<i>b</i>	-0.0005	0.0009	0.0027
	<i>c</i>	0.0107	0.0021	0.0112
Angle Difference [$^\circ$] $\theta_{M5}^\phi - \theta_{M6}^\phi$	<i>a</i>	0.2205	0.3081	0.0400
	<i>b</i>	0.3481	0.0083	0.0613
	<i>c</i>	0.6454	0.5654	0.1217
Hypothetical Power [p.u.] $(S_{M5,M6}^\phi)^\dagger$	<i>a</i>	0.3481 + j0.5246	0.3951 + j0.2329	0.0867 + j0.3426
	<i>b</i>	0.3137 + j0.0311	0.0925 + j0.0769	0.1405 + j0.2062
	<i>c</i>	0.7499 + j0.3251	0.4886 + j-0.0797	0.2669 + j0.4495

Table 12.5: Results of phasor matching for switching action simulation showing comparison between no control, magnitude only control, and phasor control.

Node	Phase A	Phase B	Phase C
M2	$0.0995 + j-0.0099$	$-0.0959 + j-0.0284$	$0.0224 + j0.0975$
M3	$0.0995 + j0.0102$	$0.0968 + j-0.0250$	0
M4	0	$-0.0974 + j0.0228$	$0.0996 + j-0.0091$
M6	$-0.0934 + j-0.0357$	$-0.0829 + j0.0559$	$-0.0945 + j0.0326$
M7	0	$0.0216 + j-0.0976$	$-0.0941 + j0.0338$

Table 12.6: Optimal DER dispatch for phasor matching for switching action from (12.4).

Chapter 13

Concluding Remarks and Future Work

Optimization of energy resources on unbalanced networks is a challenging field due to the nonlinear and nonconvex physics of power flow. Many works have studied how to address these issues using semidefinite programming and approximate linear models.

In this work, we our aim was to investigate solving OPF problems that cannot be addressed with SDP techniques. We extend the work of [14, 20, 39] by developing a linearized model for unbalanced power flow in Section 10.4. This model maps voltage angle differences across a line to the complex power flow on the line.

In Chapter 11, We investigated the accuracy of the LUPFM, comparing the results of solving power flow with the system physics and the LUPFM. We found that under normal operating conditions, the model leads to magnitude errors on the order of 1%, angle errors of less than 0.5 and substation power errors of 5% of the network rated power.

In Chapter 12, we study two applications of the LUPFM. The first application is to minimize the difference in voltage magnitude across different phases at nodes in a distribution network. Simulation results prove the OPF effective in this endeavor.

The second application is to minimize the voltage phasor difference between two nodes, representing an open switch. We design an OPF that seeks to minimize the voltage magnitude difference per phase at two nodes, and the voltage angle difference per phase at two nodes. Simulation results demonstrate the efficacy of the OPF in minimizing voltage phasor difference.

The ability to switch components into and out of distribution feeders with minimal impact on system operation presents many opportunities to reconfigure distribution systems for a variety of purposes. Moving forward, we intend to investigate two such applications. First, we plan to study grid reconfiguration in order to better withstand critical grid events (e.g. weather-related or other types of disasters). In anticipation of a critical event, it may be advantageous to alter system topology to maximize the ability to serve critical loads. To solve such a problem, we will most likely need to extend our present OPF formulation into a receding horizon controller, that can optimize over a future time window. Secondly, as

“clean” switching may also enable distributed microgrids to coalesce and pool resources to provide ancillary services, we intend to extend this OPF formulation to allow for mixed-integer formulations.

Chapter 14

Conclusion

14.1 Modeling and Optimal Control of Commercial Office Plug Loads and Battery Storage Systems

This dissertation developed an approach for control of commercial office OSBS alongside plug loads.

Summary of Results

This work focused on two main aspects: development of a model for an off the shelf OSBS for incorporation into an MPC, and solving the nonlinear and nonconvex MPC. A model predictive control formulation was augmented to include generic battery storage for demand response of load following. A model of an off the shelf OSBS was derived from experimental data. Two algorithms for solving the nonlinear MPC were derived and discussed.

An exhaustive search algorithm that optimizes plug load control over all possible battery control sequences was derived. Simulations with this algorithm highlight the severe faults of short prediction horizon and necessity of long timesteps.

A dynamic programming algorithm was then implemented. Simulation results show the promise of this method, and highlight positive attributes such as long prediction window and good timestep granularity. Simulation results also provide insight into the benefit of an OSBS with controllable charging.

Future Work

While the research in this work provided methods for control of plug loads and an OSBS, more work is needed before such work can be practically implemented. One key area is the development of an algorithm for optimal OSBS control for OSBS systems.

14.2 Modeling of Unbalanced Power Flow and Optimal Control of Distributed Energy Resources for Grid Reconfiguration

This dissertation focused on approaches for controlling voltage magnitude and phase angle on an unbalanced distribution network.

Summary of Results

First semidefinite programming is discussed as a method for solving nonlinear and non-convex OPFs. Literature points to many successes, but also bring to light many drawbacks and attributes of SDP that may preclude its widespread implementation. We then derive several SDP OPFs for control of voltage magnitude and angle. Simulations motivate further analysis into the control of voltage magnitude, and also show success in constraining voltage angle.

A linearized unbalanced power flow model (LUPFM) is derived for incorporation into convex OPFs. This model augments those of [14, 39] by adding a relationship between voltage angle difference across a network line and complex power flow on the line. The accuracy of the LUPFM is investigated and found to be satisfactory for IEEE benchmark unbalanced networks.

Two application of the LUPFM are discussed. The first is an OPF that seeks to minimize voltage magnitude imbalance at nodes on an unbalanced network. Simulation results for both radial and mesh networks show the success of this OPF.

The second is an OPF that seeks to minimize voltage phasor difference between two unconnected nodes for switching actions. Simulations for both radial and mesh networks are successful in reducing the phasor difference.

Future Work

There are many key areas in which the LUPFM can improve distribution network operation. An example is to incorporate the LUPFM into an MPC for voltage phasor regulation across changing loads and distributed generation and storage conditions.

There are also many ways in which the LUPFM can be improved itself. Development of more accurate inverter models is a necessary task. Development of additional operational network constraints for the LUPFM is also necessary. Finally, a more thorough investigation into sequential linear programming would likely prove beneficial.

Bibliography

- [1] D. B. Arnold et al. “Model-Free Optimal Coordination of Distributed Energy Resources for Provisioning Transmission-Level Services”. In: *IEEE Transactions on Power Systems* PP.99 (2017), pp. 1–1. ISSN: 0885-8950. DOI: 10.1109/TPWRS.2017.2707405.
- [2] Daniel B Arnold, Michael D Sankur, and David M Auslander. “An energy information gateway for use in residential and commercial environments”. In: *Power and Energy Society General Meeting (PES), 2012 IEEE*. IEEE. 2012, pp. 1–5.
- [3] Daniel B Arnold, Michael D Sankur, and David M Auslander. “Optimal Control of Office Plug-loads for Commercial Building Demand Response”. In: *ASME 2013 Dynamic Systems and Control Conference*. American Society of Mechanical Engineers. 2013, V001T13A001–V001T13A001.
- [4] Daniel B Arnold, Michael D Sankur, and David M Auslander. “The next generation energy information gateway for use in residential and commercial environments”. In: *Power and Energy Society General Meeting (PES), 2013 IEEE*. IEEE. 2013, pp. 1–5.
- [5] Daniel B Arnold et al. “Model-Free Optimal Control of VAR Resources in Distribution Systems: An Extremum Seeking Approach”. In: *IEEE Transactions on Power Systems* PP (99 2015), pp. 1–11.
- [6] Daniel B Arnold et al. “Optimal dispatch of reactive power for voltage regulation and balancing in unbalanced distribution systems”. In: *IEEE Power and Energy Society General Meeting, accepted* (2016).
- [7] Xiaoqing Bai et al. “Semidefinite programming for optimal power flow problems”. In: *International Journal of Electrical Power & Energy Systems* 30.6 (2008), pp. 383–392.
- [8] Mesut E Baran and Felix F Wu. “Network reconfiguration in distribution systems for loss reduction and load balancing”. In: *IEEE Transactions on Power delivery* 4.2 (1989), pp. 1401–1407.
- [9] Mesut E Baran and Felix F Wu. “Optimal sizing of capacitors placed on a radial distribution system”. In: *IEEE Transactions on Power Delivery* 4.1 (1989), pp. 735–743.
- [10] Saverio Bolognani and Florian Dörfler. “Fast power system analysis via implicit linearization of the power flow manifold”. In: *Communication, Control, and Computing (Allerton), 2015 53rd Annual Allerton Conference on*. IEEE. 2015, pp. 402–409.

- [11] Emiliano Dall’Anese, Hao Zhu, and Georgios Giannakis. “Distributed optimal power flow for smart microgrids”. In: *Smart Grid, IEEE Transactions on* 4.3 (2013), pp. 1464–1475.
- [12] Masoud Farivar, Lijun Chen, and Steven Low. “Equilibrium and dynamics of local voltage control in distribution systems”. In: *Decision and Control (CDC), 2013 IEEE 52nd Annual Conference on*. IEEE. 2013, pp. 4329–4334.
- [13] John Franco, Luis Ochoa, and Ruben Romero. “AC OPF for Smart Distribution Networks: An Efficient and Robust Quadratic Approach”. In: *IEEE Transactions on Smart Grid* (2017).
- [14] Lingwen Gan and Steven H Low. “Convex relaxations and linear approximation for optimal power flow in multiphase radial networks”. In: *Power Systems Computation Conference (PSCC), 2014*. IEEE. 2014, pp. 1–9.
- [15] *Grid Modernization Multi-Year Program Plan*. <http://energy.gov/sites/prod/files/2016/01/f28/Grid%20Modernization%20Multi-Year%20Program%20Plan.pdf>.
- [16] Gerald Thomas Heydt. “The next generation of power distribution systems”. In: *IEEE Transactions on Smart Grid* 1.3 (2010), pp. 225–235.
- [17] Longbo Huang, Jean Walrand, and Kannan Ramchandran. “Optimal demand response with energy storage management”. In: *Smart Grid Communications (Smart-GridComm), 2012 IEEE Third International Conference on*. IEEE. 2012, pp. 61–66.
- [18] *IEEE Distribution Test Feeders*. <http://ewh.ieee.org/soc/pes/dsacom/testfeeders/index.html>. Online; accessed May-2015.
- [19] David Kaneda et al. “Plug load reduction: The next big hurdle for net zero energy building design”. In: *published in the ACEEE Summer Study on Energy Efficient Buildings* (2010), pp. 9–120.
- [20] Vassilis Kekatos et al. “Voltage regulation algorithms for multiphase power distribution grids”. In: *IEEE Transactions on Power Systems* 31.5 (2016), pp. 3913–3923.
- [21] Iordanis Koutsopoulos, Vassiliki Hatzi, and Leandros Tassiulas. “Optimal energy storage control policies for the smart power grid”. In: *Smart Grid Communications (Smart-GridComm), 2011 IEEE International Conference on*. IEEE. 2011, pp. 475–480.
- [22] Javad Lavaei and Steven H Low. “Zero duality gap in optimal power flow problem”. In: *IEEE Transactions on Power Systems* 27.1 (2012), pp. 92–107.
- [23] Javad Lavaei, David Tse, and Baosen Zhang. “Geometry of power flows and optimization in distribution networks”. In: *IEEE Transactions on Power Systems* 29.2 (2014), pp. 572–583.
- [24] Bernard C Lesieutre et al. “Examining the limits of the application of semidefinite programming to power flow problems”. In: *Communication, Control, and Computing (Allerton), 2011 49th Annual Allerton Conference on*. IEEE. 2011, pp. 1492–1499.

- [25] Na Li, Guannan Qu, and Munther Dahleh. “Real-time decentralized voltage control in distribution networks”. In: *Communication, Control, and Computing (Allerton), 2014 52nd Annual Allerton Conference on*. IEEE. 2014, pp. 582–588.
- [26] Raphael Louca, Peter Seiler, and Eilyan Bitar. “A rank minimization algorithm to enhance semidefinite relaxations of optimal power flow”. In: *Communication, Control, and Computing (Allerton), 2013 51st Annual Allerton Conference on*. IEEE. 2013, pp. 1010–1020.
- [27] Raphael Louca, Peter Seiler, and Eilyan Bitar. “Nondegeneracy and inexactness of semidefinite relaxations of optimal power flow”. In: *arXiv preprint arXiv:1411.4663* (2014).
- [28] Zhi-Quan Luo et al. “Semidefinite relaxation of quadratic optimization problems”. In: *IEEE Signal Processing Magazine* 27.3 (2010), pp. 20–34.
- [29] Ramtin Madani, Somayeh Sojoudi, and Javad Lavaei. “Convex relaxation for optimal power flow problem: Mesh networks”. In: *IEEE Transactions on Power Systems* 30.1 (2015), pp. 199–211.
- [30] A. von Meier et al. “Micro-synchrophasors for distribution systems”. In: *ISGT 2014*. Feb. 2014, pp. 1–5. DOI: 10.1109/ISGT.2014.6816509.
- [31] Daniel K Molzahn, Sina S Baghsorkhi, and Ian A Hiskens. “Semidefinite relaxations of equivalent optimal power flow problems: An illustrative example”. In: *Circuits and Systems (ISCAS), 2015 IEEE International Symposium on*. IEEE. 2015, pp. 1887–1890.
- [32] Daniel K Molzahn and Ian A Hiskens. “Convex relaxations of optimal power flow problems: An illustrative example”. In: *IEEE Transactions on Circuits and Systems I: Regular Papers* 63.5 (2016), pp. 650–660.
- [33] Daniel K Molzahn et al. “Implementation of a large-scale optimal power flow solver based on semidefinite programming”. In: *IEEE Transactions on Power Systems* 28.4 (2013), pp. 3987–3998.
- [34] Nathan Murthy. “Energy-agile laptops: Demand response of mobile plug loads using sensor/actuator networks”. In: *Smart Grid Communications (SmartGridComm), 2012 IEEE Third International Conference on*. IEEE. 2012, pp. 581–586.
- [35] Luis F Ochoa and Douglas H Wilson. “Angle constraint active management of distribution networks with wind power”. In: *Innovative Smart Grid Technologies Conference Europe (ISGT Europe), 2010 IEEE PES*. IEEE. 2010, pp. 1–5.
- [36] Frauke Oldewurtel et al. “Reducing peak electricity demand in building climate control using real-time pricing and model predictive control”. In: *Decision and Control (CDC), 2010 49th IEEE Conference on*. IEEE. 2010, pp. 1927–1932.
- [37] *Quadrennial Energy Review: First Installment*. url<http://energy.gov/epa/downloads/quadrennial-energy-review-first-installment>. Online; April-2015.

- [38] He Renmu, Ma Jin, and David J Hill. “Composite load modeling via measurement approach”. In: *IEEE Transactions on Power Systems* 21.2 (2006), pp. 663–672.
- [39] Brett A Robbins and Alejandro D Domínguez-García. “Optimal reactive power dispatch for voltage regulation in unbalanced distribution systems”. In: *IEEE Transactions on Power Systems* 31.4 (2016), pp. 2903–2913.
- [40] Michael D Sankur, Daniel B Arnold, and David Auslander. “An architecture for integrated commercial building demand response”. In: *Power and Energy Society General Meeting (PES), 2013 IEEE*. IEEE. 2013, pp. 1–5.
- [41] Michael D Sankur, Daniel B Arnold, and David M Auslander. “Dynamic Programming for Optimal Load-Shedding of Office Scale Battery Storage and Plug-Loads”. In: *Power and Energy Society General Meeting (PES), 2015 IEEE*. IEEE. 2015.
- [42] Michael D Sankur, Daniel B Arnold, and David M Auslander. “Model Predictive Control of Commercial Office Plug-Loads and Battery Storage Systems”. In: *ASME 2014 Dynamic Systems and Control Conference*. American Society of Mechanical Engineers. 2014, V001T07A001–V001T07A001.
- [43] E M Stewart et al. *Analysis of High-Penetration Levels of Photovoltaics into the Distribution Grid on Oahu, Hawaii, Detailed Analysis of HECO Feeder WF1*. Tech. rep. NREL subcontract report NREL/SR-5500-54494, 2013.
- [44] *Synchrophasor Fact Sheet*. https://cdn.selinc.com/assets/Literature/Product/%20Literature/Flyers/FS_Synchrophasor_BF_20100617.pdf?v=20150408-131001. Online; June-2010.
- [45] Energy Information Administration (US). *Annual Energy Review 2011*. Government Printing Office, 2012.
- [46] Peter Van de Ven et al. “Optimal control of residential energy storage under price fluctuations”. In: *ENERGY 2011, The First International Conference on Smart Grids, Green Communications and IT Energy-aware Technologies*. 2011, pp. 159–162.
- [47] Dongping Wang et al. “PMU-based angle constraint active management on 33kV distribution network”. In: *Electricity Distribution (CIRED 2013), 22nd International Conference and Exhibition on*. IET. 2013, pp. 1–4.
- [48] RG Wasley and MA Shlash. “Newton-Raphson algorithm for 3-phase load flow”. In: *Proceedings of the Institution of Electrical Engineers*. Vol. 121. 7. IET. 1974, pp. 630–638.
- [49] Thomas Weng et al. “Managing plug-loads for demand response within buildings”. In: *Proceedings of the Third ACM Workshop on Embedded Sensing Systems for Energy-Efficiency in Buildings*. ACM. 2011, pp. 13–18.
- [50] Ahmed S Zamzam, Nicholas D Sidiropoulos, and Emiliano Dall’Anese. “Beyond relaxation and Newton-Raphson: Solving AC OPF for multi-phase systems with renewables”. In: *IEEE Transactions on Smart Grid* (2016).

- [51] Baosen Zhang et al. “Optimal distributed voltage regulation in power distribution networks”. In: *Cornell University Library Web Page*. Available online: <http://arxiv.org/abs/1204.5226v1> (accessed on 23 April 2012) (2012).

Appendix A

Distribution Network Parameters

A.1 Parameters of the Five Node Network

This appendix will outline the parameters of the five node meshed network as used in simulations in Chapter 9. The topology can be seen in Figure 9.1.

Node	∞	A1	A2	A3	A4	A5
\mathcal{P}_m	$\{a\}$	$\{a\}$	$\{a\}$	$\{a\}$	$\{a\}$	$\{a\}$

Table A.1: Five node network nodes parameters.

Node m	Node n	\mathcal{P}_{mn}	$100 \times [\mathbf{Z}_{mn}]_{\mathcal{P}_{mn}}$ [p.u.]
∞	A1	$\{a\}$	$0.3281 + j0.9639$
A1	A2	$\{a\}$	$1.3125 + j3.8557$
A2	A3	$\{a\}$	$0.9844 + j2.8918$
A2	A4	$\{a\}$	$0.9844 + j2.8918$
A4	A5	$\{a\}$	$0.9844 + j2.8918$

Table A.2: Five node network line nodes, phases and impedances.

Node	Phase a d_n^a	Phase b d_n^b	Phase c d_n^c
A2	$0.1000 + j0.0800$	-	-
A3	$0.1000 + j0.1000$	-	-
A4	$0.0600 + j0.0800$	-	-
A5	$0.0600 + j0.0400$	-	-

Table A.3: Per-unit complex demands at nodes for nine node network

Node	Phase a c_n^a	Phase b c_n^b	Phase c c_n^c
A5	$j0.0400$	-	-

Table A.4: Per-unit capacitance at nodes for nine node network

Node	Phase a \bar{w}_n^a	Phase b \bar{w}_n^b	Phase c \bar{w}_n^c
A2	0.1000	-	-
A3	0.1000	-	-
A5	0.1000	-	-

Table A.5: Per-unit apparent power capacity for DER placed nine node network.

A.2 Parameters of the IEEE 13 Node Test Feeder

This appendix will outline the parameters of the IEEE 13 node test feeder as used in simulations in Chapter 11 and Chapter 12. The topology can be seen in Figure 11.1.

Node	∞	650	632	633	634	645	646
\mathcal{P}_m	$\{a, b, c\}$	$\{a, b, c\}$	$\{a, b, c\}$	$\{a, b, c\}$	$\{a, b, c\}$	$\{b, c\}$	$\{b, c\}$
Node	671	692	675	680	684	652	611
\mathcal{P}_m	$\{a, b, c\}$	$\{a, b, c\}$	$\{a, b, c\}$	$\{a, b, c\}$	$\{a, c\}$	$\{a\}$	$\{c\}$

Table A.6: IEEE 13 node test network nodes parameters from [18].

Node m	Node n	\mathcal{P}_{mn}	$100 \times [\mathbf{Z}_{mn}]_{\mathcal{P}_{mn}}$ [p.u.]
∞	650	$\{a, b, c\}$	$\begin{bmatrix} 0.2889 + j2.3114 & 0.0722 + j0.1445 & 0.0722 + j0.1445 \\ 0.0722 + j0.1445 & 0.2889 + j2.3114 & 0.0722 + j0.1445 \\ 0.0722 + j0.1445 & 0.0722 + j0.1445 & 0.2889 + j2.3114 \end{bmatrix}$
650	632	$\{a, b, c\}$	$\begin{bmatrix} 3.7921 + j11.1400 & 1.7073 + j5.4907 & 1.7292 + j4.6359 \\ 1.7073 + j5.4907 & 3.6936 + j11.4672 & 1.6799 + j4.2124 \\ 1.7292 + j4.6359 & 1.6799 + j4.2124 & 3.7363 + j11.3250 \end{bmatrix}$
632	633	$\{a, b, c\}$	$\begin{bmatrix} 2.0591 + j3.2323 & 0.4323 + j1.1590 & 0.4268 + j1.3727 \\ 0.4323 + j1.1590 & 2.0452 + j3.2786 & 0.4200 + j1.0531 \\ 0.4268 + j1.3727 & 0.4200 + j1.0531 & 2.0345 + j3.3139 \end{bmatrix}$
633	634	$\{a, b, c\}$	$\begin{bmatrix} 0.0948 + j0.2785 & 0.0427 + j0.1373 & 0.0432 + j0.1159 \\ 0.0427 + j0.1373 & 0.0923 + j0.2867 & 0.0420 + j0.1053 \\ 0.0432 + j0.1159 & 0.0420 + j0.1053 & 0.0934 + j0.2831 \end{bmatrix}$
632	645	$\{b, c\}$	$\begin{bmatrix} 3.6373 + j3.6857 & 0.5653 + j1.2561 \\ 0.5653 + j1.2561 & 3.6220 + j3.7125 \end{bmatrix}$
645	646	$\{b, c\}$	$\begin{bmatrix} 2.1824 + j2.2114 & 0.3392 + j0.7537 \\ 0.3392 + j0.7537 & 2.1732 + j2.2275 \end{bmatrix}$
632	671	$\{a, b, c\}$	$\begin{bmatrix} 3.7921 + j11.1400 & 1.7073 + j5.4907 & 1.7292 + j4.6359 \\ 1.7073 + j5.4907 & 3.6936 + j11.4672 & 1.6799 + j4.2124 \\ 1.7292 + j4.6359 & 1.6799 + j4.2124 & 3.7363 + j11.3250 \end{bmatrix}$
671	692	$\{a, b, c\}$	$\begin{bmatrix} 0.0948 + j0.2785 & 0.0427 + j0.1373 & 0.0432 + j0.1159 \\ 0.0427 + j0.1373 & 0.0923 + j0.2867 & 0.0420 + j0.1053 \\ 0.0432 + j0.1159 & 0.0420 + j0.1053 & 0.0934 + j0.2831 \end{bmatrix}$

692	675	$\{a, b, c\}$	$2.1839 + j1.2211$	$0.8733 + j0.0897$	$0.7795 - j0.0391$
			$0.8733 + j0.0897$	$2.1590 + j1.1056$	$0.8733 + j0.0897$
			$0.7795 - j0.0391$	$0.8733 + j0.0897$	$2.1839 + j1.2211$
671	680	$\{a, b, c\}$	$1.8961 + j5.5700$	$0.8536 + j2.7453$	$0.8646 + j2.3180$
			$0.8536 + j2.7453$	$1.8468 + j5.7336$	$0.8400 + j2.1062$
			$0.8646 + j2.3180$	$0.8400 + j2.1062$	$1.8682 + j5.6625$
671	684	$\{a, c\}$	$2.1732 + j2.2423$	$0.3392 + j0.7537$	
			$0.3392 + j0.7537$	$2.1824 + j2.2114$	
684	652	$\{a\}$		$5.8770 + j2.2431$	
684	611	$\{c\}$		$2.1820 + j2.2121$	

Table A.7: IEEE 13 node test network line nodes, phases and per-unit impedances (multiplied by a factor of 100) from [18].

Node	Phase a d_n^a	Phase b d_n^b	Phase c d_n^c
634	$0.0320 + j0.0220$	$0.0240 + j0.0180$	$0.0240 + j0.0180$
645	-	$0.0340 + j0.0250$	0
646	-	$0.0460 + j0.0264$	0
671	$0.0770 + j0.0440$	$0.0770 + j0.0440$	$0.0770 + j0.0440$
692	0	0	$0.0340 + j0.0302$
675	$0.0970 + j0.0380$	$0.0136 + j0.0120$	$0.0580 + j0.0424$
680	$0.0020 + j0.0010$	$0.0020 + j0.0010$	$0.0020 + j0.0010$
652	$0.0256 + j0.0172$	-	-
611	-	-	$0.0340 + j0.0160$

Table A.8: Per-unit complex demands at nodes for IEEE 13 node feeder model from [18].

Node	Phase a c_n^a	Phase b c_n^b	Phase c c_n^c
675	$j0.0400$	$j0.0400$	$j0.0400$
611	-	-	$j0.0200$

Table A.9: Per-unit capacitance at nodes for IEEE 13 node feeder from [18].

Node	Phase a \bar{w}_n^a	Phase b \bar{w}_n^b	Phase c \bar{w}_n^c
632	0.0250	0.0250	0.0250
675	0.0250	0.0250	0.0250
680	0.0250	0.0250	0.0250
684	0.0250	-	0.0250

Table A.10: Per-unit apparent power capacity for DER placed on IEEE 13 node feeder.

A.3 Parameters of the Nine Node Meshed Network

This appendix will outline the parameters of the nine node meshed network as used in simulations in Chapter 12. The topology can be seen in Figure 12.5.

Node	∞	M1	M2	M3	M4
\mathcal{P}_m	$\{a, b, c\}$	$\{a, b, c\}$	$\{a, b, c\}$	$\{a, b, c\}$	$\{a, b, c\}$
Node	M5	M6	M7	M8	M9
\mathcal{P}_m	$\{a, b, c\}$	$\{a, b, c\}$	$\{b, c\}$	$\{a, b\}$	$\{c\}$

Table A.11: Nine node mesh network nodes parameters.

Node m	Node n	\mathcal{P}_{mn}	$100 \times [\mathbf{Z}_{mn}]_{\mathcal{P}_{mn}}$ [p.u.]
∞	M1	$\{a, b, c\}$	$\begin{bmatrix} 0.2889 + j2.3114 & 0.0722 + j0.1445 & 0.0722 + j0.1445 \\ 0.0722 + j0.1445 & 0.2889 + j2.3114 & 0.0722 + j0.1445 \\ 0.0722 + j0.1445 & 0.0722 + j0.1445 & 0.2889 + j2.3114 \end{bmatrix}$
M1	M2	$\{a, b, c\}$	$\begin{bmatrix} 0.9331 + j2.7411 & 0.4201 + j1.3510 & 0.4255 + j1.1407 \\ 0.4201 + j1.3510 & 0.9089 + j2.8217 & 0.4134 + j1.0365 \\ 0.4255 + j1.1407 & 0.4134 + j1.0365 & 0.9194 + j2.7867 \end{bmatrix}$
M2	M3	$\{a, b, c\}$	$\begin{bmatrix} 0.9331 + j2.7411 & 0.4201 + j1.3510 & 0.4255 + j1.1407 \\ 0.4201 + j1.3510 & 0.9089 + j2.8217 & 0.4134 + j1.0365 \\ 0.4255 + j1.1407 & 0.4134 + j1.0365 & 0.9194 + j2.7867 \end{bmatrix}$
M2	M3	$\{a, b, c\}$	$\begin{bmatrix} 0.9331 + j2.7411 & 0.4201 + j1.3510 & 0.4255 + j1.1407 \\ 0.4201 + j1.3510 & 0.9089 + j2.8217 & 0.4134 + j1.0365 \\ 0.4255 + j1.1407 & 0.4134 + j1.0365 & 0.9194 + j2.7867 \end{bmatrix}$
M2	M4	$\{a, b, c\}$	$\begin{bmatrix} 0.9331 + j2.7411 & 0.4201 + j1.3510 & 0.4255 + j1.1407 \\ 0.4201 + j1.3510 & 0.9089 + j2.8217 & 0.4134 + j1.0365 \\ 0.4255 + j1.1407 & 0.4134 + j1.0365 & 0.9194 + j2.7867 \end{bmatrix}$
M3	M5	$\{a, b, c\}$	$\begin{bmatrix} 0.9331 + j2.7411 & 0.4201 + j1.3510 & 0.4255 + j1.1407 \\ 0.4201 + j1.3510 & 0.9089 + j2.8217 & 0.4134 + j1.0365 \\ 0.4255 + j1.1407 & 0.4134 + j1.0365 & 0.9194 + j2.7867 \end{bmatrix}$
M4	M5	$\{a, b\}$	$\begin{bmatrix} 0.9331 + j2.7411 & 0.4201 + j1.3510 \\ 0.4201 + j1.3510 & 0.9089 + j2.8217 \end{bmatrix}$
M4	M6	$\{a, b\}$	$\begin{bmatrix} 0.9331 + j2.7411 & 0.4201 + j1.3510 \\ 0.4201 + j1.3510 & 0.9089 + j2.8217 \end{bmatrix}$

M5	M7	$\{b, c\}$	$0.9089 + j2.8217$	$0.4134 + j1.0365$	
M4	M7	$\{b\}$	$0.4134 + j1.0365$	$0.9194 + j2.7867$	
M6	M7	$\{c\}$	$0.9089 + j2.8217$		
M6	M8	$\{a, b\}$	$0.9331 + j2.7411$	$0.4201 + j1.3510$	
M7	M9	$\{c\}$	$0.4201 + j1.3510$	$0.9089 + j2.8217$	
			$0.9194 + j2.7867$		

Table A.12: Nine node mesh network line nodes, phases and impedances.

Node	Phase a d_n^a	Phase b d_n^b	Phase c d_n^c
M2	$0.1600 + j0.1100$	$0.1200 + j0.0900$	$0.1200 + j0.0900$
M3	$0.0700 + j0.0500$	$0.0500 + j0.0250$	0
M4	0	$0.1600 + j0.1100$	$0.1600 + j0.1100$
M6	$0.1600 + j0.1100$	$0.0680 + j0.0600$	$0.2000 + j0.1250$
M8	$0.1000 + j0.1000$	$0.0500 + j0.0200$	-
M9	-	-	$0.0800 + j0.0320$

Table A.13: Per-unit complex demands at nodes for nine node mesh network

Node	Phase a c_n^a	Phase b c_n^b	Phase c c_n^c
M6	$j0.0100$	$j0.0100$	$j0.0100$
M7	-	$j0.0100$	$j0.0100$
M9	-	-	$j0.0100$

Table A.14: Per-unit capacitance at nodes for nine node mesh network

Node	Phase a \bar{w}_n^a	Phase b \bar{w}_n^b	Phase c \bar{w}_n^c
M2	0.0100	0.0100	0.0100
M3	0.0100	0.0100	0
M4	0	0.0100	0.0100
M6	0.0100	0.0100	0.0100
M7	-	0.0100	0.0100

Table A.15: Per-unit apparent power capacity for DER placed nine node mesh network.

Appendix B

Newton-Raphson Algorithm for Solving Approximate Unbalanced Power Flow

This section presents the equations, residuals, and Jacobian terms for a Newton-Raphson method that solves unbalanced approximate power flow. The method presented here incorporates **A2**, **A3** where $\mathbf{H}_{mn} = \begin{bmatrix} 0 & 0 & 0 \end{bmatrix}^T$, **A4** to both the magnitude and angle equations, **A5**, and **A6**. Thus this method encompasses (10.53), (10.54), (10.55), (10.58), and (10.56). In this method, the pertinent variables are E_n^ϕ , θ_n^ϕ , P_{mn}^ϕ , and Q_{mn}^ϕ .

Line Real and Reactive Power

For a line $(m, n) \in \mathcal{E}$, if $\phi \notin \mathcal{P}_{mn}$ then by definition:

$$\begin{aligned} P_{mn}^\phi &= 0 \\ Q_{mn}^\phi &= 0 . \end{aligned} \tag{B.1}$$

The residuals are defined as:

$$\begin{aligned} \Delta P_{mn}^\phi &= 0 \\ \Delta Q_{mn}^\phi &= 0 . \end{aligned} \tag{B.2}$$

The partial derivative of the residuals are:

$$\begin{aligned} \frac{\partial \Delta P_{mn}^\phi}{\partial P_{mn}^\phi} &= 1 \\ \frac{\partial \Delta Q_{mn}^\phi}{\partial Q_{mn}^\phi} &= 1 . \end{aligned} \tag{B.3}$$

Magnitude Equation on Line (m, n)

For a line $(m, n) \in \mathcal{E}$, if $\phi \in \mathcal{P}_{mn}$ we consider (10.55) where \mathbf{M}_{mn} , and \mathbf{N}_{mn} , are defined by (10.58). For $\phi \in \mathcal{P}_{mn}$, the magnitude equation is:

$$E_m^\phi = E_n^\phi + 2 \sum_{\psi \in \mathcal{P}_{mn}} M_{mn}^{\phi\psi} P_{mn}^\psi - N_{mn}^{\phi\psi} Q_{mn}^\psi . \quad (\text{B.4})$$

The residual of the magnitude equation is:

$$\Delta E_{mn}^\phi = -E_m^\phi + E_n^\phi + 2 \sum_{\psi \in \mathcal{P}_{mn}} M_{mn}^{\phi\psi} P_{mn}^\psi - 2N_{mn}^{\phi\psi} Q_{mn}^\psi . \quad (\text{B.5})$$

The partial derivatives of the magnitude equation residual are:

$$\begin{aligned} \frac{\partial \Delta E_{mn}^\phi}{\partial E_m^\phi} &= -1 \\ \frac{\partial \Delta E_{mn}^\phi}{\partial E_n^\phi} &= 1 \\ \frac{\partial \Delta E_{mn}^\phi}{\partial P_{mn}^\psi} &= 2\mathbf{M}_{mn}^{\phi\psi} \quad \psi \in \mathcal{P}_{mn}, \\ \frac{\partial \Delta E_{mn}^\phi}{\partial Q_{mn}^\psi} &= -2\mathbf{N}_{mn}^{\phi\psi} \quad \psi \in \mathcal{P}_{mn} . \end{aligned} \quad (\text{B.6})$$

Angle equation on Line (m, n)

For a line $(m, n) \in \mathcal{E}$, if $\phi \in \mathcal{P}_{mn}$ we consider (10.56) where \mathbf{M}_{mn} , and \mathbf{N}_{mn} , are defined by (10.58), and e_m^ϕ and e_n^ϕ are fixed voltage magnitudes. For phase $phi \in \mathcal{P}_{mn}$, the angle equation is:

$$e_m^\phi e_n^\phi \theta_m^\phi = e_m^\phi e_n^\phi \theta_n^\phi - \sum_{\psi \in \mathcal{P}_{mn}} M_{mn}^{\phi\psi} P_{mn}^\psi + N_{mn}^{\phi\psi} Q_{mn}^\psi . \quad (\text{B.7})$$

The residuals of the magnitude equation is defined as:

$$\Delta \theta_{mn}^\phi = -e_m^\phi e_n^\phi \theta_m^\phi + e_m^\phi e_n^\phi \theta_n^\phi - \sum_{\psi \in \mathcal{P}_{mn}} M_{mn}^{\phi\psi} P_{mn}^\psi + N_{mn}^{\phi\psi} Q_{mn}^\psi . \quad (\text{B.8})$$

The partial derivatives of the magnitude equation residuals are:

$$\begin{aligned} \frac{\partial \Delta \theta_{mn}^\phi}{\partial \theta_m^\phi} &= -e_m^\phi e_n^\phi \\ \frac{\partial \Delta \theta_{mn}^\phi}{\partial \theta_n^\phi} &= e_m^\phi e_n^\phi \\ \frac{\partial \Delta \theta_{mn}^\phi}{\partial P_{mn}^\psi} &= -\mathbf{N}_{mn}^{\phi\psi} \quad \psi \in \mathcal{P}_{mn} \\ \frac{\partial \Delta \theta_{mn}^\phi}{\partial Q_{mn}^\psi} &= -\mathbf{M}_{mn}^{\phi\psi} \quad \psi \in \mathcal{P}_{mn} . \end{aligned} \quad (\text{B.9})$$

Node Voltage Magnitude and Angle

For a node $n \in \mathcal{N}$, if $\phi \notin \mathcal{P}_n$ then the voltage magnitude and angle are:

$$\begin{aligned} E_n^\phi &= 0 \\ \theta_n^\phi &= 0 . \end{aligned} \tag{B.10}$$

The residuals of the voltage magnitude and angle are:

$$\begin{aligned} \Delta E_n^\phi &= E_n^\phi \\ \Delta \theta_n^\phi &= \theta_n^\phi . \end{aligned} \tag{B.11}$$

The partial derivative(s) of the residual of the voltage magnitude and angle are:

$$\begin{aligned} \frac{\partial \Delta E_n^\phi}{\partial E_n^\phi} &= 1 \\ \frac{\partial \Delta \theta_n^\phi}{\partial \theta_n^\phi} &= 1 . \end{aligned} \tag{B.12}$$

Node Real Power Conservation

For a node $m \in \mathcal{N}$, if $\phi \in \mathcal{P}_n$ the conservation of real power, with p_m^ϕ taken as the real component of s_m^ϕ , is:

$$\sum_{l:(l,m) \in \mathcal{E}} P_{lm}^\phi = \left(A_{PQ,m}^\phi + A_{Z,m}^\phi E_m^\phi \right) \mathbf{Re} \{ d_m^\phi \} + u_m^\phi + \sum_{n:(m,n) \in \mathcal{E}} P_{mn}^\phi . \tag{B.13}$$

The residual of node real power conservation is:

$$\Delta p_m^\phi = - \sum_{l:(l,m) \in \mathcal{E}} P_{lm}^\phi + \left(A_{PQ,m}^\phi + A_{Z,m}^\phi E_m^\phi \right) \mathbf{Re} \{ d_m^\phi \} + u_m^\phi + \sum_{n:(m,n) \in \mathcal{E}} P_{mn}^\phi . \tag{B.14}$$

The partial derivatives of the residual of node real power conservation are:

$$\begin{aligned} \frac{\partial \Delta p_m^\phi}{\partial P_{lm}^\phi} &= -1 \\ \frac{\partial \Delta p_m^\phi}{\partial E_m^\phi} &= A_{Z,m}^\phi \mathbf{Re} \{ d_m^\phi \} \\ \frac{\partial \Delta p_m^\phi}{\partial P_{mn}^\phi} &= 1 . \end{aligned} \tag{B.15}$$

Node Reactive Power Conservation

For a node $m \in \mathcal{N}$, if $\phi \in \mathcal{P}_n$ the conservation of reactive power, with q_m^ϕ taken as the imaginary component of s_m^ϕ , is:

$$\sum_{l:(l,m) \in \mathcal{E}} \mathbf{Q}_{lm}^\phi = \left(A_{PQ,m}^\phi + A_{Z,m}^\phi E_m^\phi \right) \mathbf{Im} \{ d_m^\phi \} + v_m^\phi - c_m^\phi + \sum_{n:(m,n) \in \mathcal{E}} \mathbf{Q}_{mn}^\phi . \quad (\text{B.16})$$

The residual of node real power conservation is:

$$\Delta q_m^\phi = - \sum_{l:(l,m) \in \mathcal{E}} \mathbf{Q}_{lm}^\phi + \left(A_{PQ,m}^\phi + A_{Z,m}^\phi E_m^\phi \right) \mathbf{Im} \{ d_m^\phi \} + v_m^\phi - c_m^\phi + \sum_{n:(m,n) \in \mathcal{E}} \mathbf{P}_{mn}^\phi . \quad (\text{B.17})$$

The partial derivatives of the residual of node real power conservation are:

$$\begin{aligned} \frac{\partial \Delta q_m^\phi}{\partial Q_{lm}^\phi} &= -1 \\ \frac{\partial \Delta q_m^\phi}{\partial E_m^\phi} &= A_{Z,m}^\phi \mathbf{Im} \{ d_m^\phi \} \\ \frac{\partial \Delta q_m^\phi}{\partial Q_{mn}^\phi} &= 1 . \end{aligned} \quad (\text{B.18})$$

Slack Node Voltage Magnitude and Angle

Solving power flow typically requires selecting a slack node and assigning a fixed voltage reference. The slack node voltage magnitude variable will be represented by E_{sl}^ϕ , and the slack node voltage angle variable will be represented by θ_{sl}^ϕ . An overline notation will denote the fixed voltage reference. At the slack node, the voltage magnitude and angle are:

$$\begin{aligned} E_{sl}^\phi &= \overline{E}^\phi \\ \theta_{sl}^\phi &= \overline{\theta}^\phi . \end{aligned} \quad (\text{B.19})$$

The residuals of the slack bus voltage equations are:

$$\begin{aligned} \Delta E_{sl}^\phi &= E_{sl}^\phi - \overline{E}^\phi \\ \Delta \theta_{sl}^\phi &= \theta_{sl}^\phi - \overline{\theta}^\phi . \end{aligned} \quad (\text{B.20})$$

The partial derivatives of the residuals of the slack bus voltage equations are:

$$\begin{aligned} \frac{\partial \Delta E_{sl}^\phi}{\partial E_{sl}^\phi} &= 1 \\ \frac{\partial \Delta \theta_{sl}^\phi}{\partial \theta_{sl}^\phi} &= 1 . \end{aligned} \quad (\text{B.21})$$

Typically, the slack node is chosen as the node representing the transmission line, and given a voltage reference of $\mathbf{V}_{sl} = \left[1 \quad 1\angle 240^\circ \quad 1\angle 120^\circ \right]^T$.

Appendix C

Derivation of a Half-space Approximations for L2 Norm Constraints

Inverter dispatch is often bound by apparent power capacity limit; a bound on the magnitude of complex power dispatch, $u_n + jv_n$. Though this bound is convex, it is nonlinear, thus we seek to derive an easy to implement linear approximation of the apparent power capacity constraint:

$$\|u_n + jv_n\| \leq \bar{w}_n . \quad (\text{C.1})$$

We begin with the equation defining a circle and its interior centered at (x_0, y_0) with radius R , and express the variables x and y in polar form:

$$\begin{aligned} (x - x_0)^2 + (y - y_0)^2 &\leq R^2 \\ x &= x_0 + r \cos(\delta) \\ y &= y_0 + r \sin(\delta) , \end{aligned} \quad (\text{C.2})$$

with $0 \leq \delta \leq 2\pi$. We expand (C.2) to:

$$x^2 - 2x_0x + x_0^2 + y^2 - 2y_0y + y_0^2 \leq R^2 , \quad (\text{C.3})$$

and with (C.2), arrive at (C.4):

$$\begin{aligned} (x_0 + r \cos(\delta))x - 2x_0(x_0 + r \cos(\delta)) + x_0^2 + \dots \\ (y_0 + r \sin(\delta))y - 2y_0(y_0 + r \sin(\delta)) + y_0^2 \leq R^2 . \end{aligned} \quad (\text{C.4})$$

Here we separate $(x_0 + r \cos(\delta))x$, and again use (C.2) in x_0x and y_0y , giving (C.5):

$$\begin{aligned} x_0(x_0 + r \cos(\delta)) + r \cos(\delta)x - 2x_0(x_0 + r \cos(\delta)) + x_0^2 + \dots \\ y_0(y_0 + r \sin(\delta)) + r \sin(\delta)y - 2y_0(y_0 + r \sin(\delta)) + y_0^2 \leq R^2 . \end{aligned} \quad (\text{C.5})$$

To simplify (C.5), we cancel the x_0^2 and y_0^2 terms, and gather the $x_0 r \cos(\delta)$ and $y_0 r \sin(\delta)$

$$r \cos(\delta)x - x_0 r \cos(\delta) + r \sin(\delta)y - y_0 r \sin(\delta) \leq R^2 . \quad (\text{C.6})$$

Points on the boundary of the set will have $r = R$, which we plug into (C.6). As $R > 0$, we can divide both sides by R , and thus finish with (C.7), a linear relationship for the generic variables (x, y) :

$$\cos(\delta)x + \sin(\delta)y \leq r + x_0 \cos(\delta) + y_0 \sin(\delta) . \quad (\text{C.7})$$

Equation (C.7) gives a linear constraint on the variables x and y for the parameter δ , and defines the half-space tangent to the circle at point $(x, y) = (x_0 + R \cos(\delta), y_0 + R \sin(\delta))$. Half-spaces are convex, as are the intersection of any number of half-spaces. Thus a set N_c half-spaces of the form (C.8) will form a convex linear approximation of a circle:

$$X = \{(x, y) \mid \cos(\delta_k)x + \sin(\delta_k)y \leq r + x_0 \cos(\delta_k) + y_0 \sin(\delta_k), \\ \delta_k = \frac{k2\pi}{N_c}, k = 0, 1 \dots N_c\} . \quad (\text{C.8})$$

This linear approximation can be seen in Figure C.1 for $N_c = 12$ such that $\delta_k = 30^\circ$. The accuracy of the approximation is shown in Figure C.2, with the number of half spaces ranging from 4 ($\delta_k = 90^\circ$) to 120 ($\delta_k = 3^\circ$). It can clearly be seen that around 60 half-spaces, the half-space approximation contains 0.1 % more area than the circle defined by the L2 norm constraint.

Substituting the original variables for real and reactive complex power dispatch and apparent power capacity:

$$W_n^\phi = \{(u_n^\phi, v_n^\phi) \mid \cos(\delta_k)u_n^\phi + \sin(\delta_k)v_n^\phi \leq \bar{w}_n^\phi + u_{n,0}^\phi \cos(\delta_k) + v_{n,0}^\phi \sin(\delta_k), \\ \delta_k = \frac{k2\pi}{N_c}, k = 0, 1 \dots N_c\} . \quad (\text{C.9})$$

where $(u_{n,0}^\phi, v_{n,0}^\phi)$ is the center of the apparent power constraint.

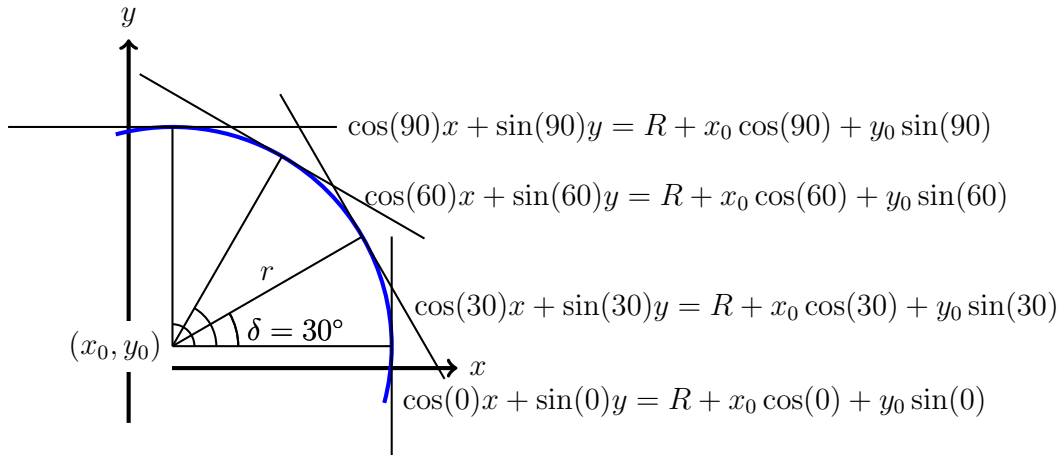


Figure C.1: Tangential half-space approximation of circle.

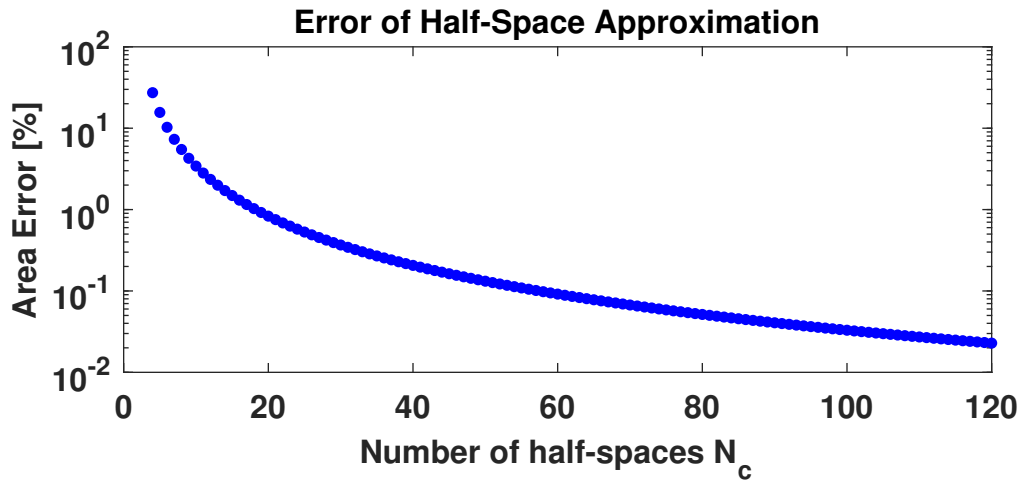


Figure C.2: Error of half-space approximation of apparent power constraint.